An Optical Method of Strain Measurement in the Split Hopkinson Pressure Bar

Steven David Swantek

Thesis submitted to the Faculty of the Virginia Polytechnic Institute and State University
in partial fulfillment of the requirements for the degree of

Master of Science
in
Mechanical Engineering

Dr. Alfred L. Wicks, Chairman
Dr. William L. Saunders
Mr. Leonard T. Wilson, NSWCDD

August 3, 2000
Blacksburg, Virginia

Keywords: Hopkinson Bar, Kolsky Bar, High Strain Rate, Laser, Impact Testing, Material Testing, Dispersion, NSWCDD

An Optical Method of Strain Measurement in the Split Hopkinson Pressure Bar

Steven David Swantek

(ABSTRACT)

The split Hopkinson pressure bar (SHPB) continues to be one of the most common methods of testing materials at medium rates of strain. Elevated rates of strain, such as those found in impact and explosive applications, have been shown to induce phenomena such as strain hardening and phase transitions that can significantly affect the strength of most materials [14]. Due to its relative simplicity and robustness, the SHPB remains one of the preferred platforms for evaluating mechanical properties of materials at rates of strain up to approximately 10^4 in/in-s (s^{-1}). At the Naval Surface Warfare Center Dahlgren Division (NSWCDD), research has been conducted in which a semiconductor laser diode has been used to measure the radial strain of a plastically deforming cylindrical test specimen in the SHPB.

The SHPB consists of two long, slender cylindrical bars, denoted input and output bars, that "sandwich" a cylindrical test specimen. Utilizing a high-pressure gas gun, a third cylindrical steel bar, known as the striker bar, is fired at the input bar, causing a compressive stress wave to travel through the input bar to the input bar - test specimen interface. At this interface, a portion of the stress wave propagates through the test specimen while the remainder of the pulse reflects back through the input bar as a tensile stress wave. The non-reflected portion of the stress pulse transmits through the test specimen and into the output bar causing the specimen to deform both elastically and plastically. Strain gages mounted to the input and output pressure bars measure both the incident, transmitted and reflected pulses. Specimen stress can be calculated using the

transmitted strain signal while specimen strain and strain rate can be computed using the reflected strain pulse.

In order to measure the specimen strain directly, a 670-nm wavelength semiconductor laser diode was affixed to the SHPB such that a vertical line of light approximately 250 micrometer (μm) wide was generated across the diameter of the test specimen. A collector lens located aft of the specimen was positioned to collate the light not occluded by the diameter of the specimen and refocus the light to be collected by a 25 MHz photodetector. Thus, changes in specimen diameter due to the impact event would result in more light being occluded by the specimen and less spectral energy being collected by the photodetector. The light collected by the photodetector is then converted to a voltage output before being recorded by a digital storage oscilloscope. With a known voltage-to-diameter calibration relationship, medium strain rate compressive tests were conducted to compare the optically measured strain results with the data gathered with the existing strain gages.

It was found that the optical measurement system provided increased bandwidth and greater resolution than the conventional strain gage instrumentation while generating strain and strain rate results within 6.7% of corresponding strain gage data. This increased bandwidth and resolution allows the identification of both the elastic and plastic behavior of the specimen. In addition, the loading and unloading of the specimen can be clearly seen in the optical strain signal. These phenomena are evident in the peak diameter and strain achieved by the specimen, data not previously available with strain gage instrumentation. The plastic modulus, the theoretical relationship between the stress and strain in the plastic regime, also exhibits a significant increase in magnitude due to this ability to measure peak rather than average strain. Finally, by ridding the experiment of the input bar strain gage, input bar dispersion and the electrical and mechanical errors associated with the input bar strain gage were nullified. These conclusions will be validated through the presentation of several sets of experimental data correlated to data gathered previously.

Acknowledgements

I would like to begin by thanking Dr. Wicks for believing in me and for trusting me to continue the research for the Naval Surface Warfare Center. Before being offered this research position, I was having serious doubts about my future as a graduate student. Without Dr. Wicks' help, I do not believe that I would have ever completed my Master's Degree here at Virginia Tech.

I would also like to thank Leonard Wilson at the Naval Surface Warfare Center for answering my never-ending lists of questions. The patience he afforded me during this research has been truly inspiring. If I can leave here with but a fraction of the patience and tolerance Leonard has displayed, I will feel fortunate.

This thesis and research would not have been possible without the help of the now-retired Benny Simpson of NSWCDD as well as Gary Bass, also of NSWCDD. Both of these men were instrumental in helping me perform the actual testing used to gather my data. Also, a great deal of thanks goes to Dr. Will Saunders for serving on my committee and for being such a lethal weapon on our intramural basketball squad.

In addition, I would like to thanks each of the members of my committee for allowing me to pursue other interests. I think its safe to say that engineers have a reputation for being, to put it kindly, one-dimensional. What I am most proud of upon completion of this rigorous research is that I am the same person that arrived at Virginia Tech two years ago: a pilot, a runner, a poor basketball player and a mediocre golfer. Through it all, my committee members have allowed me and, in some cases, encouraged me to be more than just an engineering graduate student. So, to Dr. Wicks, Leonard and Dr. Saunders, thank you!

Table of Contents

List of Figures

List of Tables

CHAPTER 1. INTRODUCTION

1.1 Introduction

The field of material science continues to be one of the most dynamic disciplines in the engineering community. The demand for stronger, lighter and more corrosion-resistant materials continues to fuel a field that has seen many remarkable discoveries over the past few decades. From "better" alloys of steel and aluminum to the increased usage of titanium to the development of ceramic and composite materials, the advancements made in material science have been critical to industry's ability to design bigger, stronger, lighter and more durable components and structures. With the development of these new materials, there exists the need to be able to characterize and tabulate the chemical, electrical and mechanical properties of these new materials. Likewise, there always exists the need to determine more accurately those properties previously investigated and tabulated. At medium rates of strain (up to 10^4 s^{-1}), the split Hopkinson pressure bar (SHPB) has been one of the most widely used methods of evaluating the mechanical properties of materials. This chapter will discuss the basics of material testing (both quasi-static and dynamic) as well as the fundamentals of the SHPB. In addition, a brief but important note about laser safety will be presented in this chapter. Instrumentation issues in the split Hopkinson pressure bar will also be discussed and the chapter will conclude with an overview of this research and thesis.

1.2 Dynamic Testing of Materials

Of particular interest to mechanical and structural engineers are the mechanical properties of engineering materials. In the elastic regime, these mechanical properties include the modulus of elasticity (Young's Modulus), yield strength and Poisson's Ratio, to name but a few. Typically, these mechanical properties are gathered by subjecting a test specimen to unidirectional loads at very slow rates of strain and measuring the resulting elongation. The recorded data is then used to generate a stress-strain diagram. According to Shigley and Mitchell [1], "The average strain rate used in obtaining the typical stress-strain

diagram is approximately 0.001 in/in-s." Figure 1.1 below shows a typical stress-strain diagram generated using a low-strain rate tensile test.

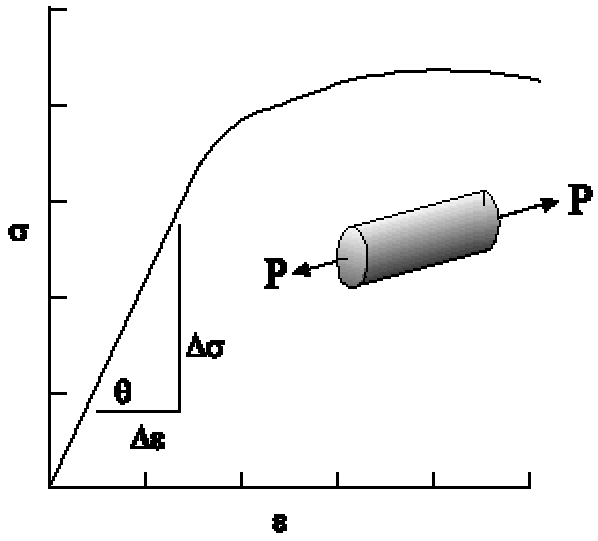

Figure 1.1 Typical Quasi-static Stress vs. Strain Relationship [25]

In Figure 1.1, P is the applied uniaxial tensile load, ε is the specimen strain (plotted on the independent axis) while σ is the specimen stress (plotted on the dependent axis). As illustrated in the figure above, the stress and strain exhibit a linear relationship at low levels of strain (less than 0.02%), indicating the presence of elastic behavior. At higher strain levels, however, the slope of the curve begins to approach zero, indicating the effects of work hardening. This behavior is indicative of and a result of plastic deformation. Continuing this analysis σ is typically defined as the force per unit area and can be calculated via Equation 1.1:

$$\sigma = \frac{P}{A} \qquad \textbf{1.1}$$

In the above equation, A is the cross sectional area of the specimen. Stress and strain can then be related by Young's Modulus, also known as the Modulus of Elasticity, shown below in Equation 1.2:

$$E = \frac{\Delta\sigma}{\Delta\varepsilon} \qquad \textbf{1.2}$$

Equation 1.2, also known as Hooke's Law, is valid only in the linear confines of Figure 1.1. At the proportional limit of the particular material, the stress and strain no longer exhibit the linear relationship described by Equation 1.2. However, this linear relationship described by Equations 1.1 and 1.2 provides a simple yet effective means of determining and predicting material properties at low levels of strain.

Although this method of testing generates acceptable results for most static and quasi-static designs, highly dynamic applications such as those involving shock and impact loads necessitate the need for further testing at higher rates of strain. As seen above in Figure 1.1, at elevated levels of strain, the linear relationship between stress and strain breaks down as strain hardening and similar effects begin to appear. According to R.A. Graham [14],

> "Solid substances are forced into unusual and distinctive conditions when subjected to powerful releases of energy such that their initial properties result in the propagation of high pressure mechanical waves within the solid body. Very high stress, microsecond duration conditions irreversibly force materials into states not fully encountered in any other excitation."

Since phenomena such as strain hardening, flow stresses and phase transitions have been proven to significantly affect the mechanical properties of materials subjected to higher loads and loading rates, data tabulated using the above experimental methods should not be used in highly dynamic applications as this data tends to underestimate the strength of the most materials. Thus, a method for evaluating these properties at elevated rates of strain is needed. This is the primary motivation for the SHPB.

The split Hopkinson pressure bar, a derivative of the Hopkinson bar, has quickly become one of the one of the preferred testing platforms for medium strain rate material testing. The Warheads Branch at the Naval Surface Warfare Center in Dahlgren, Virginia

(NSWCDD) utilizes this derivative of the Hopkinson Bar to perform material testing at strain rates up to 10^4 s^{-1}. As will be demonstrated later in this thesis, an extensive amount of experimental, computational and analytical research has allowed scientists to gain valuable insight into the physics and dynamics of the SHPB. However, very little research into alternative methods of instrumentation has been done. This is the primary motivation for designing and implementing an optical strain measurement system for the SHPB.

1.3 The Split Hopkinson Pressure Bar

At present, the most widely used version of the Hopkinson Bar is the split Hopkinson bar, more commonly referred to as the split Kolsky bar or split Hopkinson pressure bar (SHPB). As detailed earlier, the SHPB is especially useful in determining the mechanical properties of materials at medium rates of strain. Typical SHPB facilities are capable of generating strain rates up to approximately 10^4 s^{-1}. The SHPB in use at NSWCDD can be seen below in Figure 1.2.

Figure 1.2 NSWCDD Split Hopkinson Pressure Bar Facility

Scientists have shown that high stress, microsecond duration events can have significant influence on the strength of materials subjected to such events. According to C.S. Coffey [15], "Several metals have been shown to withstand much greater stresses when dynamically loaded than under quasi-static conditions." Thus, it has become universally accepted that many materials, especially metals, exhibit significantly different mechanical properties when subjected to higher loading rates. Events likely to result in high strain behavior include shock, explosive and impact events, to name but a few. Thus, there definitely exists the need for testing at these elevated rates of strain.

Figure 1.3 below shows a simplified schematic of a typical compressive SHPB.

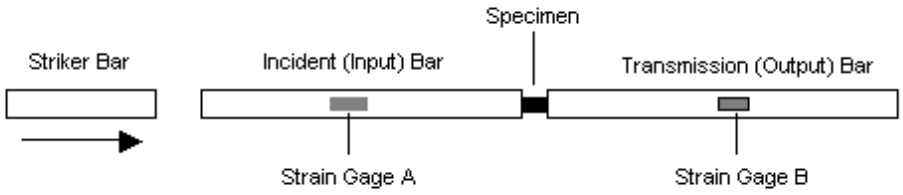

Figure 1.3 Simplified Schematic of the Split Hopkinson Pressure Bar

In the SHPB, a cylindrical test specimen is coated with a thin layer of grease and placed between two cylindrical bars. Typically, these bars range from 0.50" to 0.75" in diameter and 4' to 5' in length and are made from high-strength steel. Typical specimen dimensions are 0.25" in diameter and 0.25" in length. Proper alignment of the pressure bars with the specimen ensures a uniaxial state of stress while the thin layer of grease applied to the specimen promotes homogeneous deformation in the specimen. With the test specimen "sandwiched" between the two cylindrical bars, a projectile bar, known as the striker bar, is fired at the end of one of the first cylindrical test bar, known as the input or incident bar. The impact of the projectile bar striking the input bar causes a compressive stress pulse to propagate through the input bar until it reaches the input bar-

test specimen interface. At this interface, a portion of the stress pulse is transmitted through the specimen while the remainder of the wave reflects back through the input bar. As the compressive wave travels through the test specimen and into the second test bar, known as the output or transmission bar, the reflected wave travels back through the input bar as a tensile wave. The importance of this phenomenon will be further investigated later in this thesis. Thus, three distinct strain signals are of interest to the SHPB investigator: the incident reflected and transmitted pulses. Conventionally, strain gages mounted to the input and output pressure bars are used to record these strain signals.

The figure presented above, although a very simplified illustration of the SHPB, gives the reader a general idea of the experimental procedure. Note the arrow above the striker bar indicating the axis of motion in the experiment. Not shown in Figure 1.3 are the bearing blocks that support the pressure bars while limiting all motion to the longitudinal axis of the striker, input and output bars. Also, the specimen size has been greatly exaggerated in relation to the test bars to give the reader a clearer picture of the test procedure. Other important considerations in the design of the experiment include the dimensions of the striker bar, pressure bars and test specimen as well as the yield strengths of the pressure bars. These considerations will be detailed later in this thesis.

As for the actual impact event, the physics associated with the collision of the striker bar with the input bar and the subsequent generated stress wave are governed mainly by the laws of dynamics and vibrations. As such, bar boundary conditions and impact response characteristics become important considerations when performing the experiment. In addition to the bearing blocks described above, the bar ends are precisely machined such that the ends of the bars are flat. This machining coupled with the bearing constraints allows the event to be modeled as a uniaxial stress, homogeneous deformation problem. Also, the use of high strength maraging steel in the production of the pressure bars dictates that, for the strain rate limitation imposed at NSWCDD (10^4 s^{-1}), the bars are limited to stress levels well below their elastic limits, except in the case of very dense materials such as tungsten and certain Aermet alloys. With proper precautionary

measures, the SHPB experiment can be configured such that the pressure bars undergo zero plastic deformation and negligible elastic deformation. These assumptions will be revisited later in this thesis. Assuming dynamic equilibrium within the test specimen and pressure bars, the investigator is able to calculate specimen stress, strain and strain rate information directly from the strain histories recorded by the strain gages. By careful processing of the incident, reflected and transmitted strain pulses, the corresponding stress-strain relationship for the material can be calculated. Kolsky [2] first published this relationship in 1949:

$$\sigma_s(t) = E\frac{A_0}{A_S}\varepsilon_T(t) \tag{1.1}$$

In Equation 1.1, $\sigma_s(t)$ is the temporal history of the stress experienced by the specimen, E is the output bar's elastic modulus, A_0 is the cross sectional area of the output bar, A_S is cross sectional area of the specimen and $\varepsilon_T(t)$ is the transmitted strain history recorded at the output bar strain gage. The actual strain rate generated by the impact can be calculated via Equation 1.2:

$$\frac{d\varepsilon_s(t)}{dt} = -\frac{2C_0}{L}\varepsilon_R(t) \tag{1.2}$$

In Equation 1.2, $\varepsilon_s(t)$ is the temporal history of the specimen strain, C_0 is the infinite wavelength wave velocity in the input bar, L is the initial length of the specimen and $\varepsilon_R(t)$ is the strain history generated by the reflected pulse in the input bar. The C_0 term used above is, by definition, the "infinite wavelength wave velocity" in the input bar and can be estimated as

$$C_0 = \sqrt{\frac{E}{\rho}} \tag{1.3}$$

where, again, E is the elastic modulus of the input bar and ρ is the density of the input bar. Finally, the time history of the specimen strain can be computed by integrating Equation 1.2. This results in Equation 1.4:

$$\varepsilon_s(t) = -\frac{2C_0}{L}\int_0^t \varepsilon_R(t)dt \qquad \textbf{(1.4)}$$

With the mechanical properties calculated above, corresponding stress-strain diagrams can be generated. With this data, material response and performance at higher strains and strain rates can be determined. Obviously, all of these computations are based on the assumption that good-quality strain signals are being recorded at the input and output pressure bars. Since the accuracy and precision of these results depends directly on the quality of the data, any improvements to the data acquisition techniques used in the test would be of great interest to the engineering community.

1.4 Limitations of the Split Hopkinson Pressure Bar

Many scientists have experimented with the SHPB by using various configurations of input and output bars, varying the size of the test specimens, lubricating the test specimen - pressure bar interface and utilizing numerous types of amplifiers and filters in an effort to improve the quality of the test results [3, 23]. While all of these experiments have had their share of successes and failures, most investigators would agree that the area most in need of improvement is in the instrumentation of the SHPB. For the last 30 years, the most widely used method of instrumentation in the SHPB has been a configuration of strain gages connected to some combination of amplification and storage system. For the most part, however, improvements in strain gage technology have been nearly nonexistent when compared to the advancements made in the computer hardware and data acquisition fields. Consequently, researchers have continually updated their data acquisition hardware but have neglected to investigate more efficient methods of strain measurement.

Since their development, strain gages have been known to exhibit thermal, electrical and spatial sensitivity errors. Thermal effects such as fluctuating ambient temperatures and sensitivity to localized heat sources (even heat generated by the gage itself) have been shown to result in nonzero output for zero input conditions [25]. Bias currents and current leakage have also been shown to contribute to the output of typical electrical resistance strain gages. In addition, out-of-plane motion, typically that motion which is orthogonal to the strain-sensing grid, can cause similar errors [26]. In many cases, and especially in the case of small strains, these errors can be significant. Likewise, strain gages have been shown to output an average strain as opposed to the peak strain in cyclic strain applications due to construction limitations of the gage. This introduces the concept of windowing error, the tendency of the strain gage to attenuate the peak strains associated with cyclic strain events. Kaiser [18] published a lengthy discussion of the errors inherent to electrical resistance strain gages in 1998 and this work was presented at the American Physical Society's Shock and Compression of Condensed Matter Conference in 1999. This windowing effect as well as the other sources of error described above will be presented in much greater detail later in this thesis.

An additional limitation inherent to the use of strain gages in the SHPB stems from the small size of the test specimens and the fact that the test specimens subjected to high level of stress and strain. Because of the need to remain well below the elastic limit of the pressure bars, the test specimen must be made very small. Because of this and because it is expected that the test specimen will undergo highly dynamic plastic deformation, the strain gage cannot be mounted directly to the test specimen. Consequently, the gages must be mounted to the input and output pressure bars. With this remote-mounting scheme, scientists have found it more convenient to mount the gages at the longitudinal center of the bars, a distance of up to 3 feet from the actual test piece. The logic behind this mounting location is that it becomes much easier to separate the incident and reflected pulses within the incident bar during the post-processing stages of the experiment. Should the strain gages be mounted at or near the ends of the input and output bars (nearest the specimen), the possibility exists that a portion of the incident and reflected signals could not be differentiated from one another. So, in an effort to

simplify the processing of the strain signals, the strain gages are typically at the longitudinal centers of the input and output bars. Besides the uncertainty of the reaction at the specimen-pressure bar interface, this subjects the experiment to a phenomenon known as dispersion.

Dispersion can best be described as the velocity dependence of a pressure wave on frequency as it travels through a medium [5]. In the case of the SHPB, the strain signals are corrupted as the pressure waves propagate through the input and output pressure bars. Figure 1.4 shows a typical SHPB strain history with the effects of dispersion clearly labeled.

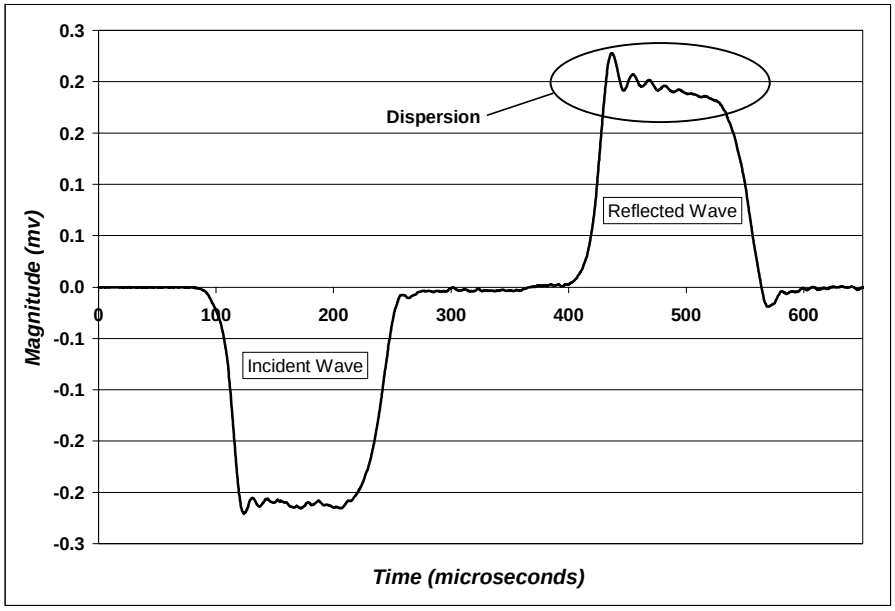

Figure 1.4 SHPB Strain History Corrupted by Dispersion

The impact of the striker bar with the input bar, similar in nature to an impulse, generates pressure waves of many different frequencies within the pressure bar, each of which arrives at the strain gages at different times. As these waves propagate through the pressure bars, the strain gages sense this as localized strain events. Thus, dispersion causes a significant ripple in the temporal strain signal generated during the experiment. This can be clearly seen in the figure presented above. In addition, as the wave disperses

within the pressure bar, the stress wave sensed by the strain gage is not the stress wave seen by the specimen. Although much research and modeling has been done regarding this phenomenon of dispersion, it continues to be one of the greatest limiting factors and sources of uncertainty in the SHPB.

One final limitation on the current method of instrumentation in the SHPB is the difficulty in obtaining an acceptable signal-to-noise ratio (S/N) for more compliant materials such as plastics, polymers and viscoelastic materials. For such materials, very little of the original stress pulse is reflected back into the input bar, resulting in a very poor signal-to-noise ratio at the input bar [18]. In order to compensate for this shortcoming, many investigators have experimented with viscoelastic, aluminum and magnesium pressures bars and, in some instances, hollow pressure bars [33], [34]. In addition, different methods of data reduction have been suggested to resolve such S/N problems. Few researchers, however, have experimented with alternative strain measurement techniques. Although such materials will not be investigated in this research, conclusions and recommendations regarding the use of the optical strain measurement system in similar applications will be presented and discussed.

1.5 A Note on Laser Safety

Because this research involves the use of a laser (solid state, semiconductor laser diode), information regarding the use of lasers and related safety issues should be addressed before proceeding further with this thesis. In industry, laser safety standard are divided into four hazard classifications: Class II, Class IIIa, Class IIIb and Class IV. Each classification is based upon the output power of the laser itself (no additional optics included) and, the higher the classification number, the greater the potential danger. For reasons detailed later in this thesis, a 0.9 mW semiconductor laser diode was chosen for this application. Consequently, this low power laser falls into Hazard Class II, which reads as follows:

> **Class II** - "Caution" low power visible laser or laser system less than 1 mW which, because of the normal human aversion response

> (eye blinking, eye movement, etc.) do not normally present a hazard, but may present a potential hazard if viewed directly for extended periods of time.

Thus, for reasons of safety, it is recommended that the user refrain from staring directly into the beam for extended periods of time. However, incidental contact with the laser beam will present no undue hazard. For additional measures of safety, it is recommended that the laser be de-energized or that the beam attenuator be installed when the laser is not in use. These precautions will be reviewed again in Chapters 4 and 6 of this thesis.

1.6 Thesis Overview

In order to get more accurate results from the SHPB, a better instrumentation method is needed such that the errors associated with electrical resistance strain gages and pressure bar dispersion can be reduced. With the recent rise in popularity of lasers, it was theorized that an optical strain measuring system similar to but much simpler in nature than a laser interferomic system could be used in place of one and/or both of the existing strain gages. Monitoring specimen strain via radial measurements directly at the specimen could effectively cancel out the effects of the pressure bar dispersion at the input and/or output pressure bars on the computed strain and strain rate. In addition, better resolution and frequency response could potentially be achieved with the optical strain measurement system while also ridding the results of much of the error associated with conventional electrical resistance strain gages.

Accordingly, it was decided that a simplified laser occlusive measurement system would be designed and installed on the split Hopkinson pressure bar at the Naval Surface Warfare Center in Dahlgren, Virginia (NSWCDD). In order to make the system as simple yet robust as possible, a direct interference system was designed. In essence, a semiconductor laser diode will be positioned such that the diameter of the specimen will occlude a portion of the laser light. As the specimen deforms under the compressive stress event, its diameter increases, thus occluding more of the laser light. A photodetector positioned beyond a collimating/filtering lens assembly will capture that

portion of the light not occluded by the specimen and will convert this optical energy into a corresponding voltage output. Conceptually, this system is elegant in that it utilizes a semiconductor laser diode and high-speed silicon photo-detector to directly measure the specimen radial strain yet simple in that it lacks the more complex components such as beam splitters and reflecting optics used on "true" interferomic systems.

The remainder of this thesis is devoted to better understanding the split Hopkinson pressure bar, related instrumentation issues as well as the science of laser technology and, more specifically, how it relates to the application at NSWCDD. Included in Chapter 4 will be the methodology used inn designing the optical system as well as the thought that went into selecting the components necessary for implementation of the design. This thesis will conclude with a comparison of data gathered using the existing strain gage instrumentation with data gathered using the optical measurement system. These results will be analyzed in detail such that conclusions can be drawn as to the effectiveness of this optical method of strain measurement.

Chapter 2. Background and Literature Review

2.1 Introduction

In conducting the research involved in this thesis, several different disciplines of engineering were researched including material science, optical engineering, electrical engineering as well as mechanical engineering. It is fairly obvious how material science, optical and mechanical engineering relate to the dynamic testing of materials but not so obvious where electrical engineering research might help with this work. This chapter will give the reader a curt overview of the different references used to perform this research as well as an evaluation as to the usefulness of each particular reference. Specific areas of research include Hopkinson bar testing, fundamentals of laser interferometry, dynamic testing of materials and circuit design and construction. Besides summarizing the various references used by the author, this chapter will also present a concise, chronological development of both the Hopkinson bar and the laser as experimental engineering tools.

2.2 The Hopkinson Bar

This section will provide a brief chronological development of the Hopkinson bar as an engineering tool. The Hopkinson bar has long been one of the most widely used methods of testing materials at medium rates of strain. Also included in this section is a concise review of some of the major accomplishments made in Hopkinson bar testing, including the development of the Kolsky Bar, strain gage technology and numerical modeling techniques.

2.2.1 The Hopkinson Bar – A Chronological Development

In 1913, Bertram Hopkinson developed a new technique for determining the peak pressure achieved during an impact or shock event. Hopkinson's idea was to subject a small, steel test specimen to a compressive stress wave via a long, cylindrical steel bar.

The test piece was coated with a thin layer of grease to hold the specimen to the end of the steel bar and to allow for uniaxial, homogeneous deformation. His theory was that, after traversing through the test specimen, the compressive pulse would cause the specimen to impact a ballistic pendulum calibrated for momentum measurements. Hopkinson determined that measuring the elapsed time of the momentum event was equivalent to measuring the longitudinal wave speed developed in the test piece. In addition, measurement of the displacement of the ballistic pendulum provided Hopkinson with an indirect measure of the pressure developed by the impact event. With this data, Hopkinson was able identify peak pressures and estimate the longitudinal wave speeds in a variety of test specimens. However, lacking reliable methods of data storage and reduction, he was unsuccessful in generating reliable pressure versus time relationships for the impact experiments. He had, however, unknowingly laid out a method of material testing that would be revisited by future researchers and scientists investigating the dynamic response of materials subjected to elevated rates of strain.

Significant advancements were not made in Hopkinson bar testing until the 1940's when Davies [7] developed a novel technique of strain measurement utilizing electrical condensers. Davies' idea was that the displacement (strain) in the pressure bar was proportional to the stress developed in the bar, provided the pressure in the bar was well under the elastic limit of the pressure bar material. With this assumption in mind, Davies designed a condenser mechanism to generate an electrical output that was proportional to the displacement of the pressure bar in Hopkinson's original apparatus. One of the primary motivating factors behind Davies' work was the uncertainty associated with the grease applied to the test specimen. He was certain that the grease added to the dynamics of the experiment but he was unsure how to account for it. Thus, Davies was able to improve the data acquisition process of Hopkinson's experiment by replacing the ballistic pendulum with his condenser strain measurement system while lessening the error and uncertainty associated with the greased test specimen.

Other work in the 1940's related to the Hopkinson Bar was done by physicists and material scientists interested in the wave propagation phenomenon in solid structures.

Hopkinson had studied this phenomenon during his years of research but it was not until the 1940's that this idea gained significant interest. Researchers such as Pochhammer and Love [27] derived equations describing the wave speed dependency on frequency in solids. Scientists knew that short duration impact events yielded stress waves with large amounts of spectral content. Thus, acoustic waves of many different frequencies resulted from the single impact event. A great amount of research was done in an attempt to characterize this spectral content in terms of frequency, wave speed and impact pulse shape. With all of the research that was done, Dennison Bancroft [5] published a series of solved equations for the longitudinal wave velocities in cylindrical bars. His equations were reduced to forms including Poisson's Ratio, infinite wave wavelength, pressure bar density and pressure bar diameter – wavelength ratio. Although Bancroft did little research directly with Hopkinson's original experiment, his work provided future researchers a method for determining wave velocities in the pressure bars used in Hopkinson bar testing.

The most profound addition to Hopkinson's research came in the late 1940's and early 1950's when Kolsky modified the original design with the addition of a second pressure bar [2]. Kolsky's motivation was that the addition of the second pressure bar would allow for strain data to be recorded at the input and output interfaces of the test specimen. In addition to specimen strain, this new version of Hopkinson's experiment allowed researchers to calculate specimen stress and strain rate. Also, a consequence of "sandwiching" the test specimen between the two pressure bars was that homogeneous deformation would be much more easily achieved. Taking a page from Davies' notes, Kolsky used an electrical condenser system to measure the strains in both pressure bars, known as the input and output pressure bars. Using the strain data from the two pressure bars, Kolsky was able to derive expressions for calculating specimen stress, strain and strain rate. Due to its improved robustness, versatility and accuracy, Kolsky's version of the Hopkinson bar, which became known as the Kolsky bar or split Hopkinson pressure bar (SHPB), quickly became one of the preferred methods for testing materials at strain rates from 10^2 s^{-1} to 10^4 s^{-1}. Additional research into the dynamics associated with the

SHPB was done by scientists such as Lindholm and Yeakly [3], Gorham and Wu [28], and Bertholf and Karnes [4].

Significant improvements to methods of strain measurement came about in the 1960's with the introduction of strain gage technology. Using the change in resistance of a conductor due to changes in its length and cross sectional area, scientists could now measure the voltage output of a strain gage device and relate it to the displacement of the surface to which the gage was applied. Krafft, et al [29], first implemented strain gage technology in the Hopkinson bar in 1954 when they studied the effects of static and dynamic loading and temperature on the yield stress of iron and mild steel in compression. In 1961, Hauser, et al [30], used strain gages on the SHPB in his studies of static and dynamic compressive loading of iron and mild steel at elevated temperatures. Lindholm and Yeakly [3] performed similar research just 3 years later in his studies of the SHPB. His experiments involved selection and mounting of the strain gages as well as interpretation of the data generated by the experiment. Even in its earliest stages of development, it was found that the strain gage significantly increased the accuracy, resolution and repeatability of the data.

Since the 1970's, the most significant improvements to the Hopkinson bar experiment and its derivatives have come in the form of high-speed computer data acquisition systems. Digital storage oscilloscopes and high-bandwidth signal analyzers have allowed the scientist to obtain much more highly resolved data with much greater precision. Current researchers routinely use digital storage oscilloscopes with bandwidths as high as 500 MHz. Additional research has been done into pressure bar characteristics, specimen geometry effects and mathematical modeling. Kaiser [18] presented his experimental results in 1998, which included a new dispersion correction technique and a novel numerical method of aligning strain pulses. Other recent advancements have come in strain gage technology, as new grid patterns and sensing element materials have been introduced which have greatly reduced the errors associated with the strain gage. Such errors include lateral strain sensitivity, thermal sensitivity and hysteresis effects [26].

Ramesh and Narasimhan [19] were the first investigators to publish SHPB data using an optical strain measurement system (1996). Their optical system, known as the LORD (Laser Occlusive Radius Detector) system, utilized a 670-nanometer (nm) laser diode capable of generating 3 miliwatts (mW) of output power to measure the change in diameter of the cylindrical specimen typically used in the SHPB. Though their LORD system produced very promising results, little work has been done involving the use of optical measurement methods in the Hopkinson bar since their efforts.

2.2.2 The Split Hopkinson Pressure Bar – Additional Resources

With the recent advancements in instrumentation and data processing techniques, the SHPB has seen a renewed interest in its use as the primary method of material testing at medium rates of strain. This includes the testing of materials previously thought too compliant for the SHPB apparatus, materials such as foams, rubbers, and other viscoelastic materials. Researchers such as Al-Mousawi, et al [31], Bateman, et al [32] and Chen, et al [33] have been able just recently to test such materials in the SHPB and still achieve acceptable signal-to-noise ratios. A contributing factor to these recent studies is the development of better, faster and more noise-resistant integrated circuits and signal analyzers. Recent advancements in computer modeling capabilities have also played a significant role in this research.

Also, this renewed interest in the SHPB has resulted in the publication of a number of technical articles on the subject of dynamic testing of materials. Gray [34] provides one of the better reviews of the SHPB technique as both a compressive and tensile testing tool. Additionally, Gong, et al [35] presents an in-depth study of the dynamics of the SHPB while focusing primarily on the phenomenon of dispersion. Similar research was also done by Graff [6] in 1991.

2.3 Light Amplification Using Stimulated Emission of Radiation

This section will present a chronological summary of the development of the laser. Although it has not been until just recently that the laser has gained significant popularity

as practical engineering tool, the history of laser science dates back to the early 20th century. This section will detail the history of the laser from Einstein's first musings of stimulated emissions of light to today's military and industrial applications of laser technology.

2.3.1 The Laser – A Chronological Development

Prior to the 20th century, scientists viewed light as a type of electromagnetic radiation with predominantly wavelike properties. However, researchers began to lay out the idea of quantum mechanics, the idea that light existed at specifics levels or quanta of energy. Thus, the idea of photons was born. However, it was not until Albert Einstein's work in 1916 that the idea of stimulated emission of photons became an area of future research [10]. That year, Einstein postulated the idea that a photon with energy corresponding to that of an energy level transition could stimulate an atom in the upper level to drop to the lower level, in the process stimulating the emission of another photon with the same energy as the first. This idea was a subject of great debate since it was still purely theoretical. Einstein defended the possibility of stimulated emissions using the thermodynamic argument that equilibrium dictates that many more atoms occur in the lower energy levels than the higher energy levels and thus, photons are more likely to encounter an atom in a lower level and be absorbed rather than encounter an atom in a higher energy level and stimulate emission. However, it wasn't until 1928 that the first evidence of stimulated emission was observed when Ladenburg [12] detailed the dispersion of light in certain gases.

In the 1950's, the first concerted effort was made to manufacture a device capable of generating stimulated emissions of light. The first to build a working model demonstrating this idea was Charles H. Townes, a physicist at Columbia University. In 1953, Townes built the maser, a **M**icrowave **A**mplification using **S**timulated **E**mission of **R**adiation apparatus [10]. A precursor to the conventional laser, the maser consisted of a molecular beam split into excited and unexcited portions. The molecules in the excited portion of the beam could be stimulated to emit microwaves when directed into a

specially designed resonant cavity. Thus, Townes was the first to verify experimentally Einstein's theory of stimulated emissions of light.

It was not until 1958 that Townes and Arthur L. Schawlow proposed the idea of the conventional laser in a patent application. However, it was Gordon Gould, a Columbia University graduate student, who was ultimately responsible for coining the term "laser," which is an acronym for **L**ight **A**mplification using **S**timulated **E**mission of **R**adiation [9]. Different from the maser in that the laser operated at lower frequencies in the visible portion of the spectrum, much of the computations necessary to create the laser were done by Townes and Schawlow in 1958. Meanwhile, Gould had set forth to develop the first operational laser but the funding he had been promised by the United States government was withdrawn when federal investigators discovered his past association with Marxist groups. Consequently, Theodore H. Maiman became the first person to demonstrate an operational laser.

Maiman's apparatus consisted of a rod of synthetic ruby with a fully reflective coating on one end and a partially transparent coating on the other end of the crystal. The crystal was surrounded by a helical flash tube used for pumping the ruby crystal. The flash tube acted as a source of optical energy, pumping the ruby crystal such that it would release a short pulse of red light from within the crystal. This pulse of light would reflect from one of the crystal and exit the crystal through the partially transparent coating at the opposite end of the crystal. Before exiting the crystal however, atoms of chromium embedded in the ruby crystal would be stimulated by the optical pumping, adding additional energy to the beam of radiation A specially designed lens was used to collimate the light such that a narrow beam would result from emission. This first operational laser was the catalyst for extensive research involving laser design and development.

In 1961, the first gas laser, a helium-neon (He-Ne) laser, was built at the Bell Telephone Laboratory in California. Originally designed to emit an 1150 nanometer (nm) pulse, it was later redesigned to emit a 632.8 nm beam of red light. The YAG (Yytrium Aluminum Garnet) laser, a chemical version of the gas laser, was developed in 1964 by

J.E Geusic, H.M. Marcos and L.G. Van Uitert, a design that still enjoys great commercial popularity today. The semiconductor laser, which is composed of two pieces of oppositely polarized semiconductor regions (p and n regions), was initially tested in 1962 by a group of scientists from General Electric (GE), International Business Machines (IBM) and Massachusetts Institute of Technology (MIT). This group used a gallium arsenide (GaAs) semiconductor diode cooled to 77 Kelvin pulsed with high current for 3 microseconds to achieve a pulsed output. The development of the semiconductor laser would prove to be one of the most significant accomplishments in the science of laser technology as the versatility and robustness of its design would be of interest to many industries.

Further research in the 1960's was done by William G. Bridges (argon ion laser), C. Kumar Patel (CO_2 laser) and IBM (organic dye laser) [10]. The 1970's saw the creation of the excimer, or excited dimer, laser. This laser device consists of a rare gas atom paired with a halide atom to form a molecule in an excited state. X-ray lasers were researched in the 1980's when x-ray pulsed radiation was discovered during nuclear explosive testing. The x-ray laser as well as the newest laser concept, the free electron laser, continues to be shrouded in secrecy due to their potential military uses. The free electron laser makes use of the "wiggle" concept of negatively charged ions (electron). Physicists have known for many years that passing a beam of negatively charged electrons through a highly polarized magnetic field causes the electrons to rotate or "wiggle" in the direction of the applied field, releasing finite amounts of energy in the process. Subjected to a magnetic field of great enough proportions, this energy release can be harnessed as a directed emission of light.

Today's research focuses on concepts such as tunable lasers, lasers capable of being "tuned " to produce a beam of light at a particular frequency. Semiconductor lasers also continue to be subjects of great interest due to their ease of construction, low cost and reliability. Gas lasers such as the argon, krypton and CO_2 lasers continue to be of great use to many industries in medium and high power applications. Free electron lasers and x-ray lasers are currently being tested and evaluated by the military. In the meantime,

however, scientists and engineers alike are constantly inventing new applications for lasers. It is these new applications that will continue to fuel the need for further laser research in the future.

2.3.2 The Laser – Additional Resources

In addition to the references cited above, Hariharan's text [36] provided a very thorough tutorial of the field of interferometry. Interferometry can best be defined as the interference pattern generated when two beams of light at different frequencies and wavelengths are combined to form a single beam. It will be shown later in this research that, although a laser diode is being used to perform strain measurements, this system differs from the classical interferometer in that no beam splitting devices, reference surfaces or complex phase measurement algorithms are needed. Hariharan does describe an interferomic technique for specimen measurements but the use of beam splitters and additional optics make it much too delicate for the environment in which the SHPB operates.

2.4 Material Science and Circuit Design

This section will detail the remainder of the references used in completing this research. Specifically, research into material science and circuit design techniques was needed in order to better understand the subtleties involved in the dynamic testing of materials as well as the electrical concepts necessary for design and construction of the various circuits needed to power the instrumentation used in this research.

2.4.1 Material Science – Literature Review

A very good review of some of the concerns involved in testing materials at high rates of strain is given by Dharan and Hauser [22]. Besides detailing the Hopkinson-Kolsky method of compressive testing, he also summarizes some of the torsion and tensile tests available to material scientists. He also discusses using the Hopkinson-Kolsky method of material testing in high temperature very low strain rate applications. This theme is

further investigated by Szczepinski, et al [16], who goes into much more detail regarding the response of materials to various types of shock and impact events. Specifically, they investigate the response of these materials on both the microscopic and macroscopic levels. Although they present little experimental data, the theory laid out in their text provides an excellent review of the dynamics involved in material testing at different rates of strain. Shigley and Mitchell [1] provide a summary of material testing at quasi-static states of stress and strain. This reference served only to relate conventional methods of material testing to the Hopkinson Bar and other methods of testing materials at elevated rates of strain.

Graham [14] and Bell [21] provide additional insight into the high-pressure shock compression of condensed matter. These authors present a mix of experimental data and the related theory in a fashion well suited to physicists and material scientists. However, for this research, these references provided a brief review of the electrical, chemical and mechanical characteristics of different materials subjected to high-pressure shock events such as they encountered in the Hopkinson Bar.

2.4.2 Circuit Design – Literature Review

Much of the information needed to properly design the various electronic circuits needed in this research came from internet sources such as National Semiconductor [37] and Burr-Brown [38] web sites. These manufacturers make available a series of technical articles written by their engineers on a variety of subjects, including instrumentation amplifier design and voltage regulator considerations. These references proved to be very valuable to this research as noise-rejection and stable power supplies could have significant impact on the experimental results.

Other sources of information came from Beckwith and Marangoni [13] and Hambley [11], both of whom present a series of circuit design and analysis techniques. Beckwith is far less theoretical in nature than Hambley but he does a fine job relating the theory to specific engineering applications. Hambley dedicates his text to the design of specific

circuits for specific applications. Although his text is written for the computer-aided circuit designer, all of the circuits he specifies are laid out in conventional drafting format for easy interpretation. In short, these two references proved to be extremely useful in the design of the circuitry necessary to conduct this research.

Chapter 3. Fundamentals

3.1 Introduction

In this chapter, the governing principles of the SHPB and laser science will be discussed. The SHPB is one of many methods of testing materials at medium rates of strain. However, the majority of these experimental techniques utilize the same engineering principles in order to perform the experiment and simplify the interpretation of the results. Some of these principles include one-dimensional wave propagation, uniaxial stress, homogeneous deformation and the conservation of momentum. These ideas will be related to the SHPB via the development of the equations governing the experiment. The equation of motion for a differential element will be computed before generating equations for the specimen stress, strain and strain rate. The development of the equations presented here will be similar to the style used by Kaiser [18] in that a single differential element will be analyzed to derive the necessary equations.

As opposed to the SHPB, laser technology is a relatively new and dynamic area of study. Its potential is still being investigated as newer and better instrumentation and processing techniques become available. Although lasers have been in existence for over 40 years, recent advancements in laser science and signal processing have allowed lasers to be used in more applications than ever before. Examples of these new applications include Doppler measurements, surface mapping, data transmission and material processing. The different types of lasers as well as their different applications will be discussed after a condensed explanation of the principles governing the laser. In addition, instrumentation issues concerning the electrical resistance strain gage and related circuitry including the Wheatstone bridge and instrumentation amplifier will be reviewed.

3.2 The Split Hopkinson Pressure Bar

As detailed earlier in this thesis, the Hopkinson Bar has been in existence since the early 1900's when Bertram Hopkinson devised the experiment to test the response of steel

billets to high-amplitude impacts [2]. Since then, many derivatives of Hopkinson's experiment have been developed. One of the more popular derivatives is the Split Hopkinson Pressure Bar (SHPB). Before proceeding with the development of the equations governing the experiment, a more detailed description of the apparatus is in order.

Figure 3.1 below shows a simplified schematic of the split Hopkinson pressure bar experiment.

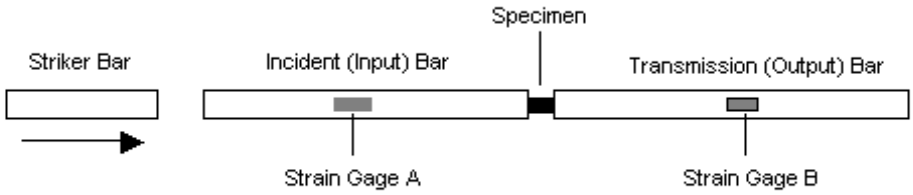

Figure 3.1 Split Hopkinson Pressure Bar Experiment

To review the experiment, the pressure gun fires the striker bar at the input bar, generating a compressive stress wave that travels the length of the input bar to the input bar – specimen interface. At this interface, a portion of the wave is transmitted through the specimen and into the output bar. The remainder of the original compressive wave reflects back into the input bar. Strain gages mounted on the input and output bars measure the strain encountered at each of the input and output bars. This strain data is recorded on a digital oscilloscope or similar equipment such that the strain versus time signal can be manipulated to yield specimen stress and strain as well as strain rate. Typically, the strain rate for the SHPB is limited to10^4 s^{-1}. This upper strain rate limitation is the consequence of a number of factors including

1. The effects of mechanical dispersion on signal resolution
2. Input bar length-to-diameter ratio requirements for 1-dimensional wave propagation theory and uniaxial stress, homogeneous deformation
3. Pressure bar length requirements to ensure separation of the input bar signal

Longitudinal wave dispersion has adverse effects on all conventional SHPB experiments. According to Burstow, et al [39], the SHPB is limited at medium rates of strain by its time resolution of approximately 1μs caused by acoustic dispersion. Dispersion is best defined as the wave propagation velocity dependence on frequency. In essence, the impact caused by the striker bar impact excites many different frequencies within the input bar. Each of these component frequencies travels at a different velocity within the input bar, causing an oscillation or "ripple" in the time history recorded by the strain gage. This introduces an undesirable amount of uncertainty in the signal in that the peak strain is no longer apparent.

Another important consideration in the SHPB is the geometry of the pressure bars, particularly the input bar. Also known as the incident bar, the input bar "delivers" the mechanical stress wave to the test specimen. A portion of this wave is transmitted into the specimen while the remainder is reflected back into the input bar. The length and diameter of the input bar is critical in enforcing the assumptions of uniaxial stress, homogeneous deformation in the specimen and elastic behavior in the incident pressure bar. In order to insure that uniaxial, homogeneous deformation is generated in the specimen while the peak stress in the pressure bar is well below its elastic limit, Equation 3.1 must hold true:

$$\frac{L}{d} \geq 11 \qquad \textbf{(3.1)}$$

In other words, the input bar length-to-diameter must be greater than 10. Also, in order to insure that the incident and reflected pulses in the input pressure bar can be separated, the bar diameter must be at least twice the wavelength of the initial compressive wave. Typical bar dimensions are 0.50" – 0.75" in diameter by 60.00" – 72.00" in length. NSWCDD's most frequently used pressure bars are 0.75" in diameter by 60.00" in length. Later in this chapter, it will be shown that specimen strain rate $\dot{\varepsilon}$ is inversely proportional to the length of the pressure bar. Thus,

$$\dot{\varepsilon} \propto K * \frac{1}{L} \tag{3.2}$$

where K is a constant of proportionality. Accordingly, in order to achieve strain rates greater than approximately 10^4 in/in-s would require pressure bars with very small lengths and diameters. However, as will be shown later in this chapter, experimentation becomes impractical with pressure bar diameters much less than 0.25" due to the decreased size of the pressure bars and, more importantly, the decreased diameter of the test specimen.

In addition to the geometry considerations presented above, precise specimen positioning and alignment also play important roles in the deformation event. In order to insure that homogeneous deformation occurs, the ends of the specimen are greased with a silicon-based lubricant to reduce the frictional coefficient at the pressure bar-specimen interfaces [8]. Also, some method of ensuring that the specimen is centered between the pressure bars and that it is perfectly aligned longitudinally with the pressure bars is needed. These experimental methods will be discussed further in Chapter 4. Failure to meet these conditions can result in non-uniaxial stress and non-homogeneous deformation.

Before any experimentation can begin, the researcher must first specify the total strain applied to the specimen. This strain value can then be used, along with the physical dimensions of the specimen and specimen stress constant, to compute the necessary parameter for setting up the experiment to yield the desired strain. These computations will be developed in the following section. Typical test results are shown below in Figures 3.2 and 3.3. Figure 3.2 shows a typical input bar strain history while Figure 3.3 depicts a typical output bar strain history.

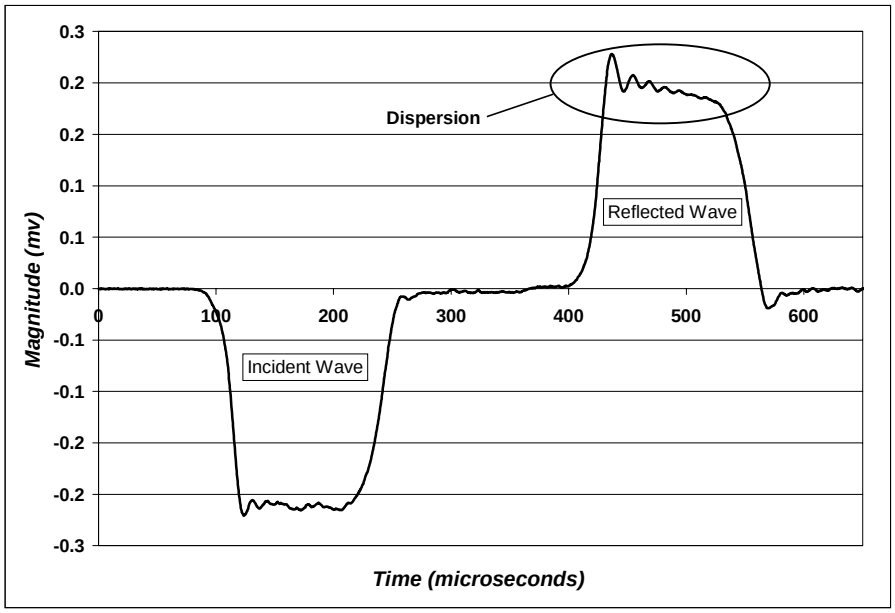

Figure 3.2 Typical Input Bar Strain History

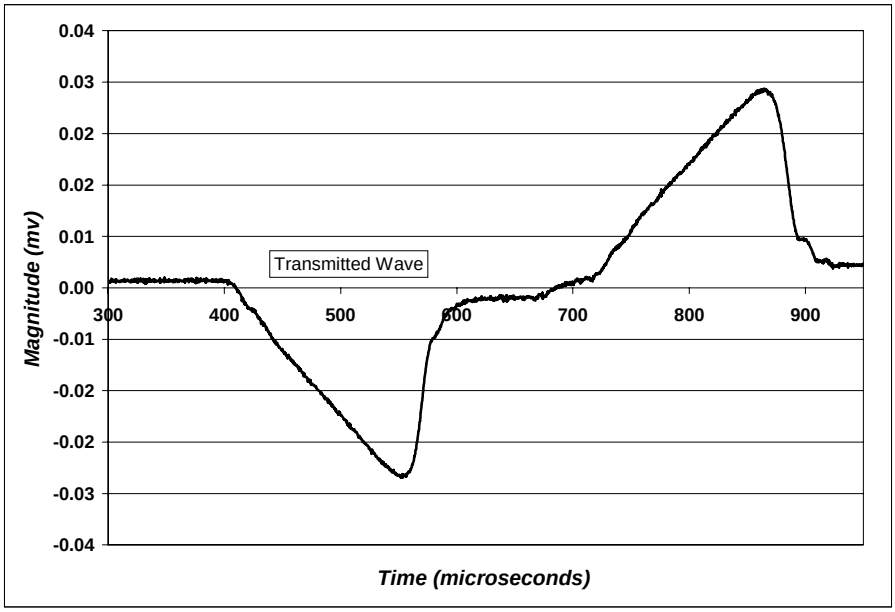

Figure 3.3 Typical Output Bar Strain History

Note the dispersive effects shown in the input bar strain history in Figure 3.2. Dispersion appears as an oscillation at the peak strain regions and has the effect of distorting the data

by altering the peak strain but also by attenuation of the signal. This attenuation is particular apparent in the reflected pulse. The effects of dispersion can be accounted for in a variety of ways, including using tabulated dispersive corrective values [5] as well as modeling the dispersive effects numerically [18]. Alternatively, these dispersive effects can be lessened or, possibly, completely removed via the use of an instrumentation system that measures strain directly at the specimen. This is the primary motivation behind this research.

3.2.1 Dynamic Analysis of the SHPB

In order to understand the dynamics of the event, it is necessary to consider a single, differential element *dx* of a long rod of cross sectional area *A*, density ρ and Young's Modulus *E*. As specified by the experiment, the rod is subjected to an impact along its longitudinal axis. Figure 3.4 illustrates the differential element of the rod along with the coordinate system chosen for this analysis.

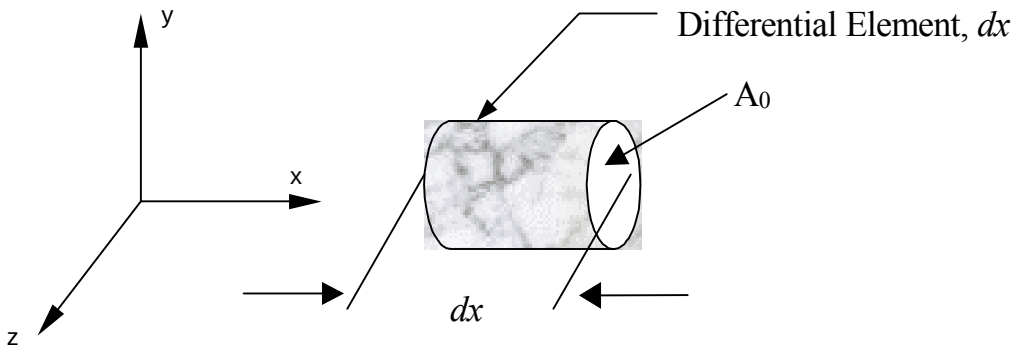

Figure 3.4 Differential Element of a Cylindrical Rod

In Figure 3.4 above, the differential element *dx* has an initial cross sectional area A_0. Subjecting the bar to a compressive stress yields Figure 3.5, differential element *dx* in a uniaxial state of compression.

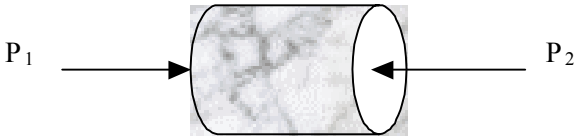

Figure 3.5 Differential Element *dx* in Uniaxial Compression

Assuming perfectly elastic behavior in the pressure bars (this assumption will be qualified later in this chapter), the compressive forces P_1 and P_2 can be related to the specimen engineering stress σ by Equation 3.3:

$$\sigma = \frac{P}{A_0} \tag{3.3}$$

Equation 3.3 merely states that engineering stress is equal to force per initial specimen area. This stress is related to the specimen strain through Hooke's Law, as shown below in Equation 3.4:

$$E = \frac{\sigma}{\varepsilon} \tag{3.4}$$

As stated previously in Chapter 1, this linear relationship is only valid for purely elastic behavior. Continuing with the analysis, the specimen strain ε can be redefined in terms of specimen particle displacements u_1 and u_2 such that

$$P_1 = A_0 E \frac{\partial u_1}{\partial x} \tag{3.5}$$

$$P_2 = A_0 E \frac{\partial u_2}{\partial x} \tag{3.6}$$

In 3.5 and 3.6, the quantities $\frac{\partial u_1}{\partial x}$ and $\frac{\partial u_2}{\partial x}$ represent the specimen strain at each boundary condition. As shown in Figure 3.3, the forces P_1 and P_2 constitute a uniaxial load set acting in compression. Consequently, using the same axis system set for the in Figure 3.2, $P_1 = -P_2$, or

$$A_0 E \frac{\partial u_1}{\partial x} = -A_0 E \frac{\partial u_2}{\partial x} \tag{3.7}$$

Returning to the original differential element, the forces on the element can be summed according to Newton's 2nd Law. Again, the coordinate system assumed in Figure 3.2 will be used in this analysis. Summing the compressive and inertial forces yields

$$\sum F = m\,a \tag{3.8}$$

$$A_0 E \frac{\partial u_1}{\partial x} - A_0 E \frac{\partial u_2}{\partial x} = A_0 \rho dx \cdot \frac{d^2 u_1}{dt^2} \tag{3.9}$$

where ρ is the density of the pressure bar material and $\frac{d^2 u_1}{dt^2}$ is the particle acceleration within the element. In addition to the uniaxial, elastic deformation assumptions made above, it is also assumed that the bar material is homogeneous across its cross section. With this in mind, Equation 3.9 can be simplified as follows:

$$C_0^{\,2}\left(\frac{\partial u_1}{\partial x} - \frac{\partial u_2}{\partial x}\right) = \frac{d^2 u_1}{dt^2} \cdot dx \tag{3.10}$$

In Equation 3.10, the term C_0 is defined as the longitudinal wave velocity in the differential element. Numerically, it is defined as $C_0 = \sqrt{\frac{E}{\rho}}$. Again, E is the elastic

modulus and ρ is the density of the element. Equation 3.10 is the fundamental equation of motion for the differential element. Using the principles of the conservation of momentum as well as the assumptions set forth at the start of this analysis (homogeneous, uniaxial deformation), further simplifications can be made. In terms of specimen displacements, u_2 can be defined in terms of u_1 as follows:

$$u_2 = u_1 + \frac{\partial u_1}{\partial x} \cdot dx \tag{3.11}$$

Differentiating this equation yields the particle spatial rate of change at interface 2 defined in terms of u_1 and u_2:

$$\frac{\partial u_2}{\partial x} = \frac{\partial u_1}{\partial x} + \frac{\partial^2 u_1}{\partial x^2} \cdot dx \tag{3.12}$$

Finally, substitution of Equation 3.12 into the equation of motion for the differential element *dx* (Equation 3.10) yields Equation 3.13:

$$C_0^{\,2} \frac{\partial^2 u_1}{\partial x^2} = \frac{d^2 u_1}{dt^2} \tag{3.13}$$

Equation 3.13 is the simplified equation of motion for the single differential element *dx* of the homogeneous, uniaxially deforming cylindrical rod. Although this equation has little practical use in the overall analysis, it will be used as an aid in simplifying the equations defining the specimen stress, strain and strain rate. This will be accomplished in the next several sections.

3.2.2 SHPB Specimen Stress Development

The motivation behind the SHPB is the determination of the mechanical properties of a dynamically loaded test specimen. Since the dynamic loading results in deformations well beyond the elastic (linear) limits, properties such as elastic modulus and shear

modulus are not applicable mechanical measures in the plastic deformation regime. Thus, specimen stress and strain at the corresponding elevated rate of strain are needed in order to completely define the mechanical properties of materials at non-quasi-static rates of strain. With this data, the familiar stress versus strain diagram can be generated for the plastic deformation regime.

In order to arrive at an equation for the specimen stress, it is necessary to consider the forces imparted on the specimen during the initial loading of the SHPB. This is shown below in Figure 3.6.

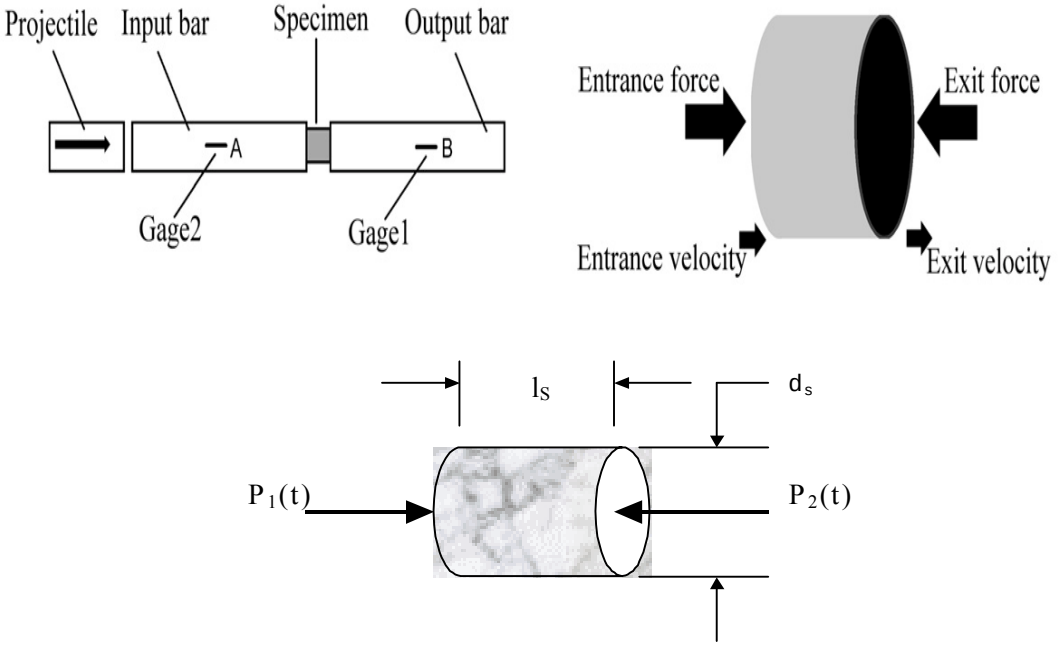

Figure 3.6 Cylindrical Specimen in Uniaxial Stress State

In Figure 3.6, the forces $P_1(t)$ and $P_2(t)$ are the result of the contact between the input and output pressure bars and the test specimen and d_s and l_s are the diameter and length of the test specimen, respectively. These forces are shown as functions of time since, during the dynamic event, the forces vary during the loading and unloading of the specimen. Noting that the forces developed in the specimen are compressive in nature, the average specimen stress can be computed according to Equation 3.3. Thus

$$\sigma_{AVG}(t) = \frac{\frac{P_1(t) + P_2(t)}{2}}{A} \tag{3.14}$$

or,

$$\sigma_{AVG}(t) = \frac{P_1(t) + P_2(t)}{2 \cdot \frac{\pi d^2{}_s}{4}} \tag{3.15}$$

Equations 3.14 and 3.15 are actually relations for the average specimen stress as the specimen is originally in an equilibrium state prior to the application of the uniaxial load. Analyzing the equilibrium state of the specimen during the loading event, the forces $P_1(t)$ and $P_2(t)$ can be replaced by the corresponding incident and reflected pressure bar strains. Consequently, with a pressure bar diameter d_{Bar},

$$P_1(t) = E[\varepsilon_1(t) + \varepsilon_2(t)] \cdot \frac{\pi d^2{}_{Bar}}{4} \tag{3.16}$$

$$P_2(t) = E[\varepsilon_T(t)] \frac{\pi d^2{}_{Bar}}{4} \tag{3.17}$$

In Equation 3.16 and 3.17, $\varepsilon_I(t)$ is the input bar incident strain signal, $\varepsilon_R(t)$ is the input bar reflected strain signal and $\varepsilon_T(t)$ is the transmitted strain signal. In order to generate a more useful equation, the average specimen stress must be related to the incident, reflected and transmitted strain histories $\varepsilon_I(t)$, $\varepsilon_R(t)$ and $\varepsilon_T(t)$. This can be accomplished by substitution of Equations 3.16 and 3.17 into Equation 3.12. The simplified result of this substitution is shown below in Equation 3.18:

$$\sigma(t) = \frac{E d^2{}_{Bar}}{2 d^2{}_S} [\varepsilon_I(t) + \varepsilon_R(t) + \varepsilon_T(t)] \tag{3.18}$$

Recalling one of the primary assumptions made in this analysis, namely that of uniform uniaxial deformation, conservation of momentum requires that the total strain in the input bar ($\varepsilon_I + \varepsilon_R$) equals the total strain in the output bar (ε_T). Thus,

$$\varepsilon_I(t) + \varepsilon_R(t) = \varepsilon_T(t) \tag{3.19}$$

Substitution of 3.19 into 3.18 yields the simplified equation for average specimen stress:

$$P_2 = A_0 E \frac{\partial u_2}{\partial x} \tag{3.20}$$

Thus, the average specimen stress is proportional to the total strain transmitted through the specimen. It also shows that changing the average stress imparted on the specimen is accomplished simply by changing the ratio of the pressure bar-specimen diameter. This will serve as the primary equation for calculating average specimen stress throughout the rest of this analysis.

3.2.3 Specimen Strain and Strain Rate

To derive the expressions for the specimen strain and strain rate, it is necessary to review the equation of motion of a differential element in the uniformly deforming, uniaxially loaded bar:

$$C_o^2 \frac{\partial^2 u_1}{\partial y^2} = \frac{\partial^2 u_1}{\partial t^2} \tag{3.21}$$

Assuming that the stress and strain are harmonic in nature, the particle acceleration in Equation 3.21 can be rewritten in terms of the particle velocity, *v*:

$$\frac{d^2 u_1}{dt^2} = \frac{dv}{dt} \tag{3.22}$$

Further simplification yields Equation 3.23

$$E \cdot \frac{\partial}{\partial x}\left(\frac{\partial u_1}{\partial x}\right) = \frac{\partial p}{\partial x} \tag{3.23}$$

in which p is the pressure across the homogeneous cross section. Finally, the equation of motion can be rewritten in terms of the pressure and velocity across the bar cross section as

$$-\frac{\partial p(x,t)}{\partial x} = \rho \frac{\partial v}{\partial t} \tag{3.24}$$

Notice from Equation 3.24 that to solve for the particle velocity in a bar requires knowledge of the pressure in the bar. If we assume a positive traveling harmonic wave of the form

$$p(x,t) = Pe^{i(\omega t - kx)} \tag{3.25}$$

in which P is the amplitude of the pressure pulse, ω is the pulse frequency, t is the temporal index, k is the wave number ($k = \frac{\omega}{C_o}$), and x is the spatial location of the wave, an expression for the instantaneous particle velocity can be computed. Taking the first derivative of Equation 3.21 with respect to x, Equation 3.26 results:

$$\frac{\partial p(x,t)}{\partial x} = -ikPe^{i(\omega t - kx)} \tag{3.26}$$

Substitution of 3.26 and 3.7 into Equation 3.24 yields

$$ikPe^{i(\omega t - kx)} = \rho i \omega v(x,t) \tag{3.27}$$

Equation 3.27 may then be rearranged and simplified to yield the particle velocity *v*, shown below in Equation 3.28.

$$v(x,t) = \frac{k}{\rho\omega} P e^{i(\omega t - kx)} \tag{3.28}$$

Substituting $k = \frac{\omega}{C_0}$ and *p(x,t)* back into Equation 3.28 yields

$$v(x,t) = \frac{1}{\rho C_o} p(x,t) \tag{3.29}$$

For the uniaxial, elastic state of stress found in the pressure bars, the pressure is equal to the applied load divided by the cross sectional area of the pressure bar. Therefore, *p(x,t)* can be written in terms of the bar strain as

$$p(x,t) = \varepsilon(x,t)E \tag{3.30}$$

Substitution of Equation 3.30 into Equation 3.29 yields an expression for the particle velocity in terms of the pressure bar strain, as shown below by Equation 3.31:

$$v(x,t) = C_o \varepsilon(x,t) \tag{3.31}$$

Before proceeding further, it is necessary to recall the dynamics of the SHPB. At the input bar-specimen interface, the stress pulse is partially transmitted and partially reflected. As such, the reflected wave now behaves as a tensile stress pulse since it is traveling in the opposite direction of the incident pulse. Thus, for a wave propagating in the opposite (-x) direction, the instantaneous particle velocity *v* is merely the inverse of 3.31, namely

$$v(x,t) = -C_o \varepsilon(x,t) \tag{3.32}$$

With instantaneous particle velocity equation now written in terms of the pressure bar strains, specimen strain rate can be calculated. Referring back to the test specimen shown in Figure 3.4, Equations 3.30, 3.31 and 3.32 can be combined to generate Equation 3.33, the average instantaneous strain rate in the test specimen:

$$\frac{d\varepsilon}{dt} = \frac{v_{SO} - v_{IS}}{l_S} \tag{3.33}$$

In Equation 3.33, v_{IS} is the particle velocity at input bar - test specimen interface while v_{SO} is the particle velocity at the test specimen – output bar interface. Recall also that l_S is the length of the test specimen. The velocity at the input bar – test specimen interface (v_{IS}) is comprised of the incident wave (+x direction) and the reflected wave (-x direction). Thus,

$$v_{IS} = C_o(\varepsilon_I - \varepsilon_R) \tag{3.34}$$

Computation of the velocity at the test specimen – output bar interface (v_{SO}) follows in much the same fashion as input bar – test specimen velocity calculation except that only the transmitted strain history ε_T is needed. Thus,

$$v_{SO} = C_o \varepsilon_T \tag{3.35}$$

By substituting these interface velocities into the expression for the specimen strain rate, an expression for the specimen strain rate in terms of the pressure bar strains can be found. This is shown below in Equation 3.36:

$$\frac{d\varepsilon_{Specimen}}{dt} = -\frac{C_o(\varepsilon_T - \varepsilon_I + \varepsilon_R)}{l_S} \tag{3.36}$$

The negative sign in 3.36 is due to the fact that the test specimen is in a state of compression. Since the uniformly, uniaxially deforming specimen assumption is still in use, Equation 3.19 still holds true and Equation 3.36 can be reduced to

$$\frac{d\varepsilon_{Specimen}}{dt} = -\frac{2C_o}{l_S}\varepsilon_R \tag{3.37}$$

With the equation defining the specimen strain rate known, the specimen compressive strain can be found through integration of Equation 3.37:

$$\varepsilon_{Specimen}(t) = -\frac{2C_o}{l_S}\int \varepsilon_R(t)dt \tag{3.38}$$

Equations 3.37 and 3.38 will form the basis for calculation of specimen strain rate and strain throughout this research. Coupled with the equation for specimen stress (3.20), these three relationships provide the SHPB scientist with a means to characterize the mechanical properties of materials using conventional strain gage instrumentation at strain rates up to and including 10^4 in/in-s.

3.3 Light Amplification by Stimulated Emission of Radiation

Laser is an acronym for **L**ight **A**mplification by **S**timulated **E**mission of **R**adiation. As detailed earlier in Chapter 2, laser science has been around since the middle of the twentieth century. However, it was not until the development of the semiconductor laser that their usage became more widespread. Common applications of the semiconductor laser include barcode scanners, compact disc players and laser printers. Since the thrust of this research centers on the application of a semiconductor laser in the SHPB, a brief review of laser phenomenon. In addition, several related applications of laser science will be presented.

3.3.1 Fundamentals of Light

In its simplest sense, light is nothing more than electromagnetic radiation that possesses both wave-like and particle-like properties (the so-called dual nature of light). The wave-like nature of light consists of orthogonal electric and magnetic fields, oscillating simultaneously. Typically, this radiation is characterized by its frequency f and wavelength λ. The speed with which these waves propagate is the speed of light, denoted as c. In a perfect vacuum, c is equal to 3 x 10^{10} cm/sec. In media other than a true vacuum, the speed of light can be computed as shown in Equation 3.39:

$$v = \frac{c}{n} \tag{3.39}$$

In Equation 3.4, v is the medium-corrected speed of light while n is the refractive index of the particular medium. Table 3.1 below lists some of the more commonly used refractive indexes:

Table 3.1 Refractive Indexes of Common Materials at Selected Wavelengths

Material	Wavelength (μm)	Refractive Index, n
Air	0.59	1.0002765
Pure Water	0.59	1.33287
Optical Glass	0.58	1.4580
NaCl	0.59	1.49482

Thus, in any given medium, all electromagnetic radiation travels at the same speed, differing only in wavelength and frequency. Equation 3.40 below relates the frequency, wavelength and velocity:

$$\lambda f = v \tag{3.40}$$

As shown in Equation 3.40, wavelength decreases with increasing frequency. Table 3.2 below lists the wavelength and frequency ranges for some common types of electromagnetic radiation:

Table 3.2 Frequency and Wavelength of Common Types of Radiation

Radiation Type	Frequency (Hz)	Wavelength
Gamma Rays	$>10^{18}$	<0.1 nm
X-Rays	$10^{17} – 10^{18}$	0.1 nm – 10 nm
Ultraviolet	$10^{15} – 10^{16}$	10 nm – 500 nm
Visible Light	$\sim10^{15}$	600 – 950 nm
Infrared	$10^{12} – 10^{14}$	1 – 1000 μm
Microwave	$10^{9} – 10^{12}$	0.1 cm – 1 m
TV	$10^{7} – 10^{8}$	1 – 100 m
Radio	$10^{4} – 10^{5}$	100m – 100 km

As opposed to ambient light that consists of light of many frequencies and wavelengths, light that possesses the characteristic of a single wavelength is called monochromatic. Light sources that are classified as monochromatic are typically expensive to produce and are used only in highly specialized applications. Lasers are a modern-day example of monochromatic light sources [17].

In addition to its wave-like properties, light also acts as particles or quanta of energy called photons. Each photon carries a discrete amount of energy proportional to its frequency. This discrete amount of energy E is given in Equation 3.41.

$$E = hf \tag{3.41}$$

In 3.41, E is the discrete amount of energy carried by the photon, h is Planck's constant (h = 6.6 x 10^{-27} erg-sec) and f is the frequency of the light. Thus, particles oscillating at higher frequencies contain greater amounts of energy than lower frequency particles.

In the field of laser science, also known as quantum electronics, both the wave-like and particle-like properties of light are observed. As will be detailed in the next section, particle transitions from a higher quantum level to a lower quantum level in the presence of additional high quantum level particles is the driving force behind stimulated emissions. In addition, the stimulated emission can be harnessed to produce a highly coherent, monochromatic (sharply defined wavelength) beam. This practical example illustrates the aforementioned dual nature of light and will be a key to the understanding of the fundamentals of laser science.

.

3.3.2 Fundamentals of Laser Science

As discussed in Chapter 2, Albert Einstein first postulated the idea of stimulated emission of radiation in 1916. Einstein's idea was that "a photon with energy corresponding to that of an energy level transition could stimulate an atom in the upper level to drop to the lower level, in the process stimulating the emission of another photon with the same energy as the first" [10].

As printed previously, the term laser is an acronym for **L**ight **A**mplification by **S**timulated **E**mission of **R**adiation. Laser light is typically found in the ultraviolet, visible and infrared portions of the spectrum, that is, with wavelengths ranging from 10 - 10^6 nm with frequencies ranging from 10^{13} -10^{15} Hz. Typical industrial lasers, however, are found in the narrow wavelength range of 500 – 10,000 nm. An important characteristic and perhaps the most appealing reason why lasers are used is the monochromatic light generated by stimulated emissions [12]. This will be explained in greater detail further into this chapter.

Common to all types of lasers are three key components:

1. Energy (pumping) source
2. Amplification medium
3. Resonating cavity

Energy sources used in typical lasers include electrical current, light generating flash tubes as well as light from other lasers. Amplification media consist of gases, dyes and even p-n junctions in the case of the semiconductor laser. The resonating cavity usually consists of a fully reflective mirror (for amplification) and a partially reflecting mirror (for emission). With these three integral components, the typical laser takes the form shown below in Figure 3.7:

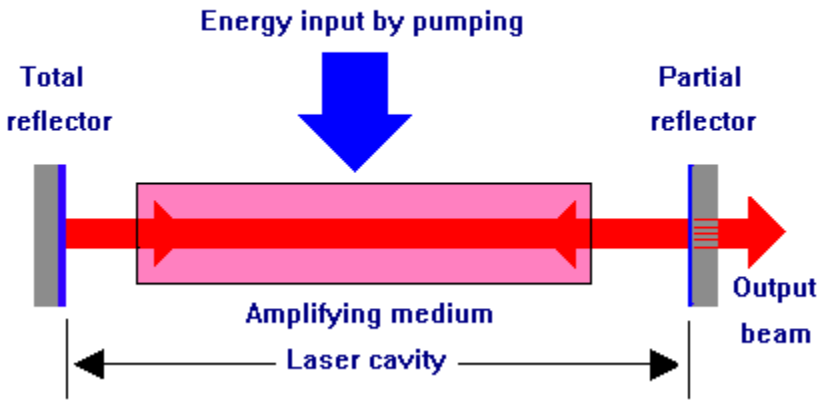

Figure 3.7 Simplified Schematic of a Typical Laser [24]

In Figure 3.7 above, the energy input can be continuous, resulting in a continuous line of laser light, or pulsed to provide a pulsed output. As detailed in the previous section, the emission of a photon can also be stimulated by the mere presence of a photon with the same energy level as the transition, such as the photons generated via spontaneous emissions. Thus, the energy input through pumping coupled with the spontaneous emissions naturally occurring within the lasing material with the material triggers stimulated emission. As the stimulated photons propagate through the resonant cavity, their mere presence induces additional stimulated emission, resulting in a cascade of stimulated emissions. These emissions can be collimated through the use of a properly

sized aperture to produce a highly coherent, monochromatic beam of light as opposed to the light generated by spontaneous emissions.

The concept by which laser light is possible is the idea of stimulated emissions, first theorized by Einstein in 1911. Excited species can release their excess energy by non-radiative processes including collisions with other atoms as well as radiative processes including spontaneous and stimulated emissions. In colliding with other atoms or molecules, this excess energy is released in the form of kinetic and thermal energy. As for spontaneous and stimulated emissions, this excess energy is released in the form of optical energy. In the case of spontaneous emissions, the excited photon drops to a lower energy level without outside interference. In this case, the energy is released as a result of natural decay to the lower energy level, similar to the half-life decay of radioactive isotopes. Spontaneous emissions of light include most ambient light, including sunlight. As for stimulated emissions, emission of a photon and transition to a lower energy level can be stimulated by the presence of a photon with the same energy level as the transition. The photons are inherently present in the form of spontaneous emissions from higher energy levels. In effect, the first several spontaneously emitted photons trigger stimulated emission of other photons, leading to a cascade of stimulated emissions. This stimulated emission produces light of the same wavelength as the original photon and light that is highly coherent (in phase) with the original light.

In practice, stimulated emissions are rare due to the same reason that spontaneous emissions are more common: species tend to drop to the lowest available energy level. Thermodynamic equilibrium dictates that the population of a state tends to decrease as its energy increases [17]. This states that there should always be a larger population in the lower state of transition than in the higher state. Thus, a photon is more likely to be absorbed by a lower-state species than to stimulate emission from another in the higher state. For this reason, spontaneous emission is the dominant mechanism of transition.

In order to force stimulated emission to dominate, a population inversion is needed. In other words, the population of the upper level of transition needs to be greater than

population of the lower transition level. With a population inversion, a photon at the higher transitional energy level would be more likely to stimulate emission from the excited state than to be absorbed by the lower state. The net result would be amplification or gain in the number of photons with the transition energy, corresponding to the difference between stimulated emission and absorption at that particular wavelength. The gain produced by the presence of the population inversion is typically known as laser gain and is measured as a percentage increase per pass through the laser medium. It can also be given as the number of added photons per unit distance traveled. In any case, the population inversion must be maintained in order for lasing action to continue. Thus, the lower energy level of transition must be depopulated as the higher energy level is populated.

3.3.3 Fundamentals of the Semiconductor Laser Diode

Carrier injection across a pn junction as a means for achieving stimulated emissions in semiconductors was first proposed in 1953 and first demonstrated in 1962 [17]. As with a typical semiconductor, the pn junction is the driving force behind the semiconductor laser diode. The p-region consists of a semiconductor material such as silicon (Si) or gallium arsenide (GaAs) "doped" with an element that has at least one less electron than the host material. An example of this would be the doping of a Si crystal with aluminum (Al). Since the Al atom has 3 valence electrons compared to silicon's 4 valence electrons, a "hole" is formed in the valence band. The n-region is the polar opposite of the p-region. In forming an n-type semiconductor region, the host material is doped with an element having at least one more electron than the host material. An example of an n-type semiconductor would be the doping of Si (4 valence electrons) with As (5 valence electrons), creating a net negatively charged region that has the capability to carry current via the extra electron. These two junctions are incorporated into a single-crystal semiconductor block, separated by an active layer and mounted to a substrate wafer. Figure 3.8 below illustrates the configuration of a typical semiconductor laser.

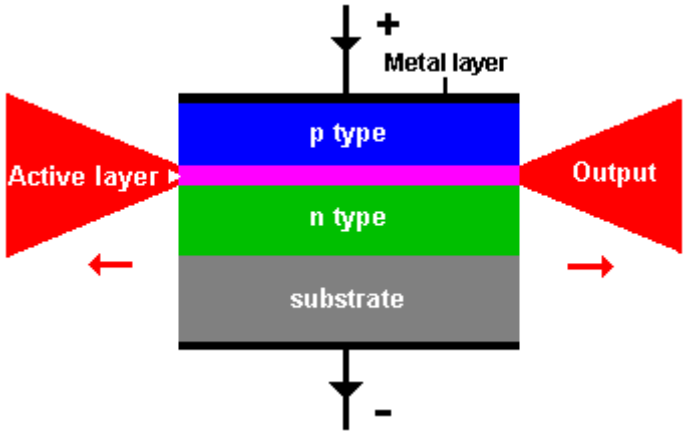

Figure 3.8 Typical Semiconductor Laser Diode [24]

Figure 3.8 above shows the p-type semiconductor material isolated from the n-type semiconductor material by the active layer. This active layer is the region in which the electrons and holes recombine to generate stimulated emission. This process is initiated by the injection of a forward bias current into the active region. Forward biasing, in this case, dictates that the voltage applied to the p region be positive with respect to the voltage applied to the n region. This current causes the internal potential barriers within the active junction to weaken, allowing the holes and electrons to permeate into the active layer where the recombination process causes spontaneous emission to occur. To enhance and amplify the light emitted by the diode laser and provide the optical feedback necessary for continuous lasing action, the both ends of the active region are cleaved to form a Fabry-Perot optical cavity. The Fabry-Perot cavity, typically 1-10 μm wide by 200-300 μm long by 0.1-0.2 μm thick, consists of a fully reflective surface opposite a partially reflective surface such that the light generated by stimulated emission will be directed through the recombination process before exiting the cavity in the form of laser light. The recombination process acts as a source of optical pumping, further fueling the ongoing lasing action and providing for self-sustaining emission. The small size of the optical cavity minimizes the current needed for sustained stimulated emission. And, although a significant amount of energy is released as heat, enough energy is present in the form of light to generate a highly coherent, monochromatic beam of light [10].

Coherence is the ability for light to remain in phase with itself over finite distances. As opposed to ambient light that exhibits 100% divergence, coherent light sources exhibit approximately 1-2% divergence. Thus, many lasers can generate light with a wavelength range of less than 10 nm and coherent lengths of up to 200 m. Typical semiconductor lasers, however, are multimode, semi-monochromatic light sources with coherent lengths of approximately 200 cm [12].

3.3.4 Industrial Applications of Lasers

As the intent of this research implies, it is desired to use a semiconductor laser diode in an application similar to classical interferomic techniques in that the diameter of a test specimen can be measured before, during and after a medium strain rate event. This application differs from classical interferometry in that no beam splitter, reference beam or phase comparison computations will be used. Figure 3.9 below illustrates an example of the classical Michelson Interferometer, first demonstrated by Albert A. Michelson.

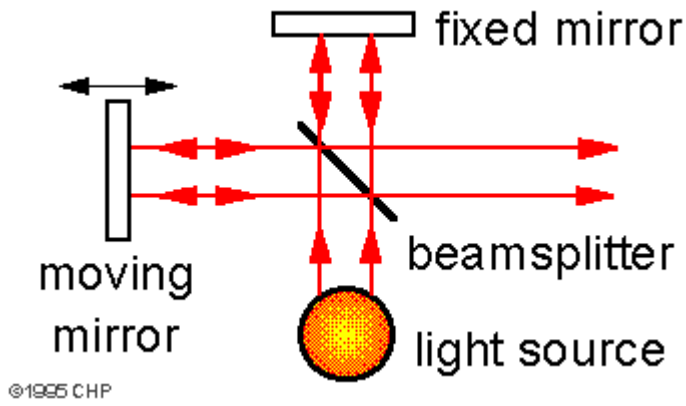

Figure 3.9 Classical Interferomic Measurement Technique [24]

As shown above, typical interferomic applications utilize a beam splitter in order to separate the laser beam into two individual beams, of which one will act as the measurand and the other will serve as a reference. The portion of the beam that reflects from the surface of interest is recombined with the reference beam at a photodetector.

These two combined beams interfere either constructively (bright) or destructively (dark), depending on the number of wavelengths by which their paths differ [13]. Since variations in this pattern are directly related to the variations on the surface, processing this signal can yield displacement, velocity and even strain data, to name but a few applications. An additional application involves moving the reference surface in a harmonic fashion to provide a phase shift between the reference and the measurement beams. This enables to the user to generate a surface profile of the object being measured.

Another common application of the laser utilizes the "Doppler Effect [9]." It is known that the frequency shift of scattered light is directly proportional to its velocity. That is, the frequency of light scattered by an object relative to a velocity source is changed by an amount that depends on the velocity and the scattering geometry. In essence, this shift can be quantified by Equation 3.49:

$$\frac{\Delta f}{f} = \frac{2\upsilon}{c} \qquad \textbf{(3.49)}$$

In Equation 3.49, f refers to the frequency of the light source, υ is the speed of the object being measured and c is the speed of light. Since the speed of the front is so much smaller than the speed of light, Δf will be a small percent of the original frequency of the light. For example, a velocity of 1500 cm/sec (nearly 30 miles/hour) results in a frequency shift of 10^8 Hz.

Additional applications of laser technology include fiber optic data transmission and communications networks, laser printers, compact disc players and barcode scanners, to name just a few. Although each of these applications differs significantly, each takes advantage of the laser's ability to generate a highly coherent, monochromatic beam of optical energy.

3.4 Instrumentation in the Split Hopkinson Bar

The primary goal of this research is to investigate the feasibility of replacing a portion of the conventional strain gage instrumentation system with an optical measurement system. It is anticipated that such a system would provide better resolution and higher degrees of accuracy and robustness by reducing the amount of data recorded with strain gages, thereby ridding the data of the errors inherent to remote mounted strain gages as well as the inaccuracies due to longitudinal bar dispersion. This section will provide an in-depth discussion of the conventional instrumentation methods used in the SHPB.

3.4.1 The Electrical Resistance Strain Gage

The electrical resistance strain gage continues to be one of the most popular strain transducers due to its versatility, ruggedness and compactness. The strain gage consists of a strain-sensing element bonded to a backing material or carrier. The strain-sensing element typically consists of a length of a fine-gauge wire or filament configured in a foil grid such that any applied strain will elongate or compress the wire, changing its cross sectional area and thus, its resistance. Typical foil grid materials include Constantan and Karma (Nickel-Chromium) alloys [13]. The backing or carrier material serves as an electrical insulation barrier for the foil grid and allows for easy bonding to the structure under investigation. Typical carriers include polyamide and glass-fiber-reinforced epoxy-phenolic. Figure 3.10 depicts the construction of a typical analog strain gage.

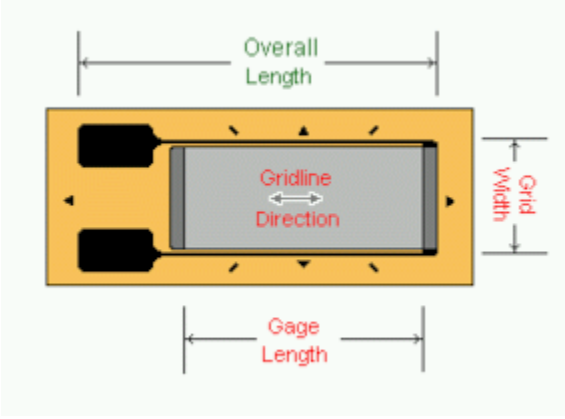

Figure 3.10 Typical Uniaxial Electrical Resistance Strain Gage [25]

The theory behind the electrical resistance strain gage is based upon the equation of the resistance of a conductor, shown below in Equation 3.42:

$$R = \rho \frac{L}{A} \tag{3.42}$$

In Equation 3.42, R is the resistance of conductor, ρ is the electrical resistivity of the conductor material, L is the length of the conductor and A is the cross sectional area of the conductor. Rewriting the denominator A in terms of a sectional dimension D and proportionality constant c, Equation 3.42 becomes

$$R = \rho \frac{L}{cD^2} \tag{3.43}$$

Differentiating Equation 3.43 and simplifying yields

$$dR = \frac{1}{CD^2}\left((Ld\rho + \rho dL) - 2\rho L \frac{dD}{D} \right) \tag{3.44}$$

Equation 3.44 is nothing more than the differential equation for the change in a conductor's electrical resistance with respect to time. Dividing Equation 3.44 by Equation 3.42 and simplifying yields

$$\frac{dR}{R} = \frac{dL}{L} - 2\frac{dD}{D} + \frac{d\rho}{\rho} \tag{3.45}$$

In Figure 3.10 above, the gridline direction defines the axial sensing direction while the lateral sensing direction is "planarly" perpendicular to the gridline direction. Equation 3.45 leads to individual relations for ε_A and ε_L, the axial and lateral strains, respectively:

$$\frac{dL}{L} = \varepsilon_A \qquad\qquad \frac{dD}{D} = \varepsilon_L \tag{3.46}$$

Another important effect mentioned earlier is defined by Poisson's ratio, which relates the change in diameter to the change in length of an element. Denotes as ν, Poisson's ratio is defined as

$$\nu = -\frac{dD/D}{dL/L} \tag{3.47}$$

Substituting 3.46 and 3.47 into Equation 3.45 yields the relation for gage factor, F:

$$F = \frac{dR/R}{dL/L} = \frac{dR/R}{\varepsilon_a} = 1 + 2\nu + \frac{d\rho/\rho}{dL/L} \tag{3.48}$$

The gage factor relates a materials mechanical properties to its electrical properties, particularly, its electrical resistivity. As Equation 3.48 holds true for all resistance type strain gages in the usual range of strain encountered, nearly all materials exhibit a constant gage factor [13]. A more convenient and common form of Equation 3.48 is given below in 3.49:

$$\varepsilon = \frac{1}{F}\frac{\Delta R}{R} \tag{3.49}$$

In Equation 3.49, ε refers to the strain in the gridline direction (axial) and is valid for small resistance changes only. Gage factor and initial resistance values are inherent properties of the strain gage foil grid material used in the construction of the gage. Typical gage factors vary from 2.0 to 5.0 and gage resistances are available in either 120 ohms or 350 ohms. A notable exception to the theory set forth above occurs with nickel, whose gage factor is actually a negative value (-12) [26]. Physically, this says that

increasing a nickel conductor's length or decreasing its cross sectional area actually decreases its resistance.

For most d.c. and low frequency strain applications, electrical resistance strain gages provide a rugged, economical and effective method of measurement. However, highly cyclic strains and thermal effects can cause significant errors in the output of strain gages [26]. Also, large strain gradients can result in an integrated or averaged strain value detected by the strain gage. Thus, many factors need to be considered before using strain gages.

The Measurements Group, Inc. [25, 26] defines a temperature-induced apparent strain as the nonzero output of a strain gage due to thermal effects. These thermal effects can be the result of variable ambient temperature conditions or thermal energy generated by the strain event. In either case, the resistivity of the strain gage is highly dependent on temperature. Thus, thermal errors can cause significant inaccuracies in strain gage output. According to The Measurements Group, Inc., "For low and medium strain applications, temperature-induced apparent strain can cause a thermal output greater than the magnitude of the strain to be measured [26]." For the SHPB, however, thermal consideration can be considered minimal since the laboratory temperature is controlled and thermal energy produced by the strain event does not affect the strain gages due to the remote mounting of the strain gages.

A more important consideration when utilizing strain gage technology is the ability of the gage to detect cyclic strains, particularly high frequency strain events. It is well documented that smaller gage length strain gages provide much better frequency response than longer gage length strain gages. However, for highly cyclic (high frequency) strain applications, high strain gradients lead to a phenomenon known as strain averaging or integration. Figure 3.11 below illustrates this phenomenon.

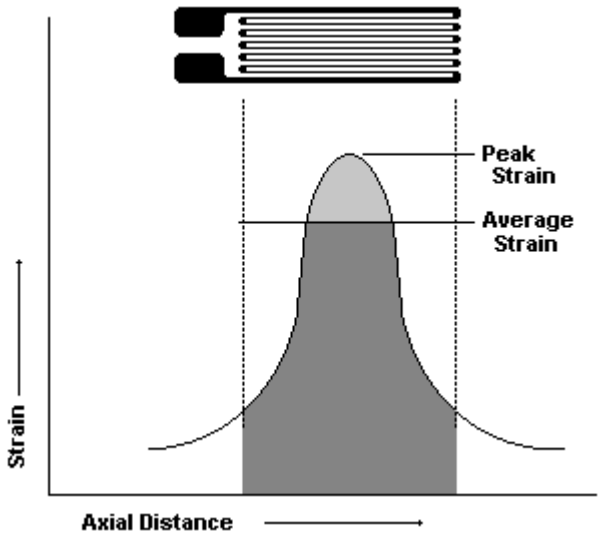

Figure 3.11 Peak Strain versus Average Strain [25]

The figure above shows that a longer gage length strain gage used to measure a highly concentrated or highly cyclic strain can average the signal over the length of the gage, causing an output that is significantly lower than the actual peak strain. Thus, smaller strain gradients result in a reported strain closer to the peak strain. Shorter strain gages, however, are not without problems either. Typically, shorter gage length strain gages exhibit degraded performance in terms of durability, thermal rejection, static load stability and signal-to-noise levels [26].

Kaiser [18] investigated more closely the phenomenon of a cyclic strain signal propagating across a strain gage and derived a relationship for the reported average strain as opposed to the peak strain. According to Vishay Measurements Group, "Since the average of any nonuniform strain distribution is always less than the maximum, a strain gage which is noticeably larger than the maximum strain region will indicate a strain magnitude which is too low [26]." In his derivation, Kaiser noted that the peak strain always occurs at the center of the gage length. Noting that the d.c. component strain is equal to the peak strain, he integrated a cosine wave over the length of the gage, as detailed below in Equation 3.50.

$$\varepsilon_{\text{Re ported}} = \frac{C_o}{L_G} \int_{-\frac{L_G}{2C_o}}^{\frac{L_G}{2C_o}} \cos(2\pi \cdot f \cdot t)dt \qquad \textbf{(3.50)}$$

In Equation 3.50, $C_0 = \sqrt{\frac{E}{\rho}}$ (the infinite wavelength wave velocity), L_G is the gage length of the strain gage and f is the frequency of the cyclic strain signal. Evaluating this integral yields

$$\varepsilon_{\text{Re ported}} = \frac{C_o \sin\left(\frac{\pi \cdot L_G \cdot f}{C_o}\right)}{\pi \cdot L_G \cdot f} \qquad \textbf{(3.51)}$$

Thus, peak strain and average strain are equal only for dc (non-cyclic) strain events. Figure 3.12 below is a graphical representation of Equation 3.51 for various length strain gages.

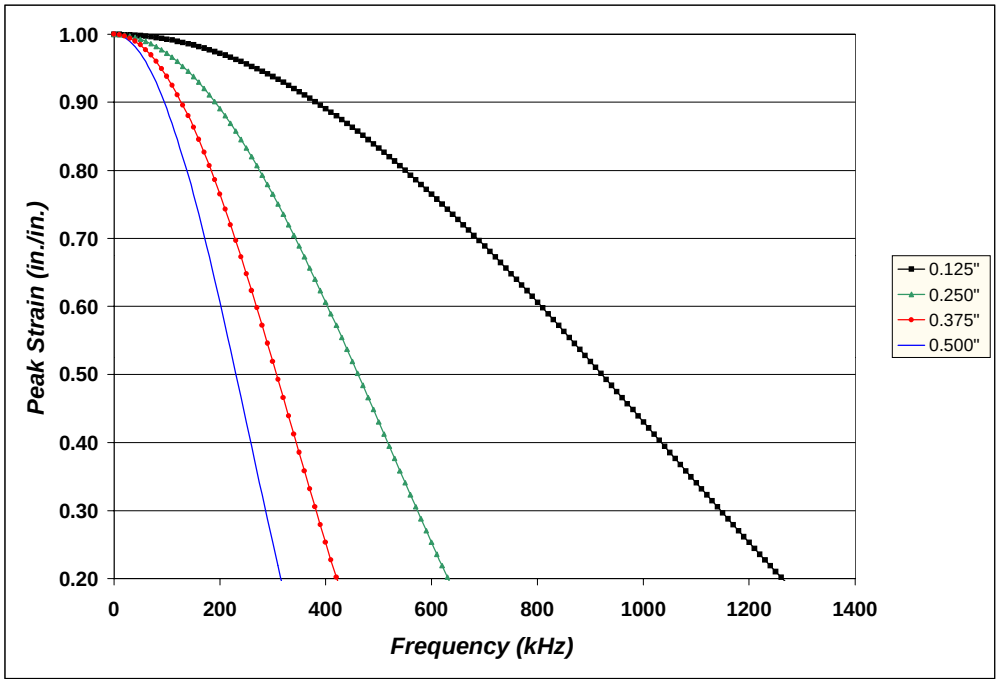

Figure 3.12 Reported Strain versus Frequency for Various Gage Lengths [18]

Examining Figure 3.12, a number of observations can be made. First, smaller gage length strain gages offer better frequency response for highly cyclic strains than longer gage length gages. Thus, smaller gages report average strain values closer to the actual peak strain values. Also, except at frequencies approaching dc, the reported strain is always lower than the true strain. This, again, is due to the averaging effect described above. In the case of the SHPB, Equation 3.10 can be used to determine the frequency at which signal attenuation becomes significant. Using 0.375" gage length strain gages (as used on the SHPB) and the mechanical properties of the maraging steel pressure bars, the cyclic strain frequency at which signal attenuation begins to be of importance is approximately 150 kHz [18].

Another undesirable characteristic of the electrical resistance strain gage is its inherent windowing effect. This windowing effect is due to the cyclic strain signal propagating the length of the strain gage. In the time domain, this is equivalent to the phenomenon known as convolution. In this case, the strain gage acts as a rectangular window propagating the entire wavelength the cyclic strain signal. Thus, the gage length of the strain gage is convolved with the strain signal, producing a windowed output. Kaiser [18] presents a concise derivation of the convolution solution required to compute the windowing effect of the strain gage. In short, the rectangular window and strain signal are represented as square pulses of magnitudes A and B, respectively. The duration of the strain signal and window pulses is denoted as $G_L/2$ and $P_L/2$, respectively. Assuming both pulses have an equivalent period T, the Fourier Transforms of both pulses can be computed such that the analysis shifts from the time domain to the frequency domain. This is done below in Equations 3.52 and 3.53:

$$Pulse(\omega_o) = \frac{B \cdot P_L}{T} \cdot SINC\left(\frac{n \cdot \omega_o \cdot P_L}{2}\right) \quad \textbf{(3.52)}$$

$$Window(\omega_o) = \frac{A \cdot G_L}{T} \cdot SINC\left(\frac{n \cdot \omega_o \cdot G_L}{2}\right) \quad \textbf{(3.53)}$$

Equations 3.60 and 3.61 represent the frequency domain representations of the two pulses. Once in the frequency domain, the two signals can be multiplied together as convolution in time is equivalent to multiplication in frequency. Thus

$$\varepsilon_{out}(\omega_0) = Window(\omega_0) * Pulse(\omega_0) \tag{3.54}$$

Once this multiplication is done, the inverse Fourier Transform can be computed to return the solution to the time domain. This solution becomes

$$\varepsilon_{OUT}(t) = \sum_{-\infty}^{\infty} \frac{4 \cdot A \cdot B \cdot SIN\left(\frac{G_L \cdot n \cdot \omega_o}{2}\right) \cdot SIN\left(\frac{P_L \cdot n \cdot \omega_o}{2}\right)}{T^2 \cdot n^2 \cdot \omega_o^2} \exp(-i \cdot n \cdot \omega_o \cdot t) \tag{3.55}$$

Basically, Equation 3.55 presents a relationship between the gage length and pulse length for strain gages subjected to cyclic strains. In order to get a clearer picture of the windowing effect of the strain gage, Equation 3.55 is plotted below in Figure 3.13 for various pulse length-to-gage length ratios (PL/GL).

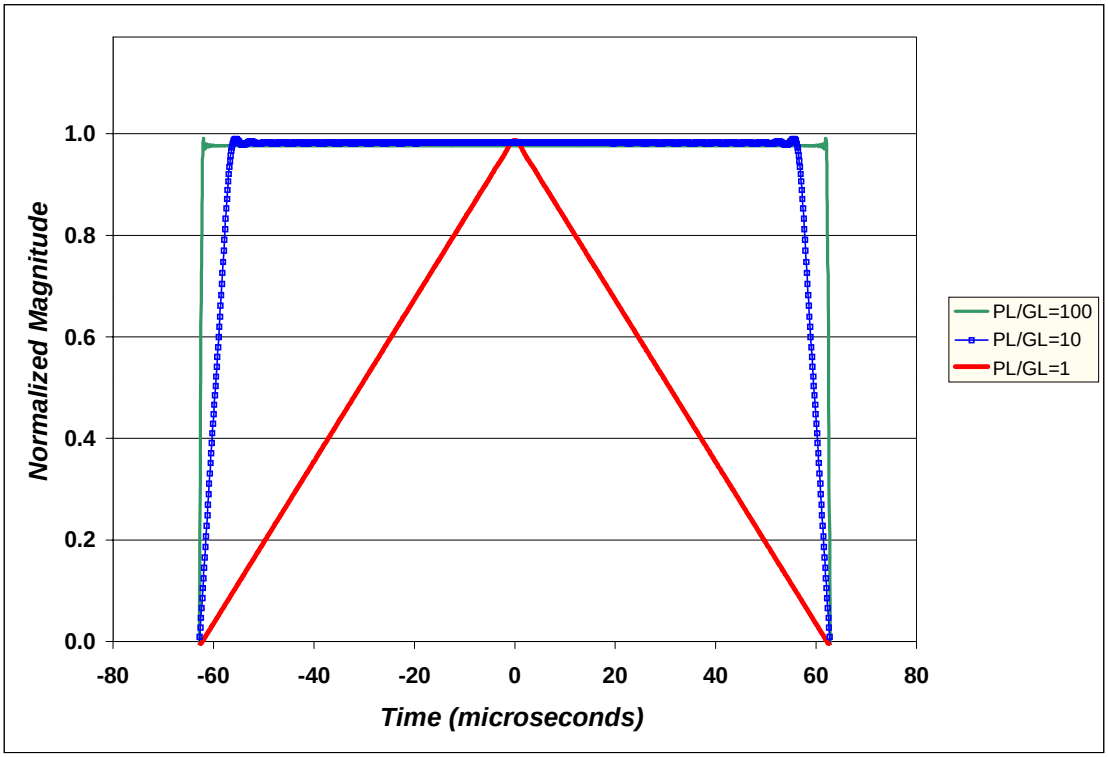

Figure 3.13 Convolved (Windowed) Output of Resistance Strain Gages [18]

Examining Figure 3.13 and recalling that the strain pulse was represented as a square wave, it is clear that gage length selection is an important criterion when instrumenting a structure subjected to cyclic strains. For PL/GL = 100 and PL/GL = 10, the strain signal shows minimal distortion, exhibiting a finite rise time and slightly reduced peak magnitude. For PL/GL = 1 however, the convolved signal resembles a triangular wave. Thus, to minimize the effects of windowing on the strain signal, it is necessary to choose strain gages with gage lengths much shorter than the wavelength of the strain pulse.

3.4.2 The Resistance Bridge

As detailed earlier in this thesis, the conventional method of capturing the strain histories from the SHPB consists of strain gages connected in a resistance bridge configuration. The most widely used resistance bridge is the Wheatstone bridge, developed by S.H. Christie in 1833 [13]. The Wheatstone bridge is ideal for making measurements with passive transducers such as thermistors, resistance thermometers and strain gages. A

derivative of the Wheatstone bridge is a configuration known as a strain bridge. The strain bridge simply consists of a combination of four resistors and strain gages configured as two parallel circuits. Figure 3.14 shows one particular strain bridge configuration.

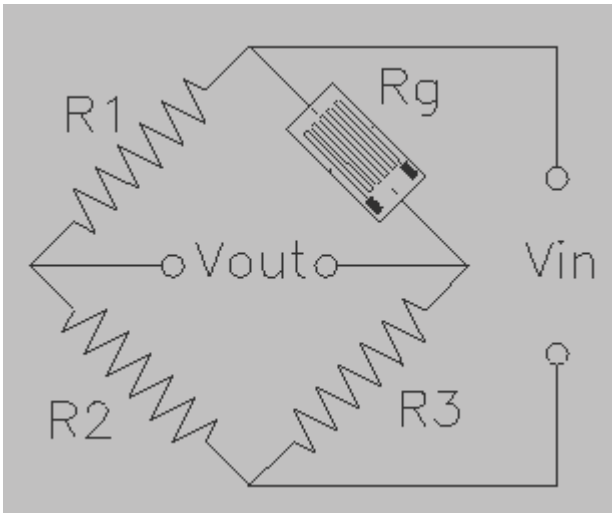

Figure 3.14 Strain Gage in Quarter-Bridge Configuration [25]

The above figure shows the quarter bridge configuration (strain gage accounts for 1 of 4 resistances) in which a single strain gage is placed in the circuit with three resistors to complete the bridge. The three resistor values, R1, R2 and R3, should be closely matched to the resistance of the strain gage, Rg, so that the bridge will be "balanced" for the zero input condition. An alternative method of selecting the resistor values involves the ratio between any two adjacent resistors. Thus, a balanced bridge could also be achieved with the following resistor ratios:

$$\frac{R1}{R2} = \frac{Rg}{R4} \qquad \text{or} \qquad \frac{R1}{Rg} = \frac{R2}{R4}$$

Typically, however, an external balance circuit is incorporated into the bridge so that introducing an input voltage in one arm of the bridge can compensate for small resistor value variations. This input voltage effectively offsets the imbalance caused by the

mismatched resistances of the resistor(s) and the strain gage(s). An excitation voltage, Vin, is required to power the bridge. Changes in any one of the resistances in the bridge will cause a bridge imbalance and ultimately, a voltage output, Vout. Thus, with the three fixed resistors set, the change in resistance of the strain gage due to an arbitrary strain event results in a voltage signal. It is this voltage signal that contains the stress and strain data from the split Hopkinson Bar experiment.

3.4.3 The Instrumentation Amplifier

In many instances, strain signals recorded by strain gages are of a very small magnitude, typically only a few millivolts. Attempting to process a signal of only a few millivolts can result in a very low signal to noise ratio since electronic noise within the digital storage scope is sure to contribute to the signal. Thus, instrumentation amplifiers are generally used to help alleviate the problems associated with small-magnitude differential signals. A typical instrumentation amplifier design is shown below in Figure 3.15.

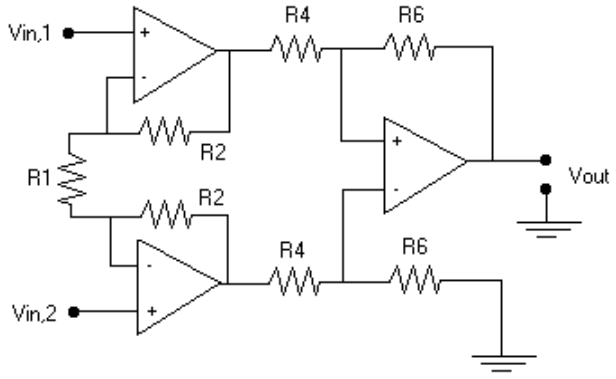

Figure 3.15 Typical Instrumentation Amplifier [11]

The instrumentation amplifier shown above utilizes three operational amplifiers (op-amps) to provide two stages of amplification (more commonly referred to as gain). In a typical adjustable gain operational amplifier, the gain is set by the selection of R1, which may be either a fixed resistor or a potentiometer. As $R1 \rightarrow 0$ or $R1 \rightarrow \infty$, the first stage of the instrumentation amplifier tends to behave as a voltage follower, meaning that the first stage gain is 1. The second stage gain is set by the selection of the resistors R4 and R6.

With the resistor pairs selected as shown above, the gain of the instrumentation amplifier can be calculated as follows:

$$Gain = \left(1 + \frac{2R2}{R1}\right)\left(\frac{R6}{R4}\right) \tag{3.56}$$

According to Equation 3.56, a wide range of gain values is available since resistor values range from a few ohms to hundreds of mega ohms. However, resistor values are normally selected in the range from 1000 ohms to 100,000 ohms. Resistor values too small result in excessive current draw and resistor values too large allow can cause noise issues. In general, the output of the instrumentation amplifier is limited by the voltage supplied to the op-amps. Without the inclusion of specialized transistor circuitry, the output of the instrumentation amplifier is limited to the voltage supplied to each individual op-amp, assuming "rail-to-rail" op-amps are used. This voltage is typically 5 VDC to 30 VDC. Op-amps not classified as "rail-to-rail" are limited to an output voltage typically 2 VDC less than the supply voltage. A typical op-amp is shown below in Figure 3.16.

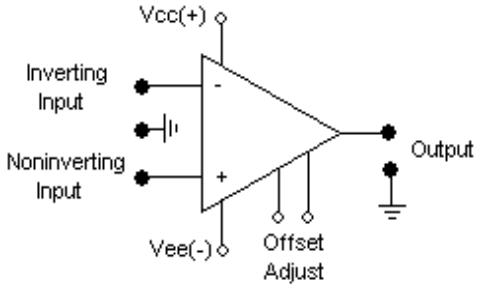

Figure 3.16 Typical Op-Amp Configuration

In the figure above, Vcc is the positive supply voltage and Vee is the negative supply voltage. Typically, -Vcc = Vee. The offset adjust pins allow the user to make provisions for zeroing the amplifier such that zero input results in zero output. This is an important feature of the op-amp since noise in the form of bias currents and ground loops can result in a signal output for the zero input condition. Zeroing an amplifier is best achieved by shorting the two inputs together before adjusting the offset.

In general, however, compared to a single op-amp design, the instrumentation amplifier provides better noise and common mode rejection capabilities by subjecting the input signals to very high input impedances. The input impedance is raised substantially by the addition of the R2 resistors in the negative feedback loop of the first stage op-amps. Neglecting the R1 resistor, each first stage op-amp acts as a voltage follower, thereby increasing the + and – input impedances substantially. Also, summing constraints at the two first stage op-amps result in a source current draw of zero. This results in nearly infinite input impedance [13]. The common mode rejection capability is improved by the addition of the R1 resistor. The addition of this resistor subjects the differential signal to a first stage gain while the common mode signal experiences no such amplification. Thus, the common mode rejection ratio (CMRR) is greatly increased. Typically, the input impedance for an instrumentation amplifier is in the gigaohms range and the CMRR is 100 decibels (dB) or more [13]. Also, as opposed to the single op-amp design, resistor values are not as critical in the instrumentation amplifier since the high input impedance yields little current through the amplifier. Thus, the instrumentation amplifier is well suited for use with strain bridges and other differential voltage signals.

Chapter 4. Design Methodology

4.1 Introduction

With the research and background information presented in Chapters 2 and 3 of this thesis, the actual design phase began with the goal to develop a simple yet effective method of measuring the dynamic change in specimen diameter of the SHPB specimen using optical methods. The simplest optical measurement system would consist of a low power laser and high-speed photodetector. However, some combination of additional optical devices including collimating lenses, filtering lenses, beam splitters and reflective reference surfaces are typically needed in such systems. For this research, an initial design was selected such that the only required tools would be a semiconductor laser diode, silicon photodetector, collimating lens and related circuitry. With this equipment, the optical measurement system would be constructed and tested in order to determine if the installation of any other optical devices would be necessary. This chapter will present the design methodology followed in preparing this optical system of strain measurement.

4.2 Naval Surface Warfare Center Dahlgren Division Split Hopkinson Pressure Bar

As detailed previously, the split Hopkinson pressure bar has become and still remains one of the preferred methods of testing materials at medium rates of strain. It is a simple yet effective means of subjecting small test specimens to stresses and strains typically encountered during shock and impact events. Figure 4.1 below is a schematic of the compressive SHPB found at the Naval Surface Warfare Center at Dahlgren:

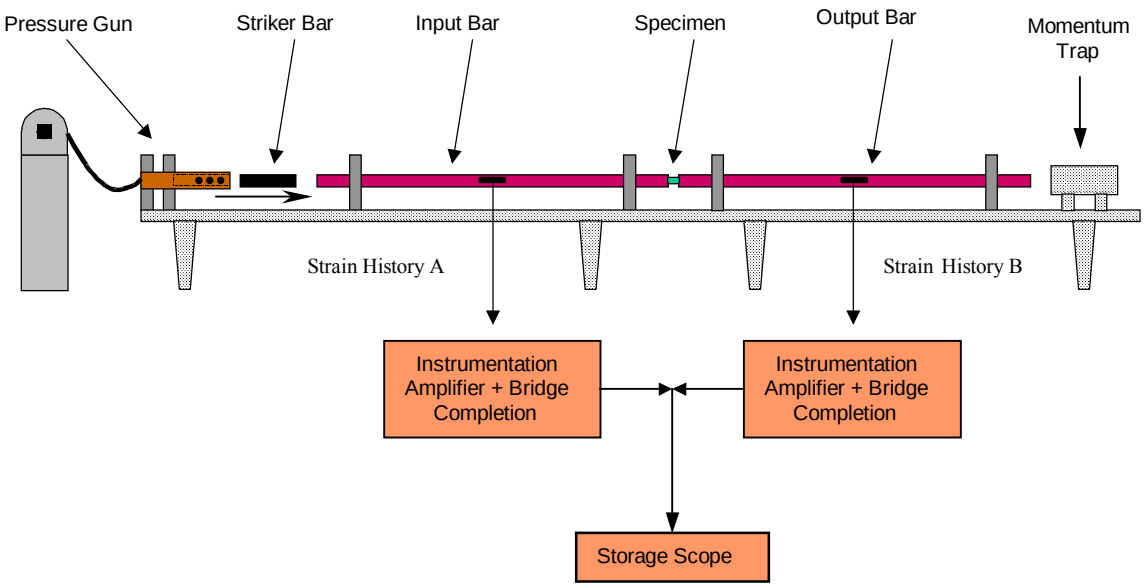

Figure 4.1 NSWCDD's Compressive Split Hopkinson Pressure Bar

To briefly review the split Hopkinson pressure bar experiment, after the striker bar impacts the input bar, a compressive stress wave travels the length of the input bar to the input bar – test specimen interface. At this interface, a portion of the compressive wave transmits through the specimen while the remainder of the wave reflects back into the input bar. The portion of the wave that transmits through the specimen exits the specimen at the output bar-specimen interface and continues through the output bar. The propagation of the stress waves generates strain histories at strain gages A and B. The strain history recorded by gage A is used to compute the specimen strain and strain rate while the strain signal captured by gage B can be used to determine specimen stress levels. These strain histories are typically amplified and recorded with instrumentation amplifiers and multi-channel digital storage oscilloscopes. In the case of the NSWCDD, this data is then post-processed via a Matlab® program designed and implemented by Kaiser [18]. This algorithm also calculates necessary pretest parameters for proper configuration of the SHPB apparatus. These parameters include gas gun breech pressure, momentum trap gap distance and pressure bar stress levels.

4.2.1 NSWCDD SHPB Mechanical Properties

As stated earlier in Chapter 3, the simplified analysis of the SHPB presented in this thesis is only valid if, among other things, the specimen stress is held below the elastic limit of the input (incident) pressure bar. Thus, the yield strength of the input bar plays a critical role in the dynamics of the experiment. The mechanical properties of the pressure bars used at NSWCDD are listed below in Table 4.1.

Table 4.1 Mechanical Properties of NSWCDD's Pressure Bars

Type: Vascomax C-350 Centerless Ground MIL-S-46850D	
Mechanical Property	**Value**
Tensile Strength	370 ksi
Yield Strength	350 ksi
Elongation	6.0%
Reduction of Area	34.0%
Charpy Impact	6.0 ft/lb

In Table 4.1, the tensile strength is analogous to the elastic limit. Thus, to ensure that the stress in the pressure bars does not approach the plastic regime, the peak stress must be held well below 370 ksi. The yield strength of the material is taken to be the 2% yield point such that application of this stress will cause plastic deformation (elongation) of 2%. The elongation and reduction of area values given above apply to a tensile test of the pressure bars. Similar to Poison's Ratio, a 6% bar elongation will result in a cross sectional reduction of area of 34%. Charpy impact is a method of toughness and resilience testing and has little bearing on the analysis done in this thesis.

The SHPB apparatus at NSWCDD was manufactured by San Diego State University. The pressure bars are made from high strength maraging steel. Several pressure bar lengths and diameters are available, each being best suited for the particular material being tested. The pressure bars are limited to thrust (longitudinal) motion only by the

addition of sleeve bearings to support the pressure bars. These sleeve bearings are supported by split bearing blocks that aid in the alignment of the bearings with the pressure bars. A series of 10 bearing assemblies are utilized in the SHPB in use at Dahlgren. These bearing assemblies are precisely positioned to ensure that the striker bars impact the specimen with a thrust force component only. Any angular or out-of-plane forces could cause the assumptions set forth above (homogeneous, uniaxial deformation) to be invalid.

The SHPB at Dahlgren has been used to conduct dozens of experiments on materials ranging from aluminum and steel to Lexan and various plastics. The results of these experiments have been compared to tabulated data presented by other researchers. Thus, reliable, baseline data exists for comparative purposes. Because of this, it can be surmised that the SHPB at Dahlgren is performing as specified.

4.2.2 NSWCDD SHPB Instrumentation

As detailed in Chapter 3, the conventional method of gathering strain data consists of strain gages connected in a full, half or quarter bridge configuration. These strain gages are typically attached at the longitudinal centers of the input and output pressure bars. Mounting the strain gages away from the specimen protects the gages from the high shock forces associated with the impact event while mounting them at the longitudinal center of the bars aids in the separation of the incident and reflected pulses in the input bar. The strain gages attached to the pressure bars at Dahlgren are 3/8" gage length, 1000-Ω nominal resistance strain gages produced by The Vishay Measurements Group. As detailed in the previous chapter, strain gages shorter than 3/8" tend to exhibit degraded performance in terms of maximum allowable elongation, stability under static strain and endurance when subjected to cyclic strains [12]. The 1000 Ω resistance of the strain gage coupled with the ½-brdge configuration provides additional thermal stability, cancellation of leadwire effects and better signal-to-noise values than lower resistance gages [13]. The instrumentation amplifiers and the bridge balance circuits were designed and built at Virginia Tech. The data acquisition system consists of a Tektronix TDS-

744A digital storage oscilloscope capable of capturing signals at speeds of up to 500 MHz. The instrumentation method currently in use at Dahlgren will be discussed in greater detail in subsequent sections.

4.3 Optical Measurement System

The primary goal of this research was to replace the existing electrical resistance strain gage measurement system with a faster, more robust method of strain measurement. The idea to apply laser technology to NSWCDD's SHPB was conceived by Dr. Andy Barker and Dr. Al Wicks. It was conceptualized that the diameter of the test specimen could be measured by a sharply defined line of laser light. The portion of the laser not obscured by the test specimen could be collected by a high-speed photodetector as well as other yet-to-be determined optics. The light absorbed by the photodetector would then be converted to a voltage output. Using a suitable calibration curve, this voltage output could then be converted to a diameter measurement and compared with the original diameter of the specimen. Training the laser on the specimen during the dynamic test would provide "real-time" strain information throughout the duration of the experiment. It was surmised that this direct, non-contact approach of optical strain measurement would effectively filter out several of the sources of uncertainty associated with SHPB testing including pressure bar dispersion and strain gage electrical and mechanical errors.

To keep the system as simple as possible, the design was originally laid out using only the most basic components of an optical measurement system: light source, collimating lens, photodetector and related circuitry. These components would be arranged to measure the diameter of the test specimen as shown below in Figure 4.2:

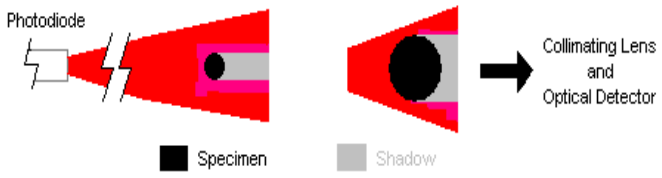

Figure 4.2 Proposed Optical Strain Measurement System

As Figure 4.2 shows, the original design consisted of only a laser diode, collimating lens and photodetector. The laser can be focused such that a sharp line of light will be generated across the diameter of the cylindrical SHPB test specimen. The portion of light not occluded by the specimen will be collected by a high-speed optical detector after being collimated by a suitable lens. The optical detector would convert the light energy into an electrical energy. This electrical energy would be measured as a voltage output and recorded before, during and after the high strain rate event. The dynamic change in the diameter of the specimen can then be related to the specimen true strain, shown below in Equation 4.1:

$$\varepsilon_{True} = \ln\left(\frac{l}{l_0}\right) \tag{4.1}$$

In Equation 4.1, ε_{True} is the true specimen strain, l is the instantaneous or final length of the specimen and l_0 is the initial length of the specimen. The development of the relationship between specimen radial changes and true strain will be presented at the end of this chapter once the reader is more familiar with the optical method of measurement. With the specimen strain in hand, the corresponding strain versus time signal can be differentiated with respect to time to compute the strain rate. Specimen stress, however, must be computed using the output bar strain gage as no acceptable means of calculating the stress from the photodetector output has been developed. Again, development of the equations governing the optical strain measurement system will be presented later in this chapter.

4.3.1 Optical Measurement System Specifications

In selecting a source of laser light for this research, many factors were considered. With the recent popularity of lasers as tools of engineering, a wide variety of lasers now exist for commercial and industrial applications. After carefully reviewing the dynamics of the test apparatus as well as the goals of this research, the following list of parameters was generated:

1. Select a Class II laser capable of generating a visible line of light.
2. Select a photodetector capable of speeds up to 25 MHz.
3. Provide additional optics and circuits to produce a linear output.
4. Select an appropriate means of supporting the entire assembly.

As detailed briefly in Chapter 1, laser protocol and safety were the major areas of concern in selecting a suitable source of laser light. In making the system as safe as possible, a laser capable of generating a visible beam was specified so that accidental or unknown exposures would be less likely. As previously shown, the visible region of light covers an approximate range of frequencies from 600,000 terahertz (THz) to 1,000,000 THz and wavelengths from 400 nm to 1000 nm. A Class II laser was specified because these lasers generate the least amount of power and allow for longer and more direct exposures without danger. To review Class II laser safety,

> **Class II –** "Caution" low power visible lasers or laser systems less than 1 mW which, because of the normal human aversion response (eye blinking, eye movements, etc.) do not normally present a hazard, but may present a potential hazard if viewed directly for extended periods of time.

As opposed to Class III and Class IV lasers, Class II lasers, when used properly, present very little hazards to the user. For this reason, a visible light Class II laser was specified.

4.3.2 Optical Measurement System Component Selection

The Lasiris SNF-501L-670-5 semiconductor laser diode was ultimately chosen for this project due to its compact size, rugged design and availability. The SNF-501L is a 670 nm wavelength line-generating semiconductor laser diode (5º divergence) capable of producing 0.980 mW of power at 0.58 milliamps (mA) while requiring only ±6 VDC power. At 670 nm, the light generated by the laser will appear red in color. It should be noted the beam itself is not visible to the naked eye without the use of smoke or similar media however, the beam will appear visible on any solid medium at which it is pointed. Figure 4.6 below shows the SNF-501L semiconductor laser diode and associated optics.

Figure 4.3 Lasiris SNF-501L Semiconductor Laser Diode and Accessories [40]

In order to provide a stable source of power for the laser, a regulated 6-volt AC-to-DC adapter was modified for use with the SNF-501L. Subsequent tests showed that this power supply produced an output voltage of 6.02 ± 0.02 VDC at 300 mA with no detectable drift or ripple. Corresponding laser output power measurements taken with a Coherent Lasermate Model 0217-050-00 (Serial Number LS46) laser power meter revealed that the SNF-501L, rated at 0.9 mW of output power, is generating 0.88 mW of peak power. The Lasermate was last calibrated January 13, 1998. Additional information regarding the Lasiris SNF-501L semiconductor laser can be found in the supplement to this thesis.

The bandwidth and resolution of the optical measuring system will be set by the selection of the optical detector, more commonly known as a photodetector. The photodetector contains an active semiconductor material such as silicon that converts optical energy into electrical energy. This electrical energy is typically in the form of a voltage. The bandwidth of the photodetector determines how quickly it can perform this energy conversion. Specified in MHz, typical photodetectors are capable of speeds up to 1 gigahertz (GHz). For this research, however, it was determined that a bandwidth of 25 MHz would still provide strain resolution approaching 1 to 2 microstrain (μstrain).

For this application, the Devar 509-0015 high-speed silicon photodiode optical detector was chosen. According to the specification sheet for the 509-0015, the 509-0015 has a maximum bandwidth (-3 dB method) of 25 MHz and a rise time (10%-90%) of 14×10^{-9} s. The 509-0015 detector, in its "as-built" configuration, is shown below in Figure 4.4:

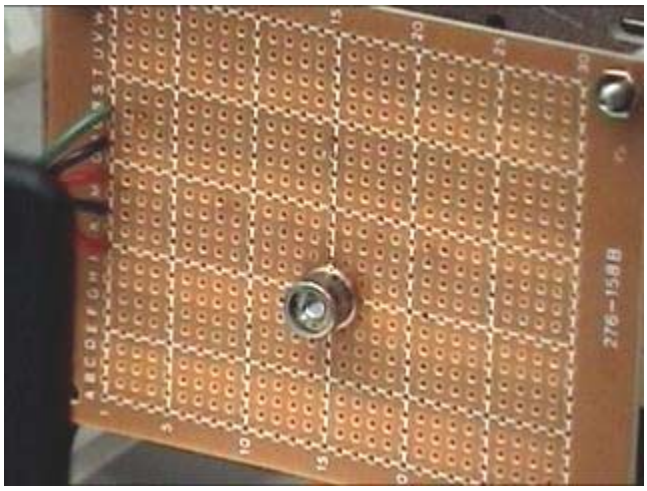

Figure 4.4 Devar 509-0015 Optical Detector

This particular detector utilizes a 5-mm2 silicon active area to perform the optical-to-electrical energy conversion. In order to perform this conversion, a negative bias voltage of –15 to –50 volts DC is required to lower the junction capacitance between the silicon photodiode and the current-mode op-amp used to perform the light-to-voltage conversion. In addition, the 509-0015 requires ± 6 VDC (nominal) for operation. This particular photodetector is constructed in a TO-5 package and lists the pin-out diagram as shown below in Figure 4.5:

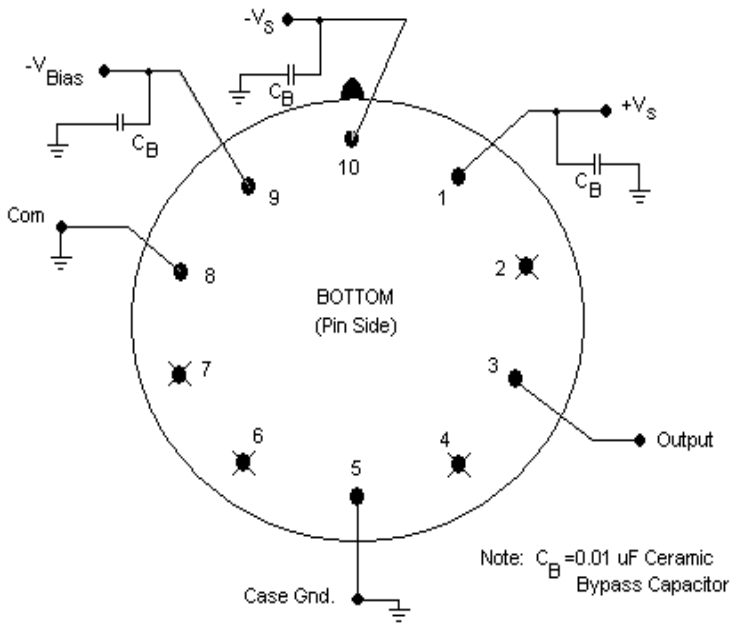

Figure 4.5 Devar 509-0015 Optical Detector Pin Connection Diagram

As shown in Figure 4.5, the TO-5 package consists of 10 connection pins. Note that the pins marked with an "X" are not used. Each $+V_S$, $-V_S$ and V_{Bias} pins were grounded via a 0.01 μF ceramic bypass capacitor in order to filter out any transient AC voltages that might be present in the power supplies. Specifications provided by Devar indicate a nominal supply voltage of ±6 VDC with a bias voltage of –15 to -45 VDC. Further research with the optical detector yielded a best operating bias voltage of approximately –25 VDC. This bias voltage provides adequate bandwidth and slew rate while maintaining acceptable noise rejection capabilities. In order to provide the optical detector with the proper voltages, a photodetector supply circuit was designed and built. This circuit is shown below in Figure 4.6.

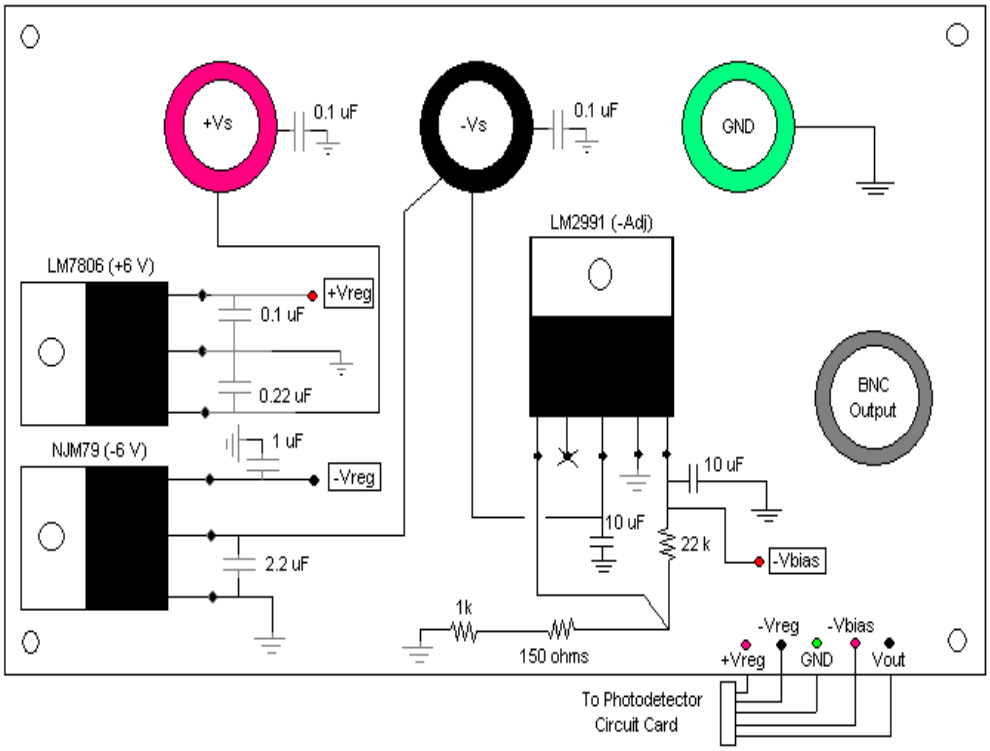

Figure 4.6 Photodetector Circuit Card and Components (NSWCDD SHPB)

In the circuit shown above, the +6 VDC and –6 VDC voltages are supplied via the National Semiconductor LM7806 and New Japan Radio NJM79 voltage regulators. Likewise, the –24.5 VDC bias voltage is supplied by the National Semiconductor LM2991 adjustable negative voltage regulator. The LM2991 output voltage is set by the relation shown below in Equation 4.2:

$$V_{out} = -1.281\left(\frac{R_1}{R_2}\right) \qquad \textbf{(4.2)}$$

With R_1 = 22 kΩ and R_2 = (1000 + 150) Ω, an output voltage of –24.5 VDC is realized. This is dependent on a nominal input voltage of V_S = ± 25 VDC at the circuit card input banana terminals. Bypass capacitors are located throughout the circuit to pass any stray AC signals to ground. These steps should ensure clean, stable voltage to the optical detector. Specification sheets for these integrated circuit components will be included in

the supplement to be included with this thesis. Shown below in Figure 4.7 is the actual photodetector circuit built for this research.

Figure 4.7 NSWCDD Photodetector Circuit

In conjunction with the 25 MHz photodetector, a collimating lens was selected such that the portion of light that passes the SHPB test specimen can be focused to a point for collection by the silicon photodetector. The lens chosen for this application is the Newport PAC552-25.4 Achromatic Doublet Lens. This 1.00" diameter lens consists of an achromatic doublet that provides superior laser beam manipulation characteristics including the ability to focus light beams to smaller spot sizes. The construction of the achromatic doublet consists of a positive low-index crown glass lens cemented to a negative high-index glass lens chosen such that the two lenses act to cancel out any chromatic aberrations within the light [24]. The lens is tailored for use at the specific frequency of the selected laser (670 nm) and has a constant focal length (effective focal length) of 100 mm.

In addition to the collimating lens, a passband filtering lens was selected such that only 670 nm wavelength light would pass through the lens assembly. The filtering lens chosen for this application is the Newport TL670-24.4 lens. It is rated at 670 nm with a

50% transmission passband of 662 nm – 678 nm. This passband effectively filters out the majority of the ambient light present in the laboratory. Thus, fluctuations in ambient lighting conditions will have negligible effect on the experimental results.

In order to support the components of the optical strain measurement system, several other pieces of equipment were required. An optical carrier rail was specified such that both longitudinal and lateral adjustments could be made during the experiment. The rail chosen was Newport's X95-1 aluminum structural rail. The X-95 is 1 meter in length and boasts a bending tolerance of 0.8 mm/m and a twisting tolerance of 0.75 mm/m. These tight tolerances minimize the possibility of component misalignment due to subtle bends or twists in the rail system. In addition, the X-95 helps alleviate the concern of positioning the laser such that the light is properly aligned with the specimen, lens and photodetector. The X-95 also permits the use of adjustable carriers on which the laser diode, collimating lens and photodetector can be mounted.

In order to properly position and align the PAC552-25.5 collimating lens, the Newport 9834-25.4 lens holder was specified. This lens holder permits the insertion of any 25.4 mm diameter lens into its carrying cavity. It also has a series of tapped holes for the attachment of additional components or to include it as a part of a greater assembly. This same holder was also used to carry the TL670-25.4 passband filtering lens. These lenses were mounted in series with one another with the collimating lens closer to the laser diode. The use of pre-tapped holes in both the lens holders and rail carriers helped ensure that the lenses were properly aligned with one another and with the longitudinal axis of the laser diode.

With all of the components and circuitry designed and built, the optical measurement system is shown below in Figure 4.8.

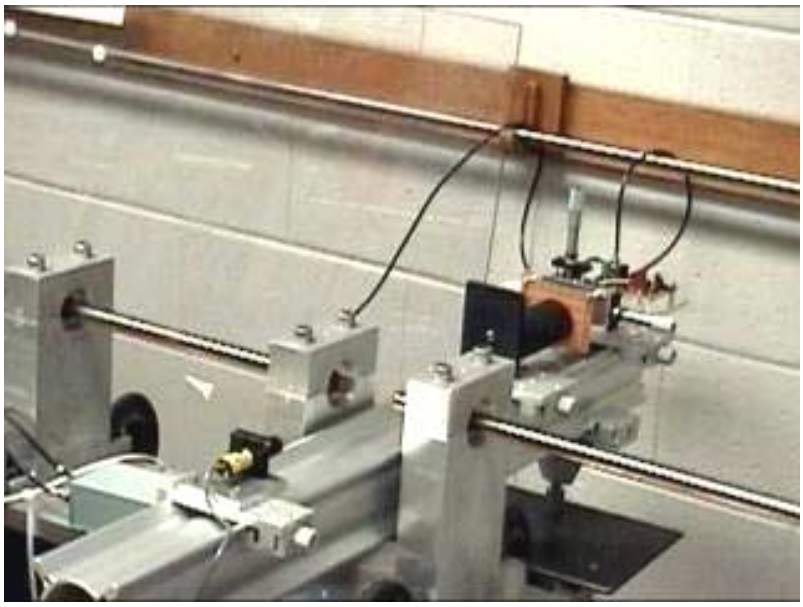

Figure 4.8 NSWCDD Optical Strain Measurement System

In the image above, note the laser diode at the bottom left corner and the detector circuit in the upper right corner. The input and output pressure bars and three of the bearing blocks are also visible. In addition, a black paper tube was arranged between the collimating lens and the optical detector such that ambient light would not contribute to the output of the detector.

4.4 NSWCDD SHPB Instrumentation Verification

Although the purpose of this research is to implement an optical method of strain measurement to negate known sources of the errors associated with strain gage technology, the original strain gage instrumentation system is needed to generate a set of baseline data against which the optically measured data can be compared. In addition, it was shown in Chapter 3 that the output bar strain gage would be needed to process specimen stress information. Thus, it was decided that the existing instrumentation would be thoroughly tested and checked to verify proper operation. Modifications and/or repairs could then be made as needed. Again, the strain gage instrumentation consists of a series of strain gages incorporated into a bridge network and an instrumentation amplifier to boost the signal strength to acceptable levels.

To briefly review, the strain bridge, modeled after the popular Wheatstone bridge, simply consists of a combination of 4 resistors and strain gages configured as two parallel circuits, similar to a pair of voltage dividers. An excitation voltage ±Vs is supplied to the bridge such that the strain gage(s) respond to the strain event with a corresponding voltage output V_{out}. Typically, a balance circuit is incorporated into the bridge such that small variations in resistor values can be nullified by introducing an input voltage across the bridge, providing an effective means of zeroing the output for the zero input condition. In the case of the bridge completion networks built for the NSWCDD SHPB project, a balance circuit referred to as a differential shunt balance was used. This balance circuit as well as the half-bridge strain gage configuration used at NSWCDD is shown below in Figure 4.9.

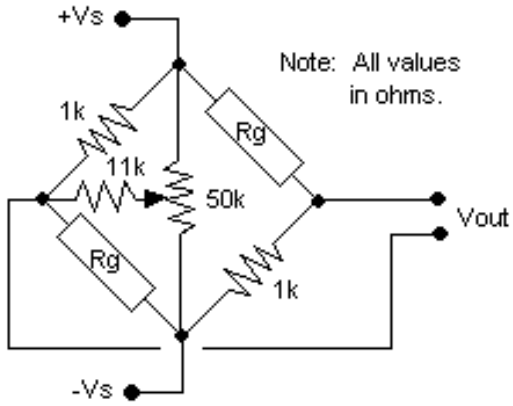

Figure 4.9 NSWCDD Strain Bridge with Differential Shunt Balance

Figure 4.9 shows the half-bridge configuration (2 strain gages + 2 fixed resistors) used with the SHPB at Dahlgren. The half-bridge configuration is more desirable than the quarter bridge configuration because it provides additional stability as the thermal and electrical sensitivities of the two strain gages tend to negate one another [26]. The differential shunt balance used in these circuits is an especially effective method of balancing resistance bridges subjected to small bridge imbalance conditions [13]. To

achieve a balanced bridge (zero output for zero input), the bridge excitation voltage Vs is introduced to the circuit through the 50 kΩ potentiometer and 11 kΩ end resistor. The potentiometer can be adjusted to change the level of voltage introduced to the circuit until this voltage effectively offsets the imbalance caused by the mismatched resistances of the R1 and R2 and the two strain gages Rg. With this combination of resistors, the total offset voltage V_{Offset} available can be calculated as follows:

$$V_{Offset} = \left(\frac{Vs}{11k\Omega + R_L} \right) * R_L \qquad \textbf{(4.3)}$$

Again, Vs is the bridge excitation voltage while R_L is the resistance of the load being driven by the potential difference. With a balanced bridge, changes in any one of the resistances in the bridge will cause a corresponding imbalance and consequently, a voltage output Vout. Thus, with the two fixed resistor values set, the change in resistance of either of the strain gages due to an arbitrary strain event results in an unbalanced bridge and hence, an output voltage signal.

Since the strains generated in SHPB testing are relatively small, instrumentation amplifiers are needed to boost the output signal Vout. As detailed previously in Chapter 3, well-designed instrumentation-quality differential amplifiers provide an effective means for achieving this boost in signal strength. Designed and built separately from the bridge completion networks, two instrumentation amplifiers were constructed in-house at Virginia Tech by the previous researcher. Figure 4.10 below schematically represents the evolution of the strain signal generated by the SHPB:

Figure 4.10 Evolution of SHPB Strain Signal

In order to verify the proper operation of the strain gage instrumentation used with NSWCDD's SHPB, the instrumentation amplifiers HB-1 and HB-2 and the bridge completion networks WB-1 and WB-2 were subjected to complete teardown and inspection. This was done to ensure that the baseline data against which the optically measured data was to be compared would be of the highest possible accuracy and precision.

In order to check and verify the operation of the SHPB amplifiers HB-1 and HB-2, both amplifiers were returned to Virginia Tech for thorough testing. From a complete teardown of the amplifiers, a wiring schematic was generated and examined. Figure 4.11 shows the original circuit design used in the construction of the amplifiers.

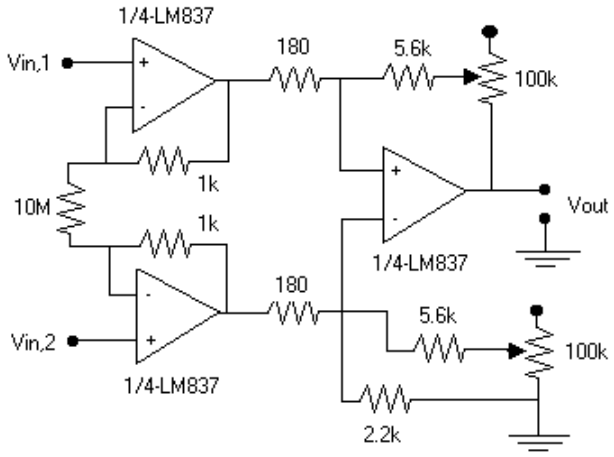

Figure 4.11 Original NSWCDD SHPB Instrumentation Amplifiers

The amplifiers built for the SHPB were designed to be adjustable gain, low noise instrumentation amplifiers with external nulling capabilities. The adjustable gain and external offset nulling capabilities are provided via the 100 kΩ potentiometers included in the circuit. Note that all of the values shown in Figure 4.9 are in ohms. To summarize the original design, a three op-amp instrumentation amplifier with adjustable gain and external offset nulling was built using the LM837 low noise quad op-amp.

At the heart of these instrumentation amplifiers HB-1 and HB-2 built for the SHPB at Dahlgren are the LM837 quad op-amps. Essentially, the LM837 is a 14-pin dual in-line (DIN) package consisting of four individual, low noise op-amps. Thus, 1/4-LM837, as used in Figure 4.11, refers to a single op-amp in the LM837 quad op-amp package. Referring to the specification sheet included in the supplement to this thesis, the LM837 has a gain-bandwidth product GBP of 25 MHz (gain*bandwidth = 25 MHz) with a slew rate of 10 V/μs. Figure 4.12 below shows a schematic of the LM837 quad op-amp.

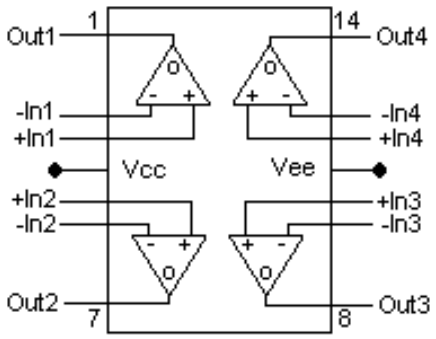

Figure 4.12 National Semiconductor LM837 Quad Op-Amp (DIN Package)

Figure 4.12 shows the four individual op-amps and their corresponding input and output terminals. Vcc and Vee are the positive and negative supply voltages, respectively. The numbers shown at each corner of the amplifier indicate the pin numbers (14 pins total). As originally built, only three of the four op-amps in the LM837 were used.

Thorough inspection and testing of HB-1 and HB-2 revealed that neither of the two instrumentation amplifiers was operating correctly. It was found that both amplifiers exhibited an unusually high sensitivity to noise and drift in addition to the problems specific to each amplifier: Amplifier HB-1 was found to have an open AC coupling capacitor while amplifier HB-2 was found to have a cracked R6 resistor. In addition, it was discovered that 5% tolerance resistors were used in the original construction of the amplifiers in lieu of the preferred 1% tolerance resistors. These findings led to the

complete teardown, overhaul and testing of the amplifiers such that satisfactory performance could be assured.

To improve the noise rejection capability and electrical and mechanical stability of the amplifiers, several modifications to the original amplifier circuits were proposed:

1. Replace 5% resistors with 1% tolerance resistors (critical resistors only).
2. Remove the adjustable gain potentiometer and replace with fixed resistor.
3. Replace external null potentiometer and process nulling voltage through 4th stage of LM837.

Replacing the 5% R4 and R6 resistors with 1% resistors would give the amplifier much better thermal and electrical stability since 1% resistors are much less sensitive to ambient conditions such as temperature and bias currents. In addition, the R4 and R6 resistors of the instrumentation amplifier have the greatest effect on the CMRR [13]. Consequently, these resistors should be closely matched to ensure acceptable CMRR. Removing the adjustable gain feature by replacing the gain adjust potentiometer with a fixed resistor was done to rid the circuit of an additional source of instability since typical potentiometers exhibit sensitivity to ambient conditions including temperature, humidity and vibration. Redesigning the external offset nulling feature to utilize the 4th stage of the LM837 and a more rugged, low-drift potentiometer was done to negate any ground loop effects that may have been present in the original design. With these changes completed, the NSWCDD instrumentation amplifiers took the form shown in Figure 4.13:

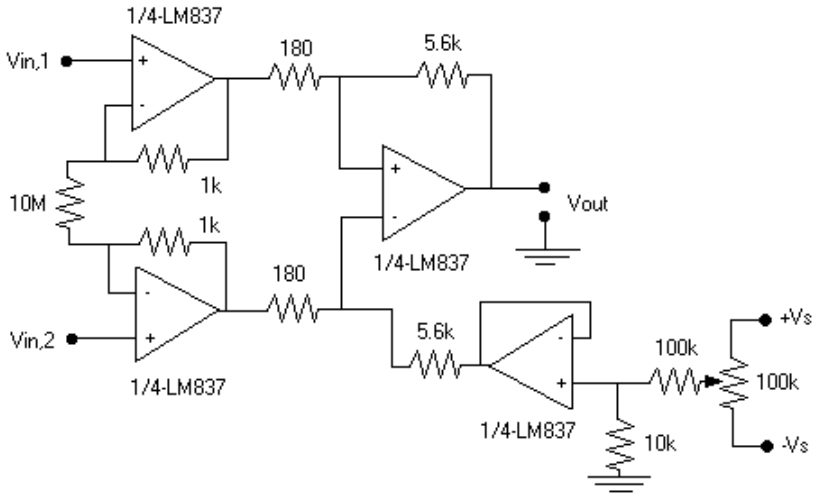

Figure 4.13 Modified NSWCDD SHPB Amplifier Schematic

The two redesigned instrumentation amplifiers were thoroughly checked and tested before being returned to service. With the addition of the fixed resistor in lieu of the gain adjust potentiometer, the gains for the two amplifiers was fixed at 31.4 V/V and 31.2 V/V, respectively. Figure 4.14 below is the experimental frequency response of the two amplifiers.

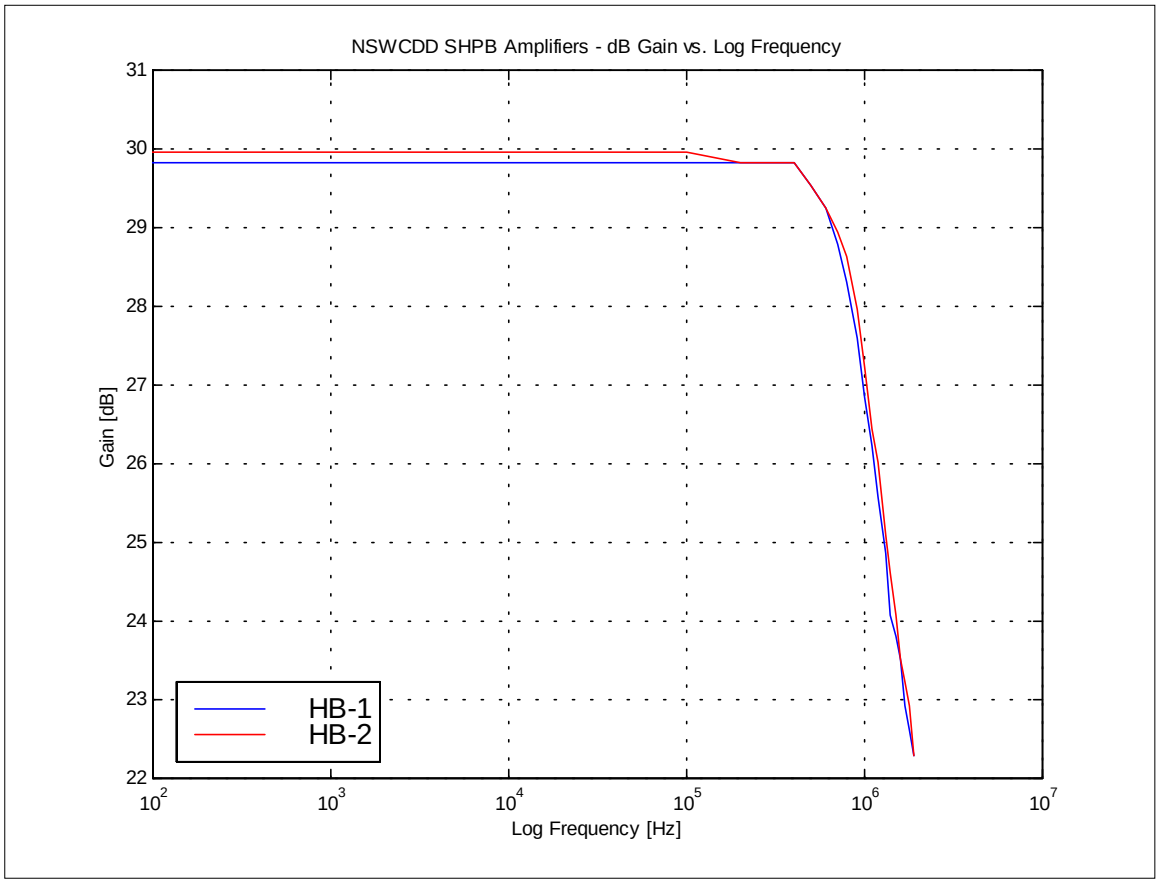

Figure 4.14 Frequency Response of NSWCDD SHPB Amplifiers

As Figure 4.14 shows, the bandwidths of the HB-1 and HB-2 amplifiers are approximately 1.02 MHz and 1.04 MHz (-3 dB method), respectively. The redesigned amplifiers also exhibited improved stability, increased common mode and noise rejection and less sensitivity to ambient conditions. Table 4.2 below summarizes the performance of the redesigned instrumentation amplifiers HB-1 and HB-2:

Table 4.2 Amplifier Specifications for HB-1 and HB-2

PARAMETER	HB-1	HB-2
Gain	31.4 V/V	31.2 V/V
Bandwidth	1.02 MHz	1.04 MHz
CMRR	99 dB	97 dB
Drift	<2.0 mV/min	<2.0 mV/min

Next to be inspected and tested were the strain gage completion networks. These circuits consist of the two bridge completion resistors (1000 Ω, ± 5%) to balance out the two strain gages attached to the pressure bars. In addition, the circuit also includes the bridge balance potentiometer. The circuitry involved in completing and balancing the bridge, shown previously in Figure 4.2, is shown again below in Figure 4.15.

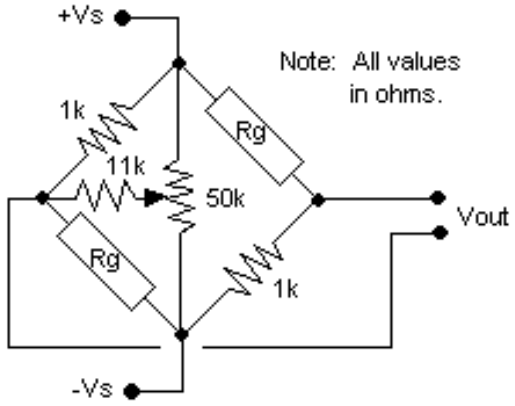

Figure 4.15 NSWCDD Half-Bridge Strain Gage Completion Networks

Upon inspection and testing of WB-1 and WB-2, it was found that all resistors were 1% tolerance. In addition, tests showed that the bridge completion circuits are performing as designed. Thus, no modifications were made to the strain bridge completion networks.

4.5 Optical Strain Measurements in the SHPB

With a basic understanding of the optical method of strain measurement designed for this research, the need exists to relate specimen diameter changes to equivalent strain and strain rate. Typical SHPB data is tabulated in terms of true strain and true strain rate. The equation for true strain is given below in Equation 4.4:

$$\varepsilon_{True} = \ln\left(\frac{l}{l_0}\right) \qquad \textbf{(4.4)}$$

In Equation 4.4, l is the instantaneous specimen length while l_0 is the initial specimen length. It is, therefore, necessary for the development of a functional relationship between the specimen diameter data reported by the optical detector and corresponding specimen true strain. Once this relationship is established, true strain rate can be computed by differentiation of the true strain with respect to time. These relationships are developed in the next section.

4.5.1 Optical Method of Strain Measurement

In performing this equation development, it is necessary to recall the assumptions of a uniaxial state of stress with homogeneous deformation. This requires, among other things, adequate specimen-pressure bar lubrication and proper pressure bar-specimen alignment. In relating specimen diameter to true strain requires definition of two terms originally put forth by Ramesh and Narasimhan [19]. These terms are the radial stretch ω and axial stretch λ:

$$\omega(t) = \frac{r(t)}{r_0} \tag{4.5}$$

$$\lambda(t) = \frac{l(t)}{l_0} \tag{4.6}$$

In 4.5 and 4.6, $r(t)$ and r_0 are the instantaneous specimen radius and initial specimen radius, respectively while $l(t)$ and l_0 are the instantaneous length and initial length of the specimen, respectively. Defining a rectangular coordinate system in which x_1 defines the axial state of the specimen while x_2 and x_3 define the radial state of the specimen, a corresponding deformation gradient can be developed from the series of relations shown in 4.5 and 4.6. This deformation gradient takes the form

$$\vec{F} = \lambda(t)\hat{x}_1\hat{x}_1 + \omega(t)\left[\hat{x}_2\hat{x}_2 + \hat{x}_3\hat{x}_3\right] \tag{4.7}$$

In Equation 4.7, the '^' is used to denote unit vectors in the specified direction. In the plastic deformation regime, it is understood that both plastic and elastic deformation contribute to this deformation gradient. Thus,

$$\vec{F} = \vec{F}_e \vec{F}_p \tag{4.8}$$

Assuming homogeneous, translational deformation only, the plastic deformation within the specimen can estimated as

$$\vec{F}_p = \lambda_p(t)\hat{x}_1\hat{x}_1 + \omega_p(t)\left[\hat{x}_2\hat{x}_2 + \hat{x}_3\hat{x}_3\right] \tag{4.9}$$

In addition, the elastic deformation component can be defined as follows:

$$\vec{F}_e = \frac{\lambda}{\lambda_p(t)}\hat{x}_1\hat{x}_1 + \frac{\omega}{\omega_p(t)}\left[\hat{x}_2\hat{x}_2 + \hat{x}_3\hat{x}_3\right] \tag{4.10}$$

In Equations 4.9 and 4.10, $\lambda_p(t)$ and $\omega_p(t)$ are the plastic axial and radial stretches, respectively. In most plastic deformation applications, the elastic deformation is considered negligible with respect to the plastic deformation. This is an oft-used approximation in SHPB experiments since plastic deformation is the end result of this experimentation. One explanation for this assumption is the inability to characterize the elastic behavior of materials subjected to highly plastic deformations. Additional commentary into this idea will be presented in Chapter 5. For now, however, the assumption of negligible elastic deformation will be used to equate the total deformation gradient (4.7) to the plastic deformation gradient (4.9). Thus,

$$\vec{F} = \vec{F}_p = \lambda_p(t)\hat{x}_1\hat{x}_1 + \omega_p(t)\left[\hat{x}_2\hat{x}_2 + \hat{x}_3\hat{x}_3\right] \tag{4.11}$$

This analysis can only be carried further via the assumption that plastic deformations are, on a "microstructural" level, incompressible. In other words, any plastic deformation within the specimen will yield a corresponding change in the physical nature of the specimen. This constraint can be represented as follows in 4.12:

$$J = \det(\vec{F}) = \lambda\omega^2 = 1 \tag{4.12}$$

Rearranging 4.12 and recalling the definition of the axial stretch λ(t) yields

$$\lambda(t) = \frac{1}{\omega^2} = \frac{l(t)}{l_0} \tag{4.13}$$

True strain can then be computed as shown in Equation 4.14:

$$\varepsilon_{True} = \ln\left(\frac{l}{l_0}\right) = \ln(\lambda) \tag{4.14}$$

Finally, true strain rate can be computed by differentiation of the true strain with respect to time.

(4.15)

Thus, direct measurement of the radial stretch coupled with the incompressibility constrain of Equation 4.12 allows the use of the optical strain measurement system to completely determine specimen strain and strain rates. However, it must be remembered that these relations are valid for incompressible materials only. Application of this system to porous, more compliant materials should be thoroughly investigated prior to tabulation of any such results. This issue will be addressed in Chapter 6 after the presentation of the experimental results and conclusions.

4.5.2 Dynamic Testing with the SHPB

With both the electrical resistance strain gage and optical strain measurement systems designed, constructed and debugged, experimentation is the next step in this research. Before experimenting with the SHPB apparatus, however, a calibration curve must be constructed for the optical strain measurement system. This will consist of recording the voltage output for specially prepared specimens of various diameters. This data will allow the output voltage to be related to the specimen diameter. It is anticipated that this relationship will be linear in nature so as to simplify the post-processing routine. This calibration curve as well as the experimental data used in the overall analysis will be presented in Chapter 5**.**

Chapter 5. Experimental Results

5.1 Introduction

Chapter 5 will begin the presentation of the results of the SHPB experiments utilizing the optical method of strain measurement as well as the corresponding strain gage data. The strain gage data is necessary for two reasons: First, this information will provide a set of baseline data against which the data recorded using the laser system can be compared and secondly, the strain gage on the output pressure bar will be needed in order to determine specimen stress. As previously explained, the ability to measure specimen strain directly at the specimen with the laser will rid the analysis of the errors associated with the input bar strain gage including thermal, electrical and lateral sensitivities, averaging effects and input bar dispersion. Thus, even though the output bar strain gage will be a necessary part of the optical method of strain measurement, it is anticipated that the accuracy, precision and repeatability of the data will be greatly improved due to the removal of the input bar strain gage. These issues will be introduced in Chapter 5 and addressed more thoroughly in Chapter 6.

5.2 Experimental Techniques

In order to ensure that the optical system of strain measurement is properly configured to acquire data, several subtleties must first be addressed. These subtleties include positioning the optical rail assembly properly with respect to the SHPB specimen and performing a calibration procedure in order to determine the relationship between the output voltage from the photodetector and the specimen diameter. Should the laser not be perpendicular to the diameter of the specimen, a nonlinear response will result. Dr. Andy Barker, a scientist who provided a great deal of support on this project, specified that the laser should be perpendicular to the specimen within approximately 2˚ to ensure that the cross sectional diameter of the specimen is measured. Also, a precise calibration procedure should be accomplished before each set of experiments to verify the calibration factor. This calibration factor will ultimately be used to convert the voltage output from

the photodetector to a corresponding diameter measurement for use in determining the specimen strain and hence, strain rate. It should be noted that any alignment problems with the optical rail will have detrimental effects on the response of the detector, namely, in the form of nonlinear detector output.

5.2.1 Optical Rail Alignment

There are two primary concerns in setting up the optical strain measuring system: First, ensuring that each individual component of the system is precisely positioned and aligned on the optical rail and second, ensuring that the entire optical rail assembly is positioned correctly with respect to the SHPB specimen. Figure 5.1 below illustrates the specified positions of the individual components of the optical strain measuring system.

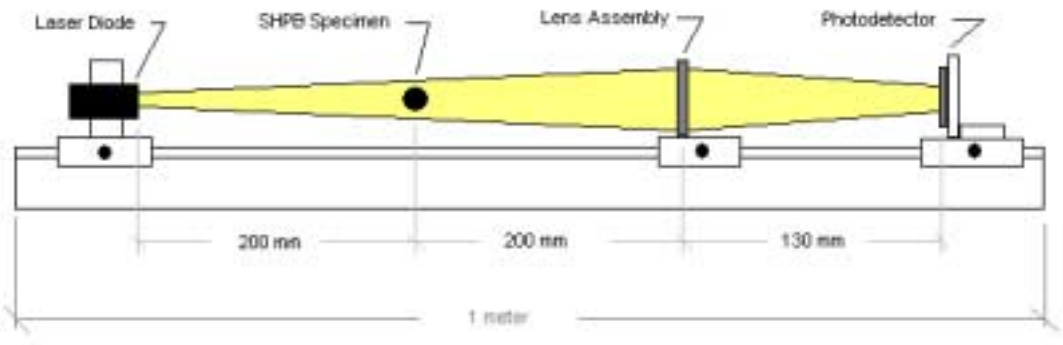

Figure 5.1 Optical Rail Component Layout Dimensions

From consultations with Dr. Barker as well as experimental data gathered in the laboratory, it was found that the component dimensions shown above would provide the best compromise between signal strength and system versatility. Moving the laser closer to the specimen would increase the strength of the recorded signal but the length of the line generated at the specimen could fail to span the entire diameter of the deformed specimen. Thus, the dimensions listed in Figure 5.1 should be used when configuring the optical system for use in the SHPB. However, once the components are oriented as shown above, the strength of the detector output can be maximized with additional adjustments to the photodetector assembly. This involves adjusting the horizontal,

vertical and lateral position of the detector until the incident laser light is focused to a point at the center of the detector. Likewise, maximum signal strength will be realized only if the laser is focused properly. The distance between the collimating lens and the detector, however, is locked by the focal length of the lens (100 ± 2mm). These issues will be explained further in the following section.

Proper alignment of each individual component on the rail can be assumed since all components were mounted in specially designed mounting brackets supplied by the various manufacturers. As specified in Chapter 4, the Newport X-95-1 optical rail has the mechanical tolerances specified below in Table 5.1:

Table 5.1 Newport X95-1 Optical Rail Tolerances

Mechanical Tolerance	Value
Bending Tolerance	0.80 mm/m
Twisting Tolerance	0.75 mm/m

The values listed in Table 5.1 indicate that minimal bending and twisting of the optical rail can be expected. In addition, each component bracket used in this design, e.g. laser diode bracket and lens holders, was mounted to pre-drilled and tapped holes in the carrier rails. Product literature found in the attached supplement shows that the tolerances used in machining these parts satisfies the alignment criteria specified above (±2˚). To verify this assumption, each component was measured with a set of calipers and a squaring-tee such that perpendicularity of the components was assured. Again, specifications for all of the hardware used in this thesis can be found in the supplement supplied with this thesis.

Proper positioning of the entire rail assembly was accomplished by mounting a pair of support stands to the floor in the laboratory in Dahlgren. Prior to lagging the supports to the floor, however, each stand was measured and adjusted such that the rail, when installed on the supports, would be perpendicular (±2º) to the specimen. This was done

using a straightedge and squaring-tee. Measurements of the distances between the optical rail and adjacent bearing blocks were also recorded and compared to be sure the rail was aligned properly. Figure 5.2 below illustrates the structural support designed for the optical rail.

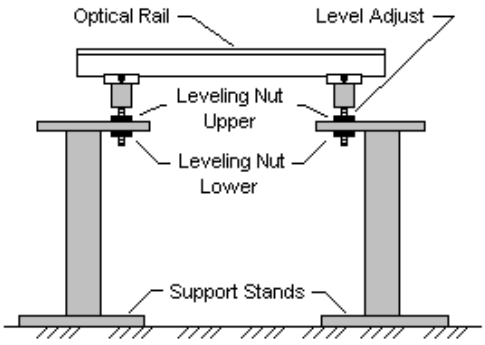

Figure 5.2 SHPB Optical Rail Support Structure

Note the upper and lower adjustment nuts that can be used to level the rail or provide additional local vertical adjustment. A total of three level adjusts were incorporated into the design such that adjustments can be made individually. This avoids the statically indeterminate condition resulting from four level adjust mechanisms. Vertical adjustment of the optical rail will be discussed in the next section when the calibration technique is thoroughly explained. Most importantly, however, the proper positioning of the optical rail and its components will be verified through the examination of the detector output. A linear response from the optical detector will verify that each individual component as well as the entire rail assembly is adequately positioned. Again, this will be discussed in the following section.

5.2.2 Calibration Procedure

Prior to gathering data with the optical strain measuring system, a calibration procedure must first be followed in order to determine the relationship between specimen diameter and output voltage. This procedure entails the static measurement of the diameter of a series of eight undeformed test specimens. Gary Bass at NSWCDD assembled calibration kits for the 0.50" and 0.75" diameter bars containing the calibration specimens as well as alignment tools for aligning the specimens at the center of the pressure bars.

The specimen sizes selected for the calibration range in diameter from 0.0625” to 0.500” in uniform increments of 0.0625”. Thus, the calibration kit consists of 8 specimens: 0.0625”, 0.125”, 0.188”, 0.250”, 0.313”, 0.375”, 0.438” and 0.500”. An alignment tool was constructed for each calibration specimen such that the specimen can be centered on the pressure bars. This calibration tool concept was originally conceived by Benny Simpson of NSWCDD and first put to practical use by Mike Kaiser as a method of specimen placement in the SHPB. Figure 5.3 illustrates the manner in which the calibration specimen is centered in the SHPB using these alignment tools:

Figure 5.3 Specimen Alignment Procedure for NSWCDD SHPB

The calibration procedure involves placing each calibration specimen in the SHPB via its particular alignment tool. Before outlining the procedure necessary for proper calibration, Figure 5.4 is presented below to familiarize the reader with the various components and component adjustments associated with the calibration procedure.

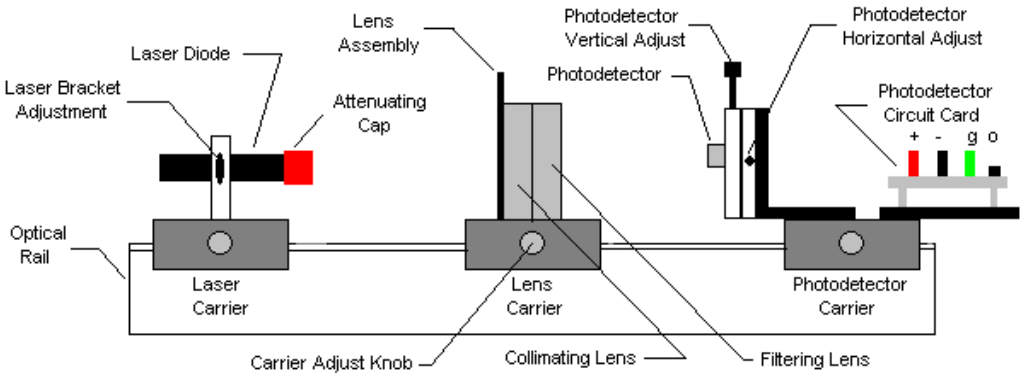

Figure 5.4 NSWCDD SHPB Optical Rail Components and Adjustments

With Figure 5.4 presented above, the steps involved in the calibration process are as follows:

1. Ensure that the red beam-attenuating cap is affixed on the output end of the semiconductor laser diode.
2. Make the following electrical connections:
    a. Laser Diode – switch the AC adapter to the 6-volt position and connect it to the end of the laser diode power cord. Plug AC adapter into wall outlet (120 VAC).
    b. Photodetector – connect +25 volts, -25 volts and ground to the red, black and green banana terminals, respectively, on the photodetector circuit card. Connect a coaxial cable between the photodetector output (BNC) and Channel 3 of the digital oscilloscope (BNC).
    c. Oscilloscope – plug the male plug into the female wall outlet (120 VAC).
3. Switch the semiconductor laser diode, photodetector power supply and digital oscilloscope power to the 'on' position.
4. Adjust each of the rail carriers as follows:
    a. Laser Diode – loosen the carrier-locking knob and move the laser carrier until its rear edge is aligned with the black line across the top of the rail.
    b. Collimating Lens – loosen the carrier-locking knob and move the lens carrier until its front edge is aligned with the red line crossing the top of the rail.
    c. Photodetector – loosen the carrier-locking knob and move the photodetector carrier until its front edge is aligned with the blue line across the top of the rail.
5. Place the 0.0625" calibration specimen in between the input and output pressure bars using the 0.0625" alignment tool.
6. Remove the beam-attenuating cap from the laser diode.
7. Verify that the laser is generating a sharp, vertical line of light at the center of the calibration specimen. If not, loosen the clamp securing the laser diode and rotate the laser until a vertical line is achieved on the specimen. If necessary, adjust the

position of the laser and/or specimen to center the beam on the specimen. Should vertical adjustment of the laser be necessary, loosen the lock nuts on the support stand and adjust the optical rail as required.

8. Adjust the vertical and horizontal position of the photodetector such that the light not occluded by the calibration specimen is focused to a point at the center of the photodetector. If necessary, adjust the photodetector carrier forward or aft by loosening the carrier-locking knob and moving it as necessary to achieve a highly focused point of light at the center of the photodetector.
9. Replace the ambient light filter between the collimating lens and photodetector.
10. Trigger the oscilloscope such that the output voltage from the photodetector can be recorded. Record the voltage output and replace the beam-attenuating cap.
11. Repeat steps 5-10 for the 7 remaining calibration specimens.
12. Generate the corresponding calibration curve by plotting specimen diameter (in) versus output voltage (V). Fit a curve to this data and determine the slope of the line. The equation of the linear curve fit will serve as the calibration relationship.

Should the calibration curve be nonlinear, attention should be given to the laser diode. In particular, the laser should be refocused such that a 250 μm wide line of light is generated at the location of the SHPB specimen. Instructions for focusing the laser can be found in supplement included with this thesis. In addition, it is also imperative that the optics of the laser be positioned correctly such that a line of uniform intensity is generated at the specimen. Note, however, that this procedure should be followed only if a nonlinear calibration curve results from the procedure described above.

5.3 Experimental Results

As detailed above, the steps involved in using the optical method of strain measurement designed for the SHPB at NSWCDD include performing a static calibration of the optical system, determining the calibration factor for converting voltage output to a corresponding specimen diameter and post processing the data to generate the following information:

1. True Strain vs. Time
2. True Stress vs. Time
3. True Strain Rate vs. Time
4. True Stress vs. True Strain

In order to generate these plots, the output from the photodetector and output bar strain gage will be needed. The procedure followed in gathering this data is presented below.

5.3.1 Experimental Calibration Results

As detailed previously, the initial step in preparing for data acquisition is to perform the calibration procedure outline in Section 5.2.2. Carefully placing each calibration specimen in the SHPB yielded the output voltage values listed below in Table 5.2:

Table 5.2 Detector Output Voltage for Calibration Specimens

Specimen [in]	Output [V]
0.0625	1.515
0.125	1.295
0.188	1.073
0.250	0.855
0.313	0.635
0.375	0.415
0.438	0.195
0.500	0.025

The calibration values listed in Table 5.2 were gathered using the calibration technique outlined in Section 5.2.2. Again, the importance of centering the calibration specimen between the two pressure bars is stressed since this is the only method of minimizing the effects of nonuniform beam intensity across the length of the generated line. However, any misalignment of the laser with the specimen will contribute to a lack of linearity in

the corresponding calibration curve. Thus, a linear calibration curve will ensure proper beam–specimen alignment.

With the calibration data listed in Table 5.2, the corresponding calibration curve is shown below in Figure 5.5:

Figure 5.5 NSWCDD Optical Strain Calibration Curve (TEK59, TEK61, TEK62)

Figure 5.5 displays the calibration data for experiment serial numbers 59, 61 and 62 with a 1st order curve fit. In order to obtain the desired calibration relationship directly, the independent specimen diameter has been plotted on the y-axis while the dependent voltage output has been plotted on the x-axis. Once the measured data was plotted, a 1st order curve fit was generated to quantify the linearity of the calibration. Error bars included with the curve fit show a maximum error of 2.88% at a specimen diameter of 0.0625". With a standard deviation of 0.1351 volts, the 95% confidence level (2σ) is

0.2702 volts, both of which are well above the maximum residual of 0.0018 volts. In addition, the standard deviation is 8.91% of the full-scale voltage output line fit. Thus, it can be concluded that the optical detector is generating a linear response. The resulting 1st order equation, which will be used to relate the detector output voltage to an equivalent specimen diameter, is shown above in Figure 5.5 and is repeated below in Equation 5.3:

$$P_1 = A_0 E \frac{\partial u_1}{\partial x} \quad \textbf{(5.3)}$$

In Equation 5.3, the slope of the line is –0.28445 and the y-intercept is 0.49276. It should also be pointed out that the 0.500" diameter calibration specimen was not used because, when placed in the path of the beam, the detector output (25 mV) encroached below the noise floor of the detector (~30 mV). Thus, it was determined that an accurate detector output could not be recorded for the 0.500" diameter specimen and it was, consequently, removed from the calibration procedure. However, the other seven calibration specimens provided enough data to ensure a linear, 1st order response.

With the calibration procedure complete, dynamic testing can begin. It should be remembered, though, that any modifications made to the optical rail or any of its components will necessitate the re-calibration of the optical system. Thus, it is imperative that the optical rail be adjusted as little as possible throughout the dynamic testing phase of the research.

5.3.2 Experimental Dynamic Testing

Performing dynamic test using the compressive SHPB requires a great deal of attention in order to ensure adequate safety. Important safety considerations include the proper handling and setup of the medium pressure gas gun, the proper placement of the safety shielding and adequate separation of personnel from the SHPB apparatus. With these safety issues in mind, dynamic testing was done for the following materials: 6061-aluminum and copper.

For NSWCDD's records, these tests were designated as serial number 59, 61 and 62, respectively. The analysis will begin by presenting the incident, transmitted and laser signals for SN 62, the dynamic compression of copper. Initially, however, a pretest Matlab program written by the University of California San Diego and implemented by Leonard Wilson of NSWCDD is utilized to compute required experimental parameters. Input parameters include specimen length and diameter while calculated parameters include gas gun breech pressure and expected specimen final diameter. The results of this routine for SN-62 are summarized below:

Table 5.3 Pretest Experimental Parameters (NSWCDD SHPB SN-62)

SN-62 Test Parameters	
Sample Material	Copper
Initial Diameter	0.201 in
Initial Length	0.202 in
Sample Mass	0.3 g
Desired Strain	0.2 in/in
Bar Diameter	0.75 in
SN-62 Calculated Values	
Final Diameter	0.225 in
True Strain	0.223 in/in
Strain Rate	1592 in/in-s
Breech Pressure	10.36 psi
Incident Bar Stress	27954 psi

As shown in the table above, the copper test specimen is 0.201" in diameter and 0.202" in length. The desired sample strain is 0.2 in/in while the calculated true strain is 0.223 in/in. This results in a true strain rate of 1592 in/in-s and a final specimen diameter of 0.225 ". In addition, the computed input pressure bar stress is 27954 psi, well below the

elastic limit of 370 ksi. Additional parameters calculated but not shown include striker bar velocity, strain levels in each of the pressure bars and maximum stress bridge output. For a more complete review of this pretest routine, the reader is referred to Kaiser [18].

For the experiments, the breech pressure was set to 15 psi and the digital storage scope was configured to record 2500 data samples over a 1 ms time interval. This corresponds to a sampling frequency of 2.5 MHz. The incident strain signal was recorded on Channel 1, the transmitted strain signal was recorded on Channel 2 and the laser signal was recorded via Channel 3. Figure 5.6 below shows the output from the three channels of the oscilloscope.

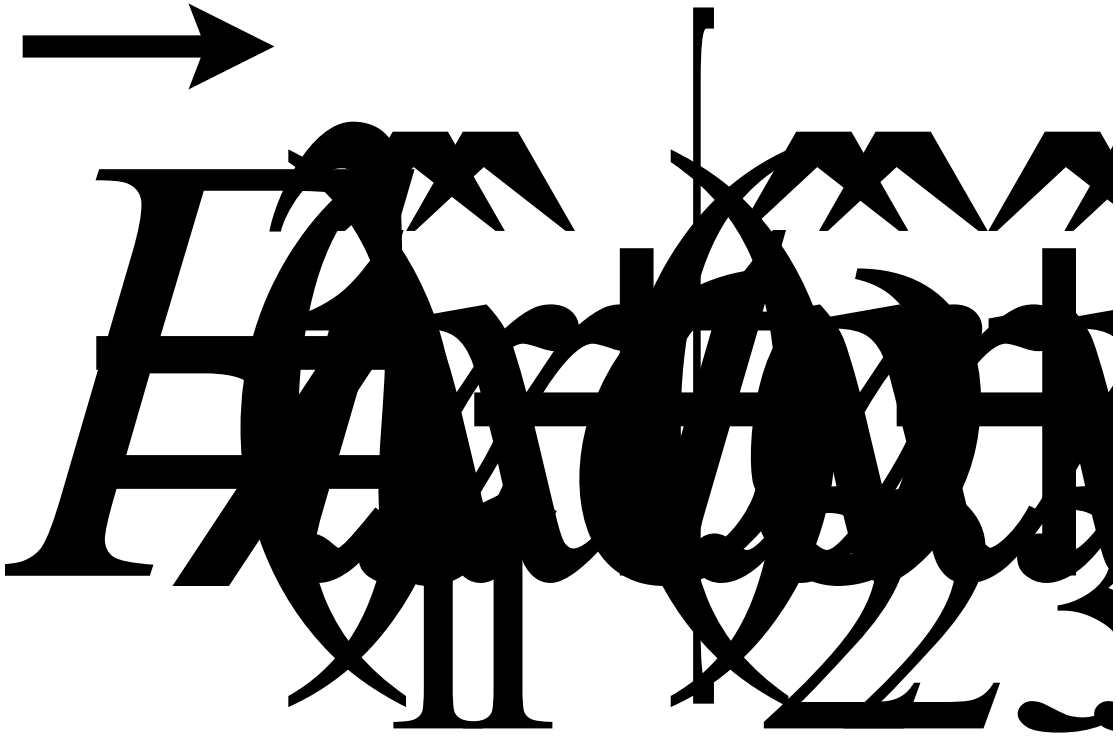

Figure 5.6 3-Channel Output for NSWCDD SHPB Experiment 62

In Figure 5.6, the upper, center and lower plots correspond to the incident, transmitted and optical signals, respectively. The incident signal consists of the incident pulse, which begins at approximately 0 ms (a time delay was set for –0.1 ms) as well as the reflected pulse which appears at approximately 0.3 ms. Examining the transmitted pulse, the transmitted wave reaches the output bar strain gage at approximately 0.32 ms. Both the incident and transmitted strain histories show stress waves "trapped" within the input and output pressure bars, respectively. This phenomenon is evidenced by the nonzero signals occurring later in the time histories of the two bars. Within the input and output bars, this trapped pulse begins at approximately 625 μs. These additional pulses are due to stress wave reflection at the flat ends of the pressure bars and should not be confused with the reflected wave within the incident bar that is used to compute specimen strain. The phenomenon of bar dispersion is also evident in the strain histories. It can be seen that dispersion corrupts the signals in that peak and average strain magnitudes are not readily apparent. This dispersive error, as noted earlier in this thesis, is one of the motivating factors behind this research. Note, however, that both incident and transmitted signals presented above were corrected for bar dispersion utilizing Kaiser's [18] dispersion correction routine in use at NSWCDD. The dispersion-corrected signals are shown more clearly in Figure 5.7 below:

Figure 5.7 Dispersion Corrected Reflected and Transmitted Strain Histories (NSWCDD SHPB 62)

In Figure 5.7, note the effects of dispersion on the reflected pulse compared with the effects on the transmitted pulse. Obviously, the effects are greater on the reflected pulse. Thus, replacing the incident bar strain gage with the optical strain measurement system employed here will significantly reduce the uncertainty due to pressure bar dispersion. Also note the phase distortion resulting from the dispersion correction. Although not a desirable result of the process, this phase distortion will have no significant effects on further signal processing since only relative magnitude information will be of interest. In addition, the magnitude offset present in the transmitted signal is a result of the mean zeroing of the data during post processing. Again, this has little bearing on the analysis.

The laser signal, shown in the lower plot of Figure 5.6, shows arrival of the stress wave at the specimen at approximately 170 μs. Traveling one-half the length of the 5' input bar in 155 μs, this corresponds to a stress wave velocity of approximately 187,500 in/s or 10,200 mph. This relates favorably to the computed theoretical infinite wavelength velocity C_0 $\left(C_0 = \sqrt{\frac{E}{\rho}} \right)$ of 191,000 in/s. Regardless, the optical strain measurement system shows the decreasing detector output as the specimen diameter grows due to the plastic deformation caused by the mechanical stress wave. It also shows the duration of the dynamic compressive event is approximately 160 μs. Even without further processing of the optical data, the information presented in this paragraph is data that had not been previously experimentally verified by SHPB investigators.

5.3.3 Post Processing (NSWCDD SHPB SN-62)

The next step in processing the recorded data involves conditioning the signals for further analysis. As shown previously in Figure 5.6, the strain histories can be conditioned via a dispersion-correction algorithm that predicts the initial form of the compressive stress wave and, utilizing pressure wave velocity data for the particular pressure bar material in use, calculates the non-dispersed form of the strain signal. This procedure has been used for many years by SHPB investigators. As mentioned in the previous section, this research was done using Kaiser's dispersion-correction routine.

The optical signal presented in Figure 5.6 is shown again below in Figure 5.8 for further analysis.

Figure 5.8 Optical Detector Output Signal (NSWCDD SHPB 62)

Note in Figure 5.8 the "choppiness" of the signal during both its steady state and transient response regimes. This can be attributed to the digitization (analog to digital conversion) within the Tektronix TDS744A Digital Storage Oscilloscope as well as noise generated by the circuitry used in the optical detector assembly. More commonly referred to as digital noise, it has no significant effects on the quality of the signal but presents great challenges when further processing of the signal is required. In this research, this output signal will ultimately used to compute specimen strain and hence, strain rate. Before proceeding with these computations, this digital noise must first be removed do that the differentiated signal will not be dominated by nondeterministic content (noise).

In order to design a digital filter, the frequency content of the signal must first be examined in order to determine what content to pass and which content to remove. This was done via a Finite Fourier Transform (FFT). The FFT is a method of transforming a signal from the time domain to the frequency domain for identification of spectral content. The FFT of the optical detector signal is shown below in Figure 5.9:

Figure 5.9 Frequency Content of Photodetector Signal 62 (NSWCDD SHPB 62)

Examination of the upper plot in Figure 5.9 shows the majority of the spectral content contained in the lower frequency range. This can be better seen in the lower plot in Figure 5.9, the low frequency spectral content. Numerically, 99.99% of the spectral energy is contained in the frequencies below 10 kHz. Thus, it was determined that a low pass filter would be used to remove the high frequency noise within the detector signal.

Research into digital filter design revealed the availability of two types of digital filters: Infinite Impulse Response (IIR) and Finite Impulse Response (FIR) filters. Briefly, FIR filters guarantee a stable, linear response with zero phase distortion while IIF filters can have a tendency to go unstable at higher orders. In addition, FIR filters are better suited for lower maximum bit data acquisition systems due to their more simplistic implementation routine [20]. Sequentially, the FIR filter is implemented as shown in Equation 5.3:

$$v(x,t) = \frac{1}{\rho C_o} p(x,t) \tag{5.3}$$

In essence, the FIR filter involves the convolution of a windowing-type function with the signal of interest. The output sequence *y(n)* is the result of the convolution of the unit sample response of the system *h(n)* with the signal *x(n)*. This results in Equation 5.3.

In the Matlab post processing of the data, an elliptic filter was designed such that low frequency content would pass while all higher frequency content would be removed. The elliptic filter allows specification of passband and stopband frequencies (in terms of the Nyquist frequency) as well as the passband and stopband attenuation levels. Further analysis of the FFT shown in Figure 5.8 led to the filter specifications shown in Table 5.4:

Table 5.4 Elliptic Filter Specifications (NSWCDD SHPB)

Filter Specification	Value
Pass Frequency ω_p	$0.1*f_{NYQ}$
Stop Frequency ω_s	$0.2*f_{NYQ}$
Pass Ripple R_p	0.1 dB
Stop Ripple R_s	50 dB

With a sampling frequency of 2.5 MHz, the corresponding Nyquist Frequency f_{NYQ}, according to the Sampling Theorem, is 1.25 MHz. Thus, a passband frequency ω_p of 125 kHz is realized while the stopband frequency ω_s is set at 250 kHz. The passband ripple was specified as 0.1 dB (minimum attenuation) while the stopband attenuation was set at 50 dB (maximum attenuation). With these filter specifications (implemented in Matlab as 'elliptic') coupled with Matlab's 'filtfilt' zero phase shift filtering routine, the elliptic filter exhibits the following frequency response:

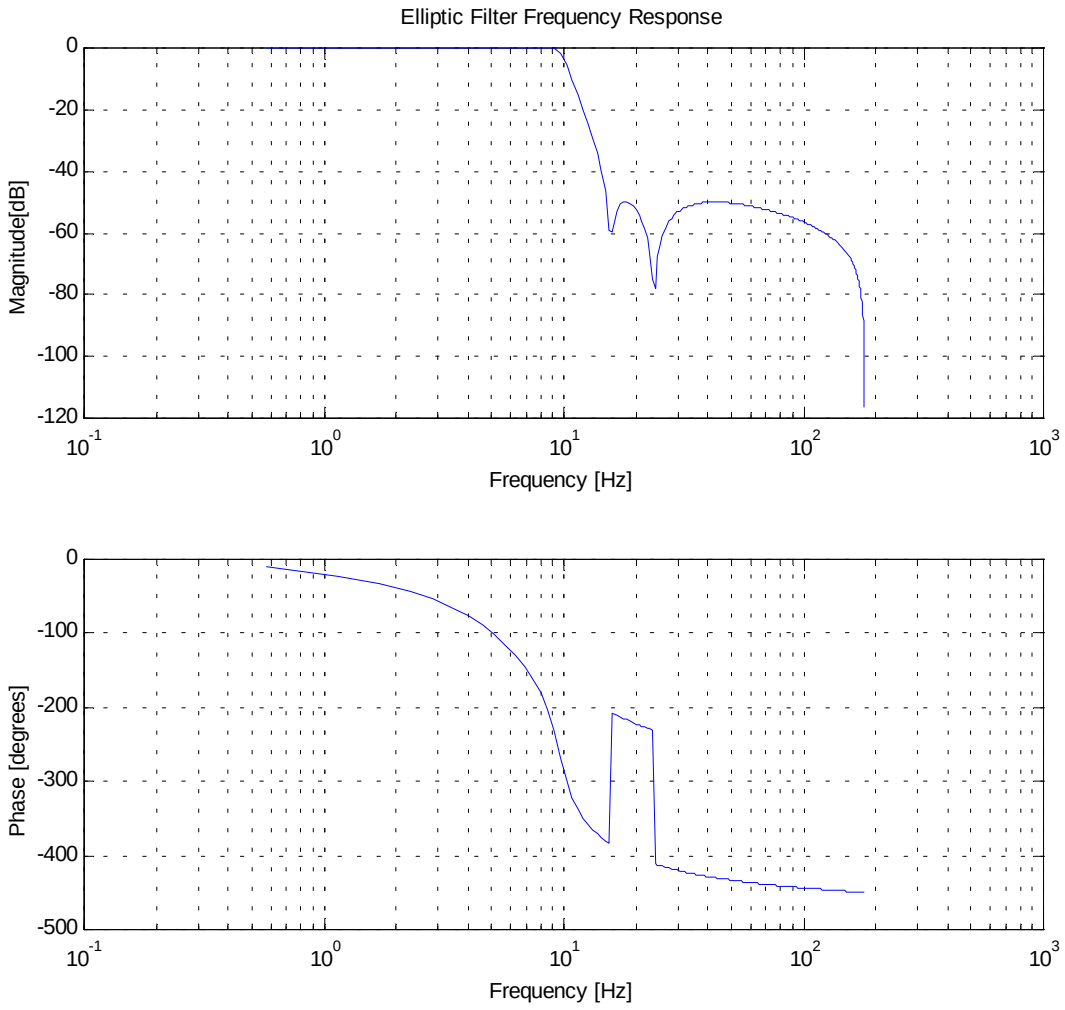

Figure 5.10 Elliptic Filter Frequency Response (NSWCDD SHPB)

Figure 5.10 shows little attenuation in the magnitude of the low frequency passband content with 50 dB or greater attenuation in the stopband regime. It must be noted that the frequency axis in Figure 5.10 is relative to pi and normalized to the Nyquist Frequency. In addition, the filter displays an acceptable phase loss as the filter approaches the passband-to-stopband transition regime. However, the final test of the filter's performance will come in the analysis of the unfiltered detector output signal superimposed on the filtered output. This is shown below in Figure 5.11.

Figure 5.11 Unfiltered and Filtered Optical Detector Output (NSWCDD SHPB 62)

In Figure 5.11, both the filtered and unfiltered signals are shown. As seen previously in Figure 5.8, the raw (unfiltered) detector output signal exhibits a significant amount digital

noise. The filtered signal, passed through the elliptic filter described in the preceding paragraph, provides effective noise attenuation and removal with minimal loss of signal strength. This same level of signal preservation was verified through the analysis of two additional sets of data (SN-59 and SN-61) and these results will be presented in following sections. From this analysis, it was concluded that the elliptic filter provides acceptable signal conditioning.

The next step in the analysis is to convert the filtered detector output to specimen diameter. This is done via the calibration relationship shown in Equation 5.2. This relationship is shown again in Equation 5.3 for further analysis:

$$P_1 = A_0 E \frac{\partial u_1}{\partial x} \quad \textbf{(5.3)}$$

This conversion is performed simply by inserting the filtered output signal from the detector into the 1st order, linear equation relationship shown in Equation 5.3. The result of this conversion yields the time history of the specimen diameter during the experimental event. This time history can be seen below in Figure 5.12:

Figure 5.12 Optically Measured Specimen Diameter History (NSWCDD SHPB 62)

In SHPB SN-62, the initial and final mechanically measured diameters of the copper specimen were found to be 0.201 in and 0.227 in, respectively. This compares favorably to the initial and final specimen diameters shown in Figure 5.12: 0.2011 in and 0.2261 in, respectively. Again, the increase in specimen diameter occurring at 800 μs was a result of the pressure bar interference with the beam of light. In comparison, pre-test calculations revealed an expected final diameter of 0.225 in. Thus, the error between and the mechanically measured and optically measured specimen diameters was 0.04% and 0.5% for the initial and final diameters, respectively. Note that all mechanical measurements were performed with a digital caliper.

Also worth noting in Figure 5.12 is the peak diameter achieved by the specimen (0.232 in). It was initially thought that this peak diameter was merely the barreling effect of nonuniform deformation within the specimen coupled with the translation of the specimen within the beam of light. This theory, however, was refuted by careful measurement of the deformed specimen. Additional measurements with the digital caliper reveal a measurable amount of barreling in the specimen but only on the order of 0.002 to 0.003 in., not the 0.006 in seen in Figure 5.11.A more plausible theory is that this peak diameter is the result of previously-immeasurable elastic deformation occurring within the specimen. It is known that, even in the plastic regime, elastic behavior still exists. However, few instrumentation methods have been able to capture this behavior. This theory will be addressed in forthcoming sections of this research.

Finally, the specimen diameter information can be converted to corresponding true strain and true strain rate by invoking the idea of plastic incompressibility. It is accepted that most metals and dense nonmetals exhibit incompressible behavior in the plastic regime. This is analogous to the idea of the conservation of specimen volume. This incompressibility issue was explored more deeply in Chapter 4 in development of the equations presented by Ramesh and Narasimhan. Summarizing this development, equations for true strain and true strain rate are shown in Equation 5.4 and 5.5, respectively:

(5.4)

(5.5)

Again, ω is defined as the radial stretch and, numerically, where $r(t)$ is the instantaneous radius of the specimen and r_0 is the initial radius of the specimen. With

these equations, the true strain and true strain rate for SHPB experiment SN- 62 are shown below in Figure 5.13:

Figure 5.13 Optically Measured True Strain and True Strain Rate (NSWCDD SHPB 62)

Again, the optical method of strain measurement utilized in this research allows identification of peak true strain and strain rate. In the copper specimen used in SN- 62, the peak strain can be seen to be approximately 0.2450 in/in while the peak strain rate was observed to be 1.3×10^4 in/in-s. These peak values can also be attributed to the elastic behavior of the specimen, behavior not previously seen in the strain gage data. In comparison with the strain gage data, the final strain achieved by the specimen was 0.219 in/in while the mean steady state true strain rate was found to be approximately 1680 in/in-s. This compares favorably to the computed strain and strain rate values of 0.2231

in/in and 1592 in/in-s. This results in a true strain error of 1.9% and strain rate error of 5.4%. This comparison is more easily understood by examination of Figure 5.14 below.

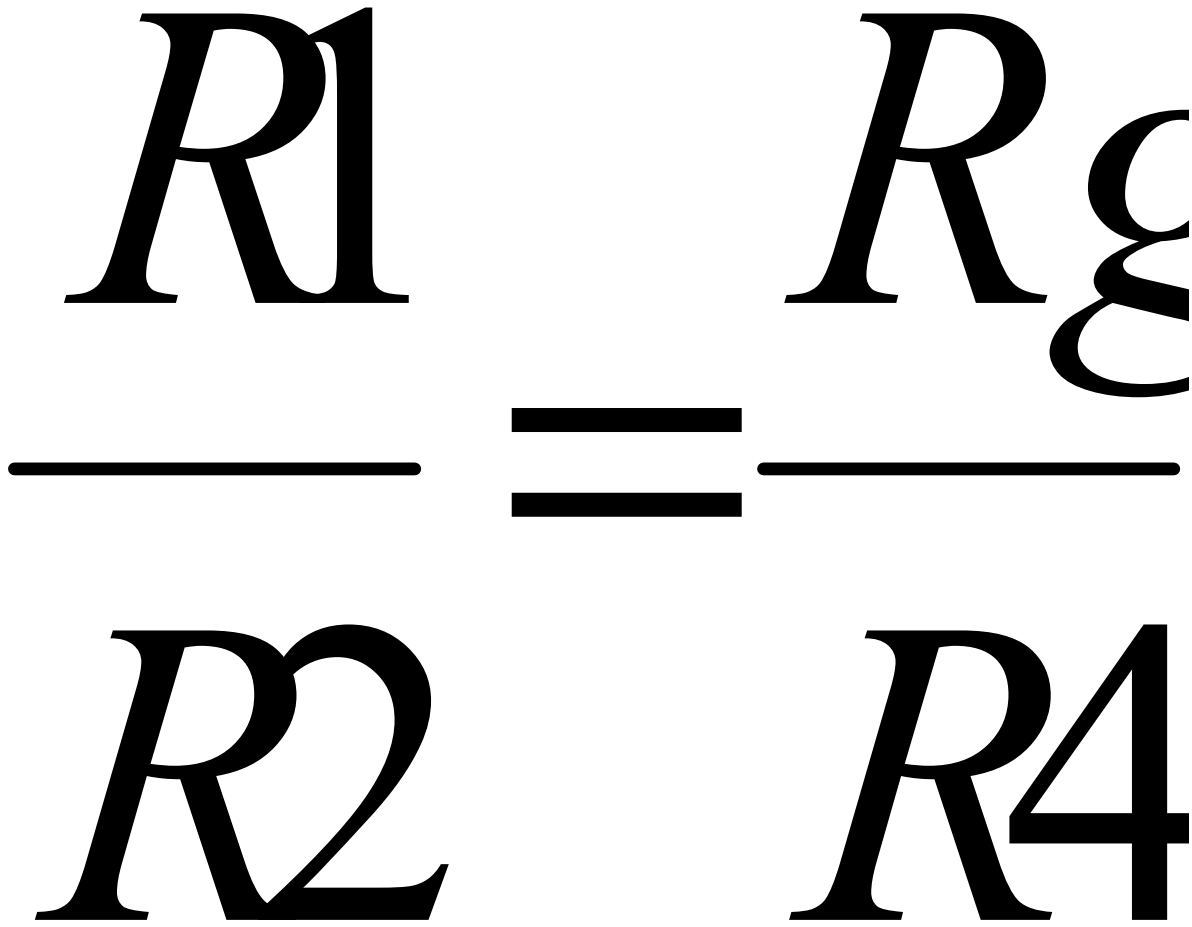

Figure 5.14 True Strain and True Strain Rate Comparison (NSWCDD SHPB 62)

It must first be pointed out that, because the strain gages are mounted at a significant distance from the actual deforming specimen (2.5' in this instance), superimposing the strain gage strain and strain rate over the optically measured strain and strain rate will result in a phase difference between the two measurements methods. This is clearly shown in Figure 5.14. Normalizing a time vector and plotting the equivalent portions of both the strain gage and laser signal, Figure 5.15 results:

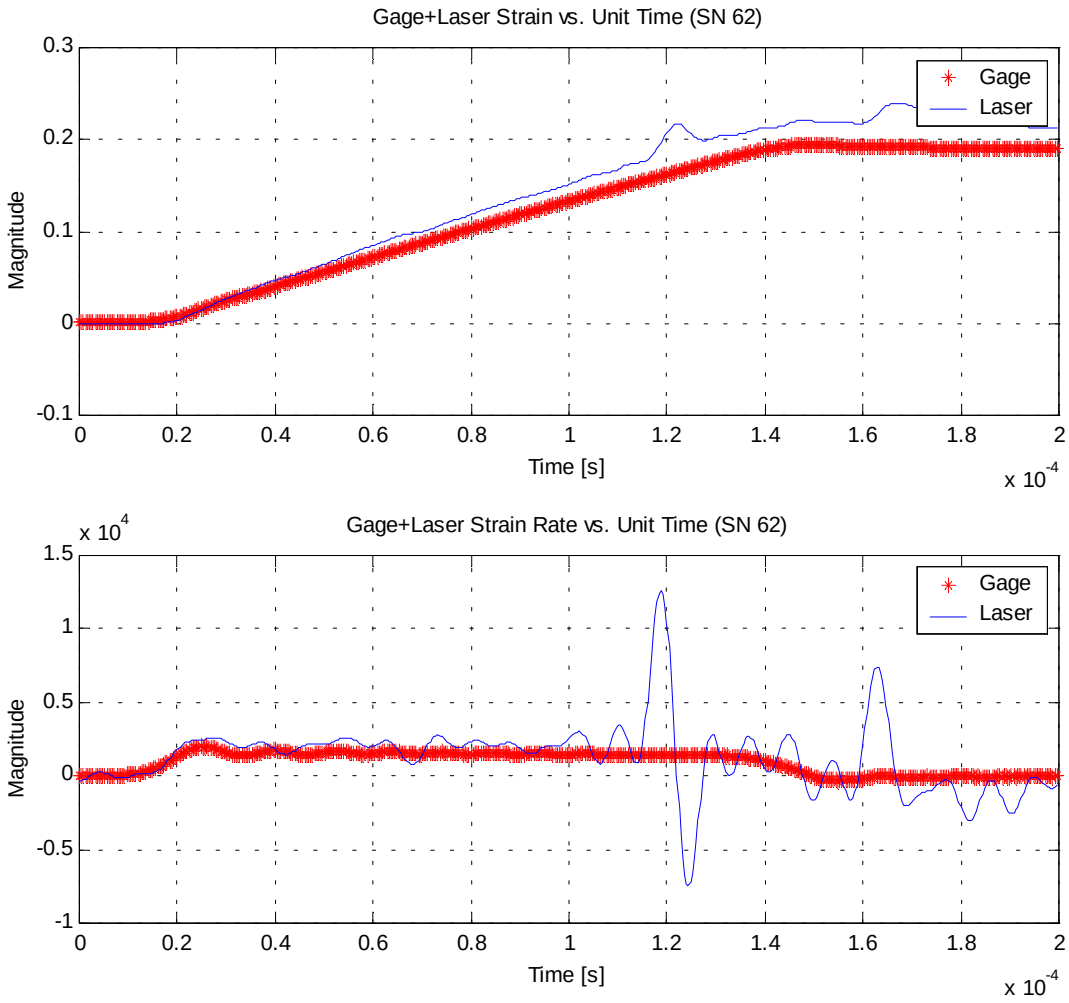

Figure 5.15 Normalized Time True Strain and True Strain Rate Comparison (NSWCDD SHPB SN-62)

Figure 5.15 presents a much more straightforward comparison of the optically measured and strain gage true strain and strain rate. The true strain comparison shows a similar increase in specimen true strain. This can be seen also in the true strain curves, as both curves initially achieve nearly identical levels of true strain rate (~1600 in/in-s). However, the optically measured strain achieves a higher final strain level than does the strain gage signal. This is due to the averaging effect of the analog strain gage. Since the strain gage is reporting a strain level that is lower than peak strain, a lower strain gage true strain level is expected. The oscillations within the optically measured strain rate signal may be attributed to the elastic behavior within the copper specimen. Similar to

the phenomenon of "springback" in the bending (braking) of many metals, the ability to measure the strain directly at the specimen allows the investigator to better identify and understand this elastic behavior.

Finally, the goal of any dynamic testing of materials experiment is the construction of the familiar stress versus strain curve. As detailed previously, no method of stress measurement via the optical strain measurement system employed here has yet been developed. Thus, all stress data presented in this thesis was generated via the output bar strain gage. Utilizing the transmitted bar strain signal shown in Figure 5.7, Equation 5.6 was used to compute specimen true stress:

$$P_2 = A_0 E \frac{\partial u_2}{\partial x} \tag{5.6}$$

Again, E is the elastic modulus of the input pressure bar, d_{Bar} is the diameter of the input bar, d_S is the diameter of the specimen and $\varepsilon_T(t)$ is the transmitted strain history (converted to true strain). With this equation and the dispersion-corrected transmitted pulse shown in Figure 5.7, the following true stress vs. true strain curve was generated for NSWCDD SHPB SN-62 (Dynamic Compression of Copper):

Figure 5.16 True Stress vs. True Strain Comparison (NSWCDD SHPB 62)

It can be seen in Figure 5.16 that the laser curve and the strain gage curve exhibit similar rates of change in the true stress versus true strain relationship. However, the curve generated using the optically measured strain data shows a more pronounced initial increase in true stress at true strain levels near zero. This, again, is due to the averaging of the analog strain gage since averaging can have the effect of smoothing a signal. The ability of the optical strain measurement system to report peak strain levels results in a more abrupt stress increase as the specimen begins to deform. As the strain gage signal falls off due to unloading, the optically generated curve exhibits elasticity in the form of changing specimen strain levels as the specimen unloads. This elastic behavior within

the confines of the plastic deformation regime is an area of future study since this phenomenon has not been available for comprehensive study until recently.

The quicker rise time in the stress-strain figure above has another important significance. Using traditional strain gage instrumentation, the elastic modulus of the material cannot be measured in these highly dynamic experiments due to the errors and uncertainties inherent to the electrical resistance strain gage. However, using the laser to measure actual as opposed to average strain at the specimen, the slope of the stress–strain curve in the elastic regime in Figure 5.16 begins to approach the published elastic modulus of the material. For copper, the published elastic modulus is approximately $18x10^6$ psi. The strain gage generated data from Figure 5.16 yields an elastic regime slope of approximately $6.5x10^6$ psi while the laser-generated data yields an elastic regime slope of approximately $13.9x10^6$ psi. Again, strain gage errors such as strain averaging and windowing tend to underestimate the strain levels achieved by the stress pulse. Thus, all measurements derived from the strain signals will not be truly representative of the actual event. Thus, the real time strain data collected from the optical system significantly improves the ability to estimate the elastic modulus even under highly plastic deformation conditions. Similar results will be demonstrated in the following chapter for aluminum as well.

5.4 NSWCDD SHPB Experimental Results SN-59 and SN-61

Utilizing the optical method of strain measurement in NSWCDD SHPB experiment SN-62, final specimen true strain levels within 2% of the strain gage data were realized. In addition, true strain rates within 6% of industry-accepted strain gage data were achieved. Further proof of these claims can be found in Appendices A and B, the dynamic compression of 6061 aluminum, SN-59 and SN-61, respectively. In these additional experiments, diameter measurements, true strain levels and true strain rates were computed as done for SN-62, the dynamic compression of copper. The results of these experiments are summarized below in Tables 5.5 and 5.6:

Table 5.5 Dynamic Compression of 6061-Al (NSWCDD SHPB 59)

Mechanical Property	Optically Measured	Strain Gage Result	Relative Error
$d_{S,0}$ [in]	0.2035	0.204	0.25 %
$d_{S,F}$ [in]	0.2271	0.228	0.39 %
True Strain [in/in]	0.2232	0.223	0.10 %
Peak Strain [in/in]	0.4193	n/a	---
Strain Rate [s^{-1}]	1592	1550	2.71 %
Peak Strain Rate [s^{-1}]	27000	n/a	---

In Table 5.5, the dynamic compression of 6061-Aluminum (SN-59), the relative error in specimen diameter is a maximum of 0.39%, indicating very good agreement in static measurement applications. Also, very good agreement (0.10%) is shown in the true strain comparison between the strain gage data and the optically measured data. The maximum error between the strain gage results and the optically measured data occurs in the true strain rate. However, this error is only 2.71%.

Table 5.6 Dynamic Compression of 6061-Al (NSWCDD SHPB 61)

Mechanical Property	Optically Measured	Strain Gage Result	Relative Error
$d_{S,0}$ [in]	0.2022	0.202	0.09 %
$d_{S,F}$ [in]	0.2254	0.225	0.18 %
True Strain [in/in]	0.223	0.2231	0.01%
Peak Strain [in/in]	0.461	n/a	---
Strain Rate [s^{-1}]	1697	1592	6.59 %
Peak Strain Rate [s^{-1}]	65000	n/a	---

Results similar to those found in Table 5.5 can be found in Table 5.6, the dynamic compression of 6061-Aluminum (SN-61). The maximum relative error, in this experiment, is 6.59%. This occurs in the strain rate computation due to two important factors: First, the averaging effect of the strain gages on the true strain level is even more pronounced in the strain rate. Secondly, the ability of the optical measurement system to resolve peak strains results in a reported strain and hence, strain rate, closer to the actual levels experienced by the specimen.

Tables 5.5 and 5.6 above were intended to give the reader additional evidence as to the relative accuracy of the data collected utilizing the optical method of strain measurement employed in this research. However, the data and results for experiments SN-59 and SN-61 can be found in Appendices A and B, respectively. These results are presented in the same graphical format as the results shown in this chapter for experiment SN-62.

Chapter 6. Conclusions

6.1 Introduction

The primary assumptions made in performing this research were that the test specimen is in a uniaxial state of stress and that homogeneous deformation is observed. These assumptions can only be ensured via adequate lubrication of the pressure bar-specimen interfaces as well as proper pressure bar-specimen alignment. Realizing these conditions, measuring the strain in either the axial or radial plane is sufficient to characterize the entire strain state of the specimen. In addition, it was surmised that the material, on a "microstructural" scale, is inherently incompressible. These assumptions must be stressed as the results of the experiments detailed in Chapter 5 are discussed. Chapter 6 will present conclusions drawn from the data presented in Chapter 5 and the validity of the above assumptions will be addressed. In addition, recommendations for future research and experimentation will be presented.

6.2 Discussion of Results

In Chapter 5, a complete analysis of the results of NSWCDD SHPB Experiment SN-62, the dynamic compression of copper, was done. In addition, the results from experiments SN-59 and SN-61, the dynamic compression of 6061-Al, were summarized and analyzed. The three experiments generated specimen strains on the order of 0.22 in/in and strain rates of approximately 1592 s^{-1}. Input and output bar strain gages recorded the reflected and transmitted strain histories for conventional computation of specimen strain, strain rate and stress information. Likewise, the optical measurement system was configured to report instantaneous specimen diameter such that corresponding specimen strain and strain rate could be calculated. Relative error values were calculated between the optically measured and calculated data and the strain gage generated and calculated data. The results of these experiments were presented previously in Chapter 5. In this section, these results will be discussed in greater detail.

6.2.1 Plastic versus Elastic Behavior

From the data presented in Chapter 5, it can be seen that specimen initial and final diameter measurements reported by the optical system differed from the caliper-measured initial and final specimen diameters by less than 0.5% in all three experiments. It can also be seen that the optical system, unlike the conventional strain gage instrumentation method, allows the analysis of the time history of the specimen diameter. It is known that elastic behavior is present within the plastic deformation regime. However, the ability to identify and quantify this elastic behavior has been difficult. The optical method of strain measurement employed in this research allows the analysis of this elasticity within the plastic deformation regime. Figures 5.11, A.4 and B.4 show the time history of the specimen diameter for SN-62, SN-59 and SN-61. In all three instances, the elastic behavior is evident in the peak diameter(s) achieved by the specimen. Such elasticity is also evident in the corresponding strain and strain rate time histories. Multiple peaks in these histories show the loading and unloading of the specimen, both plastically and elastically. Although this research cannot quantify the extent of this elastic behavior, this measurement system provides the SHPB investigator a means for further study of this phenomenon.

6.2.2 True Strain Measurement

In providing a better understanding of the changes in specimen diameter during the dynamic event, the optical strain measurement system also allows more complete characterization of the strain occurring within the specimen. It was shown in Chapter 4 how changes in the diameter of the specimen could be related to the true strain within the specimen for incompressible materials subjected to uniaxial stress and homogeneous deformation. With the development of this relation, true specimen strain can be reported in a "real-time" manner. In other words, instantaneous specimen diameter can be readily compared to instantaneous specimen strain with minimal processing. Previously, the SHPB investigator was forced to trim the reflected wave from the incident strain history by estimation of the time required by the stress wave to travel from the specimen to the strain gage. This computation assumes a homogeneous pressure bar material and

requires correction for pressure bar dispersion, both of which introduce additional amounts of uncertainty. The optical method of measurement utilized here is not limited by such assumptions and estimations. Uncertainty considerations as well as the advantages associated with instantaneous peak strain measurements will be examined further in the next sections.

6.2.3 Peak Strain versus Mean Strain

With the ability to resolve peak specimen diameter comes the ability to resolve peak specimen strain. Not previously available to the SHPB scientist, peak strains reported by the optical method of strain measurement give additional insight into the elastic behavior of the specimen within the plastic deformation regime. However, mean strain levels can be computed simply by averaging the strain over the corresponding time interval. Thus, while providing the ability to resolve peak strains, this system also allows easy computation of mean strain levels for comparison with traditional SHPB data. This is an important concept since the vast majority of the SHPB facilities in use still utilize traditional electrical resistance strain gage instrumentation.

In addition, the ability to resolve peak strain has significant effects on the true stress vs. true strain diagram shown in Figures 5.16, A.7 and B.7. Compared to the strain gage generated results, the optical stress vs. strain signal consistently exhibits a more concentrated degree of specimen loading in that the optically generated curves are characterized by quicker specimen stress rise time and greater stress per unit strain loading (plastic modulus). This is evidenced by the abrupt rise in specimen stress during the very early stages of specimen loading (low levels of strain) and the greater slope of the loading curve. Also, “real time” strain data makes obvious the elastic unloading of the specimen as the dynamic event concludes. The ability to measure and quantify these phenomena will have significant effects on the characterization of materials at elevated rates of strain. Material properties affected by such phenomena include strain hardening effects, material toughness and material resilience. However, more experimentation is needed before publication of any such conclusions.

6.2.4 Strain Rate Computation

Peak strain rate and mean strain rate information is available in the same fashion as described in the previous section. It is generally accepted that the peak strain rate available to SHPB scientists is approximately 10^4 s^{-1}. This research has shown that, while the mean strain rate remains well below this level, peak strain rates exceed this level by nearly one order of magnitude. Again, the significance of this ability to resolve peak strain rates will be realized in the study of elasticity within the plastic deformation regime.

6.2.5 Comparison of Sources of Uncertainty

Pressure wave dispersion was previously explained as the attenuation of the stress wave within the pressure bars due to the damping effect of the bar material. Thus, the stress wave arriving at the test specimen is not the same stress wave that was reported by the strain gages. Thus, dispersion correction routines must be initiated to correct for this phenomenon. While SHPB investigators are able to estimate and account for bar dispersion, they are often forced to neglect thermal and electrical errors inherent to the strain gage due to the inability to quantify such effects. The effects, however, can be minimized by proper bridge design and construction as well as proper gage selection. In addition, the strain reported by the strain gage in cyclic strain applications is the average strain over the length of the gage. Thus, peak strain is not available via typical strain gage instrumentation methods. Since the optical system reports specimen diameter in a direct, non-contact manner, errors due to input bar dispersion and input bar strain gage mechanical and electrical errors can be nullified since the strain information previously recorded by the input bar strain gage is now measured via the optical detector.

6.2.6 Signal to Noise Considerations

One of the anticipated benefits of this system was the high signal strength expected from the optical detector. Using the Lasiris 0.9 mW semiconductor laser with the Devar solid-

state photodetector yields and output signal between 700 mV and 1.05 V. With a noise floor of only 30 mV, a minimum signal-to-noise ratio of 27 dB can be expected in the testing of dense materials such as metals and most other dense materials. It is estimated that, even in the testing of more compliant materials such as plastics and composites, a minimum signal-to-noise ratio of 24 dB, corresponding to a final specimen diameter of 0.313 in, can be expected. Also, these levels are attained without the aid of additional amplification or signal processing, other than implementation of a software-based, zero-phase distortion digital filter. Since most types of signal processing and amplification involve some degree of phase distortion, the lack of additional amplification can be beneficial. Zero phase distortion preserves the phase information between the stress wave, specimen diameter history and specimen strain history. Thus, stress wave velocities such as those published by Bancroft as well as experimental strain rates can be computed with much more precision. An example of such a calculation was presented in Chapter 5.

6.3 Low Impedance Materials Application

It has been stressed throughout this thesis that the analysis performed here is valid only for incompressible materials such as metals and dense ferrous alloys. This is due to the assumptions necessary for complete development of the equations relating specimen diameter to specimen true strain. In using this optical method of strain measurement on specimens with relatively low impedances such as foams and composites, additional dynamic analysis similar to that study put forth by Ramesh and Narasimhan [19] should be performed. This is due to the compressibility factor inherent to porous, more compliant materials. Since no such materials were tested in this research, no conclusions can be made as to the ability to calculate specimen strain and strain rate without further analysis. However, the high signal-to-noise ratios achieved with this system coupled with the ability to record the dynamic specimen diameter during the experiment make it ideal for testing such materials. It is surmised that the application of this system to materials with relatively low impedances can be accomplished by performing several experiments and comparing strain gage strains with optically measured strains. Compressibility

factors for various materials could then be published and used to correct for the compressible behavior of such materials. Again, it is believed that such experimentation would only be necessary for highly compliant materials such as foams and other porous materials. For a preliminary discussion of such testing concerns, the reader is referred to Ramesh and Narasimhan [19].

6.4 Recommendations

The advantages of the optical method of strain measurement have been made clear by the data presented in Chapter 5 as well as the commentary presented in Chapter 6. The ability to compute specimen strain and strain rate with data collected in a direct, non-contact fashion provides a powerful tool to the SHPB researcher. One immediate application is the verification of the wave velocity data published by Bancroft. This tabulated data has been the standard for dispersion correction in split Hopkinson pressure bars. Additionally, it may even be possible to achieve a better understanding of the phenomenon of dispersion such that, instead of correcting bar dispersion, it may be possible to prevent bar dispersion. This is important because it is recognized that most SHPB facilities will continue to use existing strain gage instrumentation since the technology is already in place.

The optical system of strain measurement also makes it possible to further investigate one of the primary assumptions governing the SHPB, homogeneous deformation. Using the optical system to carefully measure post-test specimen diameter would allow for the quantification of the degree of homogeneous deformation. In other words, the degree of "barreling" by the specimen could be examined. Should a low degree of homogeneous deformation be observed, additional studies could be done to either correct for or prevent non-homogeneous deformation within the SHPB sample.

As specified in the previous section, additional experimentation should be done to improve the testing technique with regards to low impedance materials. Such materials result in poor signal-to-noise ratios when used in traditional strain gage SHPB facilities.

The relatively high-signal-to-noise ratio achieved here should allow for testing of such materials with this system. However, additional experimentation is needed before tabulation of any such results.

The most logical "next step" is to implement an additional laser to measure axial strain by monitoring the relative distance between the input and output pressure bars. It is theorized that implementation of such a system would provide sufficient information to compute specimen stress without the use of the transmitted strain history. With this "true" stress data, a stress-strain curve could be plotted that depicts the actual modulus of the material throughout both the elastic and plastic deformation regimes. However, further additional mathematical analysis and reduction will be necessary to implement such a procedure

6.5 Concluding Remarks

The research presented here has shown the great versatility and robustness offered by the optical method of strain measurement. The experimentation presented in this thesis covers only a fraction of the possible applications of such a system. One point not touched upon earlier is the relatively low cost of implementing such a system. Lasers in measurement applications are becoming increasingly more prevalent as presented briefly in Chapter 3. Therefore, it is anticipated that more and more SHPB facilities will begin to investigate the idea of implementing such a measurement system. Since the Naval Surface Warfare Center in Dahlgren now has such a system in place, the opportunity exists for NSWCDD to become one of the premier SHPB testing facilities.

Index of Authors

[1] Shigley, J.E. and Mitchell, L.D., *Mechanical Engineering Design,* 4th ed., McGraw-Hill, New York, p. 177 (1993).

[2] Kolsky, H., "An Investigation of the Mechanical Properties of Materials at Very High Rates of Strain," *Proc. Roy. Phys. Soc.,* **B 62**, pp. 676-700 (1949).

[3] Lindholm, U.S. and Yeakly, L.M., "High Strain Rate Testing: Tension and Compression," *Experimental Mechanics*, **Vol. 8**, pp. 1-4 (1968).

[4] Bertholf, L.D. and Karnes, C.H., "Two Dimensional Analysis of the Split Hopkinson Pressure Bar System," *J. Mech. Phys. Solids,* **Vol. 23**, pp. 1-19 (1975).

[5] Bancroft, D., "The Velocity of Longitudinal Waves in Cylindrical Bars," *Physical Review***, Vol. 59**, no. 59, pp. 588-593 (1941).

[6] Graff, K.F., *Wave Motion in Elastic Solids,* Dover, New York, pp. 80-83 (1991).

[7] Davies, R.M., "A Critical Study of the Hopkinson Pressure Bar," *Phil. Trans. R. Society,* **A240**, pp. 375-457 (1948).

[8] Dowling, D.E., *Mechanical Behavior of Materials,* Prentice Hall, New Jersey, pp. 174-175 (1993).

[9] Cloud, G., *Optical Methods of Engineering Analysis,* Cambridge University Press, New York, pp. 13-53 (1995).

[10] Hecht, J., *The Laser Guidebook,* McGraw-Hill, New York, pp. 1-17 (1986).

[11] Hambley, A.R., *"Electronics: A Top Down Approach to Computer-Aided Circuit Design,* Prentice Hall, New Jersey, pp. 470-567 (1994).

[12] Ready, J.F., *Industrial Applications of Lasers,* 2nd ed., Academic Press, New York, pp. 215-231, pp. 278-313 (1997).

[13] Beckwith, T.G., Marangoni, R.D., Lienhard V, J.H., *Mechanical Measurements,* 5th ed., Addison-Wesley, Massachusetts, pp. 272-282 (1993).

[14] Graham, R.A., *Solids Under High-Pressure Shock Compression,* Springer-Verlag, New York, pp.1 –7 (1993).

[15] Coffey, C.S., "Mechanisms of Elastoplastic Response of Metals to Impact," *High-Pressure Shock Compression of Solids III,* Springer, New York, pp. 59-80 (1998).

[16] Szczepinski, W., *Experimental Methods in Mechanics of Solids,* vol. 51, Elevier, New York, pp. 88-124 (1990).

[17] Cheo, P.K., *Handbook of Solid State Lasers,* Marcel Dekker, New York, pp. 1-112 (1989).

[18] Kaiser, M.A., *"Advancements in the Split Hopkinson Bar Test*," Virginia Polytechnic Institute & State University, Blacksburg, Virginia (1998).

[19] Ramesh, K.T. and Narasimhan, S., "Finite Deformations and the Dynamic Measurement of Radial Strains in Compression Kolsky Bar Experiments," *Int. J. Solids Structures,* **Vol. 33**, pp. 3723-3738 (1996).

[20] Ifeachor, E.C. and Jervis, B.W., *Digital Signal Processing: A Practical Approach,* Addison-Wesley, New York, pp.278-373 (1993).

[21] Bell, J.F., "Contemporary Perspectives in Finite Strain Plasticity," *Int. J. Plast.,* **Vol. 1**, pp. 3-27 (1985).

[22] Dharan, C.K. and Hauser, F.E., "Determination of Stress-Strain Characteristics at Very High Strain Rates," *Experimental Mechanics*, **Vol. 10**, pp. 370-376 (1970).

[23] Sharpe, W.N. and Hoge, K.G., "Specimen Strain Measurement in the Split Hopkinson Pressure Bar Experiment," *Exp. Mechanics,* **Vol. 12**, pp. 570-574 (1972).

[24] Laser-Optics USA, "Laser Tutorial," *http://member.aol.com/WSRNet/laser*, (2000).

[25] Measurement Group, Inc., www.measurementsgroup.com, Raleigh, NC, (1996).

[26] "Student Guide to Strain Gage Selection," Measurements Group, Inc., Raleigh, NC (1998).

[27] Love, A.E., *A Treatise on the Mathematical Theory of Elasticity,* Dover Press, New York, NY (1944).

[28] Gorham, D.A. and Wu, X.J., "An Empirical method for Correcting Dispersion in Pressure Bar Measurements of Impact Stresses," *Measurement Science and Technology*, **Vol. 7**, **No. 9**, pp. 1227-1232 (1996).

[29] Krafft, J.M., Sulivan, A.M. and Tipper, F.F, "The Effect of Static and Dynamic Loading and Temperatures on the Yield Stress of Iron and Mild Steel in Compression," *Proc. R. Soc. Lond*., **A-221**, pp. 114-127 (1954).

[30] Hauser, F.E., Simmons, J.A. and Dorn, J.E., "Strain Rate Effects in Plastic Wave Propagation," *Response of Metal to High Velocity Deformation,* Interscience, New York, NY (1961).

[31] Al-Mousawi, M.M, Reid, S.R. and Deans, W.F., "The Use of the Split Hopkinson Pressure Bar Techniques in High Strain Rate Material Testing," *Proc. Instn. Mech. Engrs*., **Vol. 211**, pp. 273-292 (1997).

[32] Bateman, V.I. Brown, F.A., and Hansen, N.R., "A Study of Shock Mitigating Materials in a Split Hopkinson Bar Configuration Phase II," Sandia National Laboratories (1998).

[33] Chen, W., Zhang, B. and Forrestal, M.J., "A Split Hopkinson Bar Technique for Low-Impedance Materials," *Experimental Mechanics,* pp. 1-5 (1998).

[34] Gray III, G.T., "Classic Split Hopkinson Pressure Bar Technique," *American Society of Mechanics*, **Vol. 8** (1999).

[35] Gong, J.C., Malvern, L.E. and Jenkins, D.A., "Dispersion Investigation in the Split Hopkinson Pressure Bar," *American Society of Mechanical Engineers,* **Vol. 112**, pp. 309-314 (1990).

[36] Hariharan, P., *Basics of Interferometry*, Academic Press, San Diego, CA (1992).

[37] National Semiconductor Corporation, www.national.com, DSO11260 (1999).

[38] Burr-Brown Corporation, www.burrbrown.com (1999).

[39] Burstow, C.G., Corell, M.C. and Rogers, A.C., "Mechanisms of Dislocation Motion in 7075-T73 Aluminum Alloy at Strain Rates of 10^5 s^{-1}," *Materials at High Rates of Strain,* Institute of Physics, Bristol, CT (1989).

[40] "Lasers for Structured Lighting," Lasiris, Inc., www.lasiris.com, pp. 1-8 (1999).

Appendix A. Dynamic Compression of 6061-Al (NSWCDD SHPB SN-59)

Figure A.1 3-Channel Output for NSWCDD SHPB Experiment 59

Figure A.2 Dispersion Corrected Reflected and Transmitted Strain Histories (NSWCDD SHPB 59)

Figure A.3 Unfiltered and Filtered Optical Detector Output (NSWCDD SHPB 59)

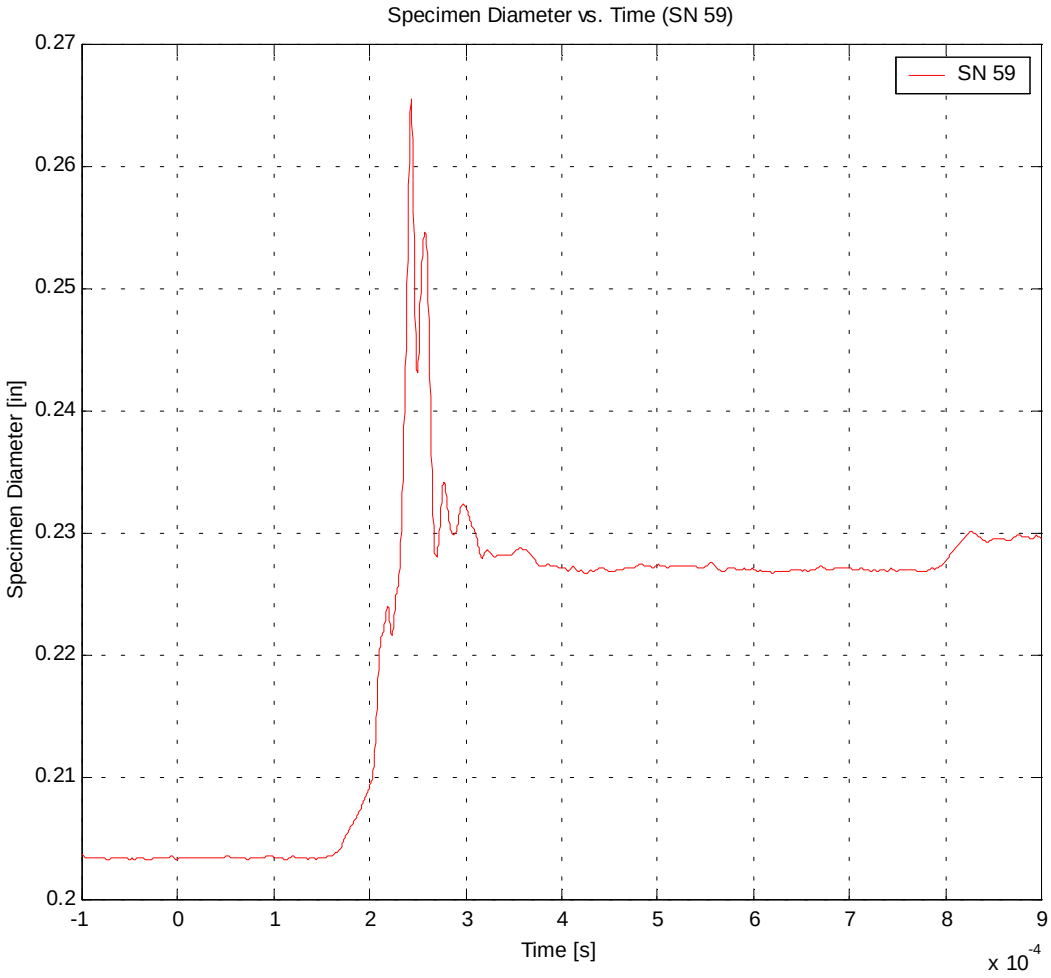

Figure A.4 Optically Measured Specimen Diameter History (NSWCDD SHPB 59)

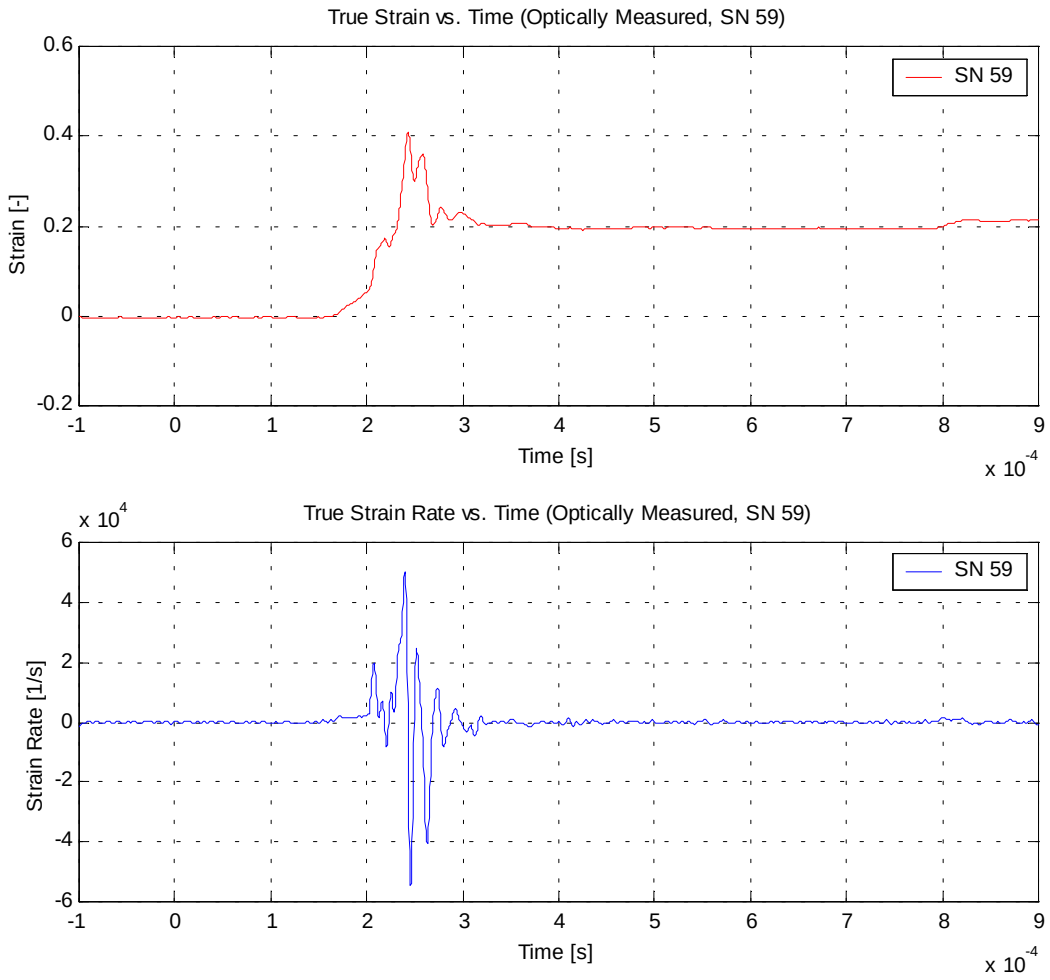

Figure A.5 Optically Measured True Strain and True Strain Rate (NSWCDD SHPB 59)

Figure A.6 Normalized Time True Strain and True Strain Rate Comparison (NSWCDD SHPB 59)

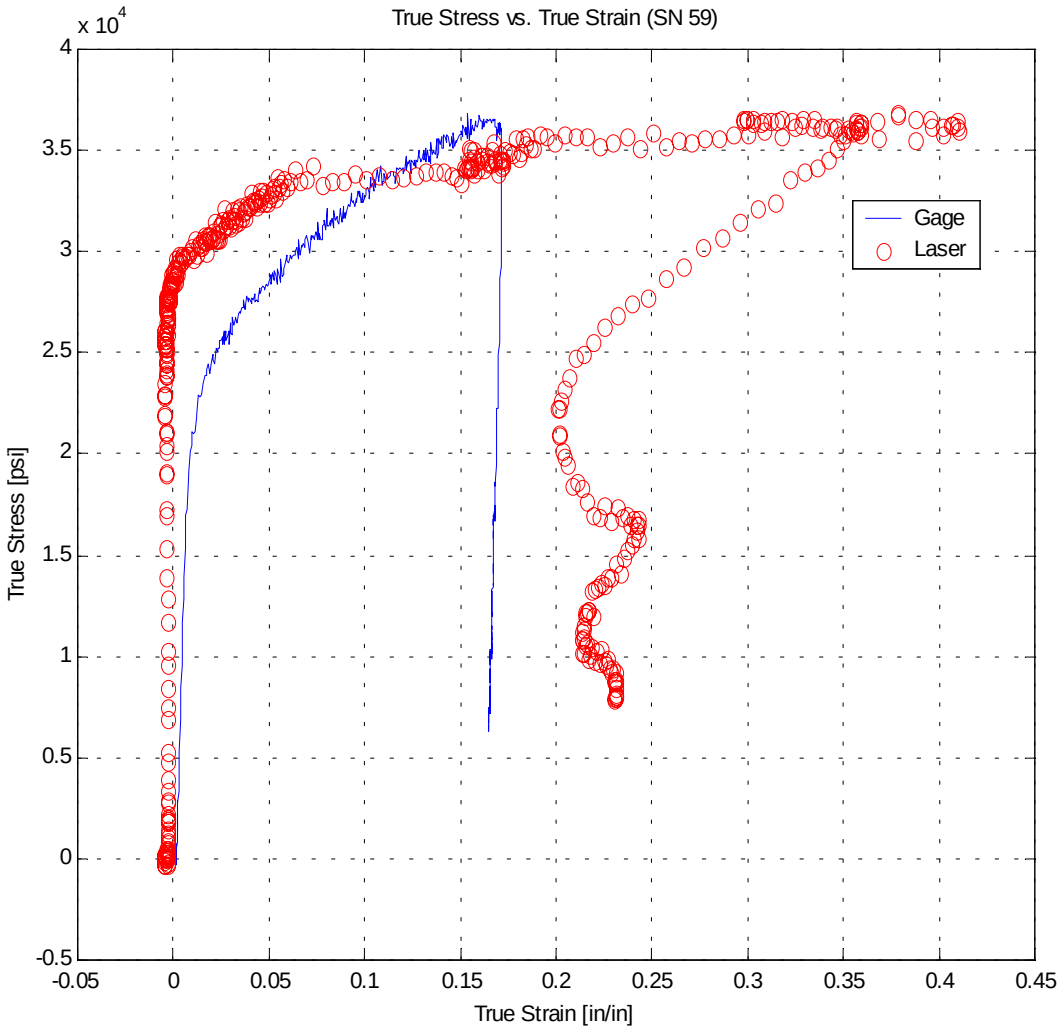

Figure A.7 True Stress vs. True Strain Comparison (NSWCDD SHPB 59)

Appendix B. Dynamic Compression of 6061-Al (NSWCDD SHPB SN-61)

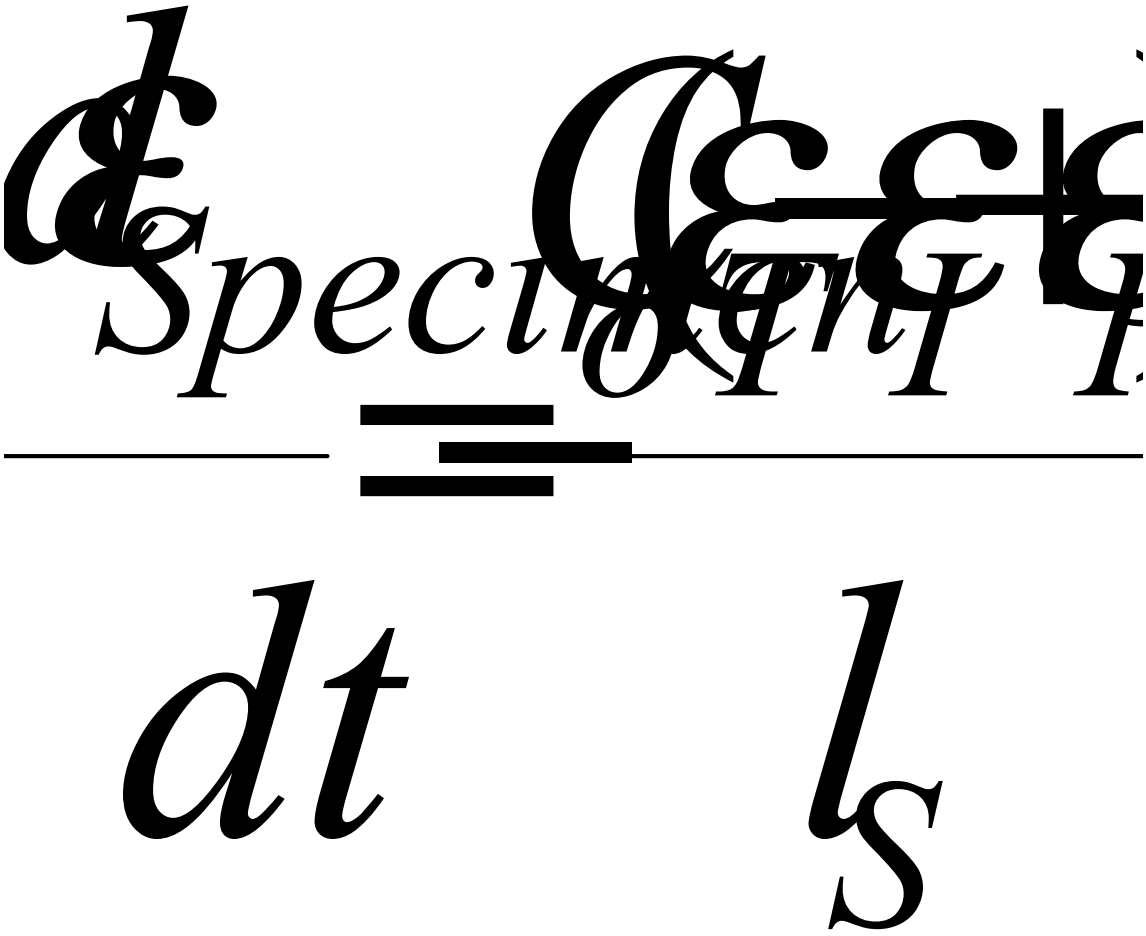

Figure B.1 3-Channel Output for NSWCDD SHPB Experiment SN-61

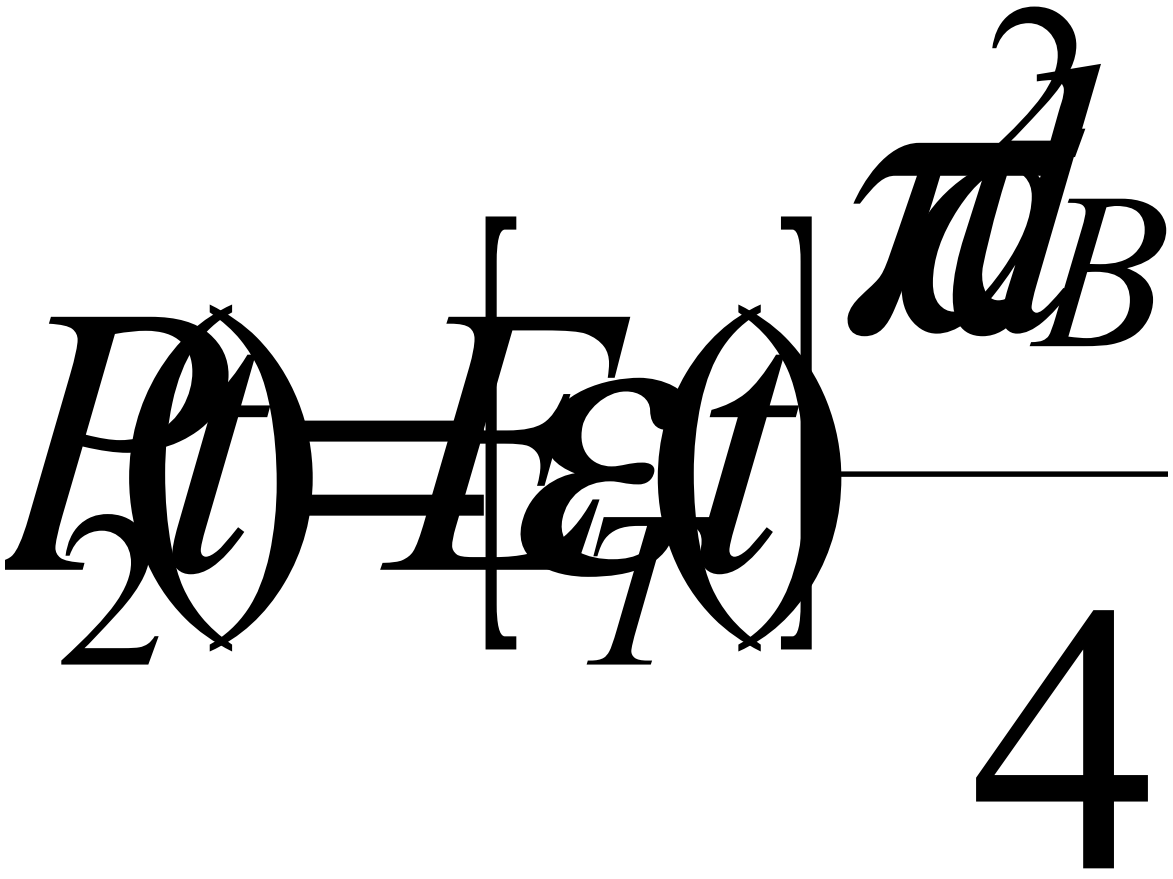

Figure B.2 Dispersion Corrected Reflected and Transmitted Strain Histories (NSWCDD SHPB 61)

Figure B.3 Unfiltered and Filtered Optical Detector Output (NSWCDD SHPB 61)

Figure B.4 Optically Measured Specimen Diameter History (NSWCDD SHPB 61)

Figure B.5 Optically Measured True Strain and True Strain Rate (NSWCDD SHPB 61)

Figure B.6 Normalized Time True Strain and True Strain Rate Comparison (NSWCDD SHPB 61)

Figure B.7 True Stress vs. True Strain Comparison (NSWCDD SHPB 61)

Appendix C. Matlab Code for Optical Strain Measurement Post Processing

```
%%%%%%%%%%%%%%%%%%%%%%%%%%%%%%%%%%%%%%%%%%%%%%%%%%%%%%%%%%%%%%%%%%%%%%%%%%%%%%%
%%%%%%
%              Optical Strain Data Processing Program                          %
%                                                                              %
%  This program loads the data recorded by the optical strain 
measurement   %
%  system and processes it into engineering strain based on the 
calibration %
%  factor [Volts/inch] of the laser.                                           %
%%%%%%%%%%%%%%%%%%%%%%%%%%%%%%%%%%%%%%%%%%%%%%%%%%%%%%%%%%%%%%%%%%%%%%%%%%%%%%%
%%%%%%
%  Clear all buffers:

clear all;
close all;

%  Prompt user for test parameters:

EXP=input('Enter Serial Number of SHPB Experiment >');
L0=input('Enter initial length of test specimen [in] >');
Bard=input('Enter pressure bar diameter [in] >');
Diam=input('Enter initial diameter of specimen [in] >');

%  Specify test parameters:

fs = 2.5e6;
Co = 191000;
gain = 10;
VBS = 10;
VBSR = 10;
GF = 2.05;
Ebar = 29e6;
StressCon = Ebar*(Bard/diam)^2;
StressBridgCon = 2/(gain*GF*VBSR);

%  Retrieve comma separated data files for laser and transmitted 
signals (.csv):

[a,path]=uigetfile('*.csv','Select Incident Data File for Strain 
Calculations',0,0);
cd(path(1:length(path)-1));
pause(.9)
[b, path] = uigetfile('*.csv', 'Select Transmitted Data File for Stress 
Calculations', 0, 0);
pause(.9)
[c, path] = uigetfile('*.csv', 'Select Laser Data File for Strain 
Calculations', 0, 0);

%  Read data files and define time and magnitude vectors:
%  Files are .csv files from Tektronix Digital Oscilloscope.

Incident=csvread(a);
incident_time = Incident(:,1);
incident_mag = Incident(:,2);
I = length(Incident);

Transmitted=csvread(b);
```

```
transmitted_time = Transmitted(:,1);
transmitted_mag = Transmitted(:,2);
T = length(Transmitted);

Laser=csvread(c);
laser_time = Laser(:,1);
laser_mag = Laser(:,2);
L = length(Laser);

%  Mean zero strain gage data:

meani=mean(incident_mag(1:size(incident_time,1)));
meant=mean(transmitted_mag(1:size(transmitted_time,1)));
magi=incident_mag-meani;
magt=transmitted_mag-meant;

%  Compute time interval for derivative calculations:

laser_dt = laser_time(2)-laser_time(1);
transmitted_dt = transmitted_time(2)-transmitted_time(1);
incident_dt = incident_time(2)-incident_time(1);

%  Prompt user to select calibration curve or calibration factor start:
%  If YES, call CALCURVE to prompt for calibration data.
%  If NO, skip CALCURVE and prompt for calibration factor.

ANSWER=input('Do you need to run calibration curve program [y/n]
?','s');

%  YES - Call CALCURVE to accept calibration data and compute
calibration equation:

if ANSWER == 'Y' | ANSWER == 'y'
   [CF1,CF2] = calcurve(ANSWER);
end

%  NO - Prompt user for laser calibration equation:

if ANSWER == 'N' | ANSWER == 'n'
   CF1=input('Enter experimental slope of laser calibration equation
[in/V] >');
   CF2=input('Enter experimental y-intercept value for calibration
equation [in] >');
end


%  FFT of raw laser data to determine frequency content:
%  FFT's transform signal to frequency domain for spectral estimation.

content = fft(Laser(:,2));
mag = abs(content);
freq =
[0:1/(length(Laser)*(1/fs)):(1/(length(Laser)*(1/fs)))*(length(Laser)-
1)]';

%  Plot frequency content of laser signal less dc component:
```

```
figure(1)
subplot(2,1,1),stem(freq(1:length(freq)/2),mag(1:length(freq)/2)/100);
xlabel('Frequency [Hz]'),ylabel('Magnitude [-]')
title(['Frequency Content of Photodetector Signal ',num2str(EXP)]),grid
legend(['SN ',num2str(EXP)])
subplot(2,1,2),stem(freq(1:15),mag(1:15)/100);
xlabel('Frequency [Hz]'),ylabel('Magnitude [-]')
title(['Low Frequency Content of Photodetector Signal
',num2str(EXP)]),grid
legend(['SN ',num2str(EXP)])

%  Design elliptic finite impulse response (FIR) digital filter for
laser signal:
%  This effectively eliminates noise introduced by ambient and
digitizing conditions.

[n,wn]=ellipord(0.1,0.2,0.1,90);
[b,a]=ellip(n,.1,90,wn);

%  Define frequency vector and compute frequency response of elliptic
FIR filter:
%  This is to verify performance of designed elliptic FIR filter.

w=[0:.01:pi];
H=freqz(b,a,w);

%  Plot response of elliptic FIR filter:

figure(2)
subplot(2,1,1),semilogx(w*(180/pi),20*log10(abs(H)))
xlabel('Frequency [Hz]'),ylabel('Magnitude[dB]')
title('Elliptic Filter Frequency Response')
grid
subplot(2,1,2),semilogx(w*(180/pi),phase(H)*180/pi)
xlabel('Frequency [Hz]'),ylabel('Phase [degrees]')
grid

%  Process raw data through FIR elliptic filter:
%  FILTFILT command results in zero phase distortion.

output=filtfilt(b,a,laser_mag);

%  Plot photodetector unfiltered output:

figure(3)
plot(laser_time,laser_mag,'r-')
xlabel('Time [s]'),ylabel('Detector Output [V]')
title(['Photodetector Output vs. Time (SN ',num2str(EXP),')']),grid
legend(['SN ',num2str(EXP)])

%  Plot photodetector unfiltered and filtered output:

figure(4)
plot(laser_time,laser_mag,'r-',laser_time,output,'b-')
xlabel('Time [s]'),ylabel('Detector Output [V]')
title(['Photodetector Output vs. Time (SN ',num2str(EXP),')']),grid
legend(['Unfiltered ',num2str(EXP)],['Filtered ',num2str(EXP)])
```

```
%  Convert photodetector output voltage to inches:

diameter = (output*CF1)+CF2;

%  Compute and plot instantaneous specimen diameter:

figure(5)
plot(laser_time,diameter,'r-')
xlabel('Time [s]'),ylabel('Specimen Diameter [in]')
title(['Specimen Diameter vs. Time (SN ',num2str(EXP),')']),grid
legend(['SN ',num2str(EXP)])

%  Compute specimen radial and axial stretch:

w = (diameter/2)/(diameter(1)/2);
lamda = 1./(w.*w);

%  Begin strain rate and stretch rate computations:

w_rate = (diff(w)/laser_dt)./w(1:length(diff(w)));
lamda_rate = -2*(w_rate./w(1:length(w_rate)));

true_strain =log(lamda);
true_strain_rate = lamda_rate./lamda(1:length(lamda_rate));

%  Plot radial strain and radial strain rate results:

figure(6)
subplot(2,1,1),plot(laser_time(1:length(output)-
1),true_strain(1:length(output)-1),'r-')
xlabel('Time [s]'),ylabel('Strain [-]')
title(['True Strain vs. Time (Optically Measured, SN
',num2str(EXP),')'])
grid,legend(['SN ',num2str(EXP)])

subplot(2,1,2),plot(laser_time(1:length(output)-1),-
true_strain_rate(1:length(output)-1),'b-')
xlabel('Time [s]'),ylabel('Strain Rate [1/s]')
title(['True Strain Rate vs. Time (Optically Measured, SN
',num2str(EXP),')'])
grid,legend(['SN ',num2str(EXP)])


%%%%%%%%%%%%%%%%%%%%%%%%%%%%%%%%%%%%%%%%%%%%%%%%%%%%%%%%%%%%%%%%%%%%%%%%%%%%%%%%
%%%%%%%%%%%%%%%%
%     This section of the code calls dispersion.m to correct for bar
dispersion       %
%%%%%%%%%%%%%%%%%%%%%%%%%%%%%%%%%%%%%%%%%%%%%%%%%%%%%%%%%%%%%%%%%%%%%%%%%%%%%%%%
%%%%%%%%%%%%%%%%
disp(' ');
disp('CALCULATING WAVE VELOCITY VS. FREQUENCY');
Co = 191000;

time = incident_time;
mag=incident_mag;
z=-30;
```

```
[cormagin]=dispersion(mag,time,z,Co);
z=-30;
[cormagref]=dispersion(mag,time,z,Co);clear mag;
mag=transmitted_mag;
[cormagt]=dispersion(mag,time,z,Co);

%  Plot incident, transmitted and laser signals:

figure(7)
subplot(3,1,1),plot(incident_time,incident_mag,'b-',time,cormagin,'r-
'),grid
ylabel('Magnitude [V]')
title(['(A) Incident Signal vs. Time (SN ',num2str(EXP),')'])
legend('Original Pulse','Dispersion Corrected')
subplot(3,1,2),plot(transmitted_time,transmitted_mag,'b-
',time,cormagt,'r-'),grid
ylabel('Magnitude [V]')
title(['(B) Transmitted Signal vs. Time (SN ',num2str(EXP),')'])
legend('Original Pulse','Dispersion Corrected')
subplot(3,1,3),plot(laser_time,laser_mag,'b-'),grid
xlabel('Time [s]'),ylabel('Magnitude [V]')
title(['(C) Laser Signal vs. Time (SN ',num2str(EXP),')'])
legend('Laser Signal')

%  Plot reflected and transmitted strain histories:

figure(8)
subplot(2,1,1),plot(incident_time(1001:1500),incident_mag(1001:1500),'b
-',time(1001:1500),cormagin(1001:1500),'r-')
xlabel('Time [s]'),ylabel('Magnitude'),grid
title(['Reflected Signal vs. Time (SN ',num2str(EXP),')'])
legend('Original Pulse','Dispersion Corrected')
subplot(2,1,2),plot(transmitted_time(1001:1500),transmitted_mag(1001:15
00),'b-',time(1001:1500),cormagt(1001:1500),'r-')
xlabel('Time [s]'),ylabel('Magnitude'),grid
title(['Transmitted Signal vs. Time (SN ',num2str(EXP),')'])
legend('Original Pulse','Dispersion Corrected')


%  Re-initialize test parameters:

fs = 2.5e6;
Co = 191000;
gain = 10;
VBS = 10;
VBSR = 10;
GF = 2.05;
Ebar = 29e6;
StressCon = Ebar*(Bard/diam)^2;
StressBridgCon = 2/(gain*GF*VBSR);

%  Trim data based upon sample size:

magref=cormagin(1001:1500);
magref=magref';
timeref=time(1001:1500);
StrainCon=2*Co/L0;
```

```
StrainBridgCon=2/(gain*GF*VBS);
StrainBridgCon=2/(gain*GF*VBS);

%  Compuite strain via straincalc.m

[Strain]=straincalc(timeref,magref,StrainCon,StrainBridgCon);
Strain=Strain';

%  Compute specimen stress:

Stress=StressCon*StressBridgCon*cormagt(1001:1500);
Stress=Stress';

%  Compute strain rate:

Strainrate=-StrainCon*StrainBridgCon*magref;

%  Plot strain, stress and strain rate results:

figure(9)
subplot(2,1,1),plot(timeref,-Strain,'r*',laser_time,true_strain,'b-')
xlabel('Time [s]'),ylabel('Magnitude'),grid;
title('Strain vs. Time'),legend('Gage','Laser')
subplot(2,1,2),plot(timeref,-
Strainrate,'r*',laser_time(1:length(true_strain_rate)),-
true_strain_rate,'b-')
xlabel('Time [s]'),ylabel('Magnitude'),grid;
title('Strain Rate vs. Time'),legend('Gage','Laser')

%  Plot true stress vs. true strain:

figure(11)
plot(-Strain,-Stress,'b-',1-lamda(531:1000),-Stress(1:470),'ro')
xlabel('True Strain [in/in]'),ylabel('True Stress [psi]'),grid
title(['True Stress vs. True Strain (SN ',num2str(EXP),')'])
legend('Gage','Laser')

%  Overlay strain and strain rate events for comparison (laser and
strain gage results):

figure(12)
subplot(2,1,1),plot(timeref-timeref(1),-Strain,'r*',timeref-
timeref(1),true_strain(610:1109),'b-')
xlabel('Time [s]'),ylabel('Magnitude'),grid;
title(['Gage+Laser Strain vs. Unit Time (SN
',num2str(EXP),')']),legend('Gage','Laser')
subplot(2,1,2),plot(timeref-timeref(1),-Strainrate,'r*',timeref-
timeref(1),-true_strain_rate(610:1109),'b-')
xlabel('Time [s]'),ylabel('Magnitude'),grid;
title(['Gage+Laser Strain Rate vs. Unit Time (SN
',num2str(EXP),')']),legend('Gage','Laser')
```

```
function[CF1,CF2]=CALIBRATION(ANSWER)
home

%  This program compoutes the calibration curve for the SHPB at NSWCDD.
%  User input optical detector output [Volts] for 8 existing
calibration specimens.
%  CALCURVE plots calibration curve and corresponding calibration
factor [V/in].
%  User must verify that curve is linear before using calibration
factor.

%  Prompt user for laser calibration factors:

CAL1=input('Enter detector output for 0.0625" diameter specimen [V]
>');
while CAL1<=0
   disp('Invalid calibration factor (must be >0)')
   CAL1=input('Enter experimental laser calibration factor [V/in] >');
end

CAL2=input('Enter detector output for 0.125" diameter specimen [V] >');
while CAL2<=0
   disp('Invalid calibration factor (must be >0)')
   CAL2=input('Enter experimental laser calibration factor [V/in] >');
end

CAL3=input('Enter detector output for 0.188" diameter specimen [V] >');
while CAL3<=0
   disp('Invalid calibration factor (must be >0)')
   CAL3=input('Enter experimental laser calibration factor [V] >');
end

CAL4=input('Enter detector output for 0.250" diameter specimen [V] >');
while CAL4<=0
   disp('Invalid calibration factor (must be >0)')
   CAL4=input('Enter experimental laser calibration factor [V] >');
end

CAL5=input('Enter detector output for 0.3125" diameter specimen [V]
>');
while CAL5<=0
   disp('Invalid calibration factor (must be >0)')
   CAL5=input('Enter experimental laser calibration factor [V] >');
end

CAL6=input('Enter detector output for 0.375" diameter specimen [V] >');
while CAL6<=0
   disp('Invalid calibration factor (must be >0)')
   CAL6=input('Enter experimental laser calibration factor [V] >');
end

CAL7=input('Enter detector output for 0.4375" diameter specimen [V]
>');
while CAL7<=0
   disp('Invalid calibration factor (must be >0)')
   CAL7=input('Enter experimental laser calibration factor [V] >');
end
```

```
CAL8=input('Enter detector output for 0.500" diameter specimen [V] >');
while CAL8<=0
   disp('Invalid calibration factor (must be >0)')
   CAL8=input('Enter experimental laser calibration factor [V] >');
end

%  Define volt and inch vectors:

volts = [CAL1 CAL2 CAL3 CAL4 CAL5 CAL6 CAL7 CAL8];
inch = [0.0625 0.125 0.1875 0.250 0.3125 0.375 0.4375 0.500];

%  Compute differentials of both vectors to compute calibration factor:

[p,s] = polyfit(volts,inch,1);
fit = polyval(p,volts);
CF1 = p(1);
CF2 = p(2);

%  Plot resulting calibration curve:

figure(10)
plot(volts,inch,'kx',volts,fit,'r-'),grid
xlabel('Voltage [V]'),ylabel('Diameter [in]')
title('NSWCDD Detector Calibration Curve - Diameter vs. Output')
text(0.75,0.47,['Calibration Equation = ',num2str(CF1),'*volts +
',num2str(CF2)])
```

VITA

Steven David Swantek

Steven Swantek was born in Atlanta and grew up near Tampa, Florida. After 12 years of Catholic schooling at Nativity School and Jesuit High School, Steve left home to attend Clemson University in South Carolina. After a brief stint with the Tiger baseball team, Steve returned to the University of Florida to finish his Bachelor's Degree in Mechanical Engineering. Five years later, he kept a promise to himself by returning to earn his M.S. Degree in Mechanical Engineering at Virginia Tech. Upon completion of his Master's Degree, Steve plans to move to Utah to continue his work in engineering as a flight test engineer with Groen Aviation, Inc. He also plans to become a licensed professional engineer, earn a flight instructor's certificate and begin coursework towards an M.B.A.